Fall 10-1-2021

Advancing the Underactuated Grasping Capabilities of Single Actuator Prosthetic Hands

Michael Thomas Leddy
Yale University Graduate School of Arts and Sciences, micleddy@gmail.com

Abstract

Progressing the Underactuated Grasping Capabilities of Single Actuator Prosthetic Hands

Michael Thomas Leddy

2021

The last decade has seen significant advancements in upper limb prosthetics, specifically in the myoelectric control and powered prosthetic hand fields, leading to more active and social lifestyles for the upper limb amputee community. Notwithstanding the improvements in complexity and control of myoelectric prosthetic hands, grasping still remains one of the greatest challenges in robotics. Upper-limb amputees continue to prefer more antiquated body-powered or powered hook terminal devices that are favored for their control simplicity, lightweight and low cost; however, these devices are nominally unsightly and lack in grasp variety. The varying drawbacks of both complex myoelectric and simple body-powered devices have led to low adoption rates for all upper limb prostheses by amputees, which includes 35% pediatric and 23% adult rejection for complex devices and 45% pediatric and 26% adult rejection for body-powered devices [1]. My research focuses on progressing the grasping capabilities of prosthetic hands driven by simple control and a single motor, to combine the dexterous functionality of the more complex hands with the intuitive control of the more simplistic body-powered devices with the goal of helping upper limb amputees return to more active and social lifestyles.

Optimization of a prosthetic hand driven by a single actuator requires the optimization of many facets of the hand. This includes optimization of the finger kinematics, underactuated mechanisms, geometry, materials and performance when completing activities of daily living. In my dissertation, I will present chapters dedicated to improving these subsystems of single actuator prosthetic hands to better replicate human hand function from simple control. First, I will present a framework created to optimize precision grasping – which is nominally unstable in underactuated configurations – from a single actuator. I will then present several novel mechanisms that allow a single actuator to map to higher degree of freedom motion and multiple commonly used grasp types. I will then discuss how fingerpad geometry and materials can better grasp acquisition and frictional properties within the hand while also providing a method of fabricating lightweight custom prostheses. Last, I will analyze the results of several human subject testing studies to evaluate the optimized hands performance on activities of daily living and compared to other commercially available prosthesis.

Dissertation Title: Advancing The Underactuated Grasping Capabilities Of Single Actuator Prosthetic Hands

A Dissertation

Presented to the Faculty of the Graduate School

Of

Yale University

In Candidacy for the Degree of

Doctor of Philosophy

By
Michael T. Leddy

Dissertation Director: Aaron Dollar

December, 2021

ACKNOWLEDGEMENTS

First, I would like to thank my advisor Professor Aaron Dollar for supporting me during my PhD and providing me the opportunities to pursue my research in upper limb prosthetics and present it at robotics conferences around the world. I would also like to thank my committee members, Professor Madhu Venkadesan and Professor Rebecca Kramer for the helpful guidance from initial concepts to my final dissertation.

Next, I would like to thank my fellow lab mates - former and current - that have provided a space of both fun and academic rigor. This includes Joe Belter for teaching me the fundamentals early in my PhD, Dr. Ad Spiers for keeping me in a good mood and expanding my knowledge in robotics, and Neil Bajaj for being the wrist to my hand. Our entire lab has made the last several years incredibly enjoyable for me and I appreciate all the late nights spent helping each other perfect our papers before deadlines.

Last, I would like to thank my parents, Susan Leddy and Michael Leddy, for supporting me in my pursuit of a graduate degree in engineering and comforting me during its challenges. It was their background and constant support that drove my love of academia and I look forward to what is next in this journey.

TABLE OF CONTENTS

I. INTRODUCTION

1.1 Motivation

The finals of the 2015 DARPA Robotics Challenge gathered the most complex and advanced humanoid robots from around the world to compete in everyday life environments. These robots were able to balance dynamically, sense in real time and act autonomously. However, "many robots struggled to grasp objects and use them properly" relying on grippers that "lack the delicate, compliant touch of human digits" [2]. The replication of human hand function – a goal in the field of upper-limb prosthetics - has been a significant challenge when it comes to anthropomorphic robotic system design. According to Childress in his 1995 paper on the history of powered-limb prostheses, "the adequate replacement of the human hand and arm is one of the most difficult problems facing medical technology today" [3]. In this section, I will introduce the current shortcomings of upper-limb terminal devices and discuss recent research in single actuator prosthesis including commercial options available to amputees to motivate the need to further investigate and progress the capabilities of single actuator underactuated prosthetic hands.

1.2 Living with Amputation

In the United States an estimated 541,000 people currently experience different levels of upper limb loss [4] with the leading causes of amputation being vascular disease (54%), trauma (45%) and cancer (less than 2%) [5]. A majority of amputations occur from traumatic incidents either

immediately requiring amputation or developing dyvascular disease which is a reduced blood flow to a limb from a traumatic incident. Although most upper limb amputations are transcarpal (61%) involving fingers, the most common amputation locations are transhumeral (16%) across the bicep and transradial (12%) across the forearm amputations [4]. Prosthetic devices and systems were invented to address and restore function to all levels of upper limb amputation. Upper-limb terminal devices can range in complexity from a passive cosmetic finger for a transcarpal amputee to a high degree of freedom robotic arm and hand for a shoulder disarticulation amputee. A common issue with new amputees is societal withdrawal due to a sudden loss of upper-limb function and a negative self-perception. These prosthetic devices not only serve to restore function but also serve to reestablish feelings of autonomy and a positive self-image to help the amputee continue an active lifestyle and reintegrate back into their communities [6].

Upper-limb terminal devices can be classified into two main categories: passive prostheses, including cosmetic and task-specific devices, and active prostheses, including body-powered and electrically actuated prostheses. Most electrically actuated prostheses are controlled by electromyography (EMG) or muscle activation signals. Newer control techniques such as electroencephalography (EEG) and targeted muscle reinnervation (TMR) are less common but useful for higher degree of freedom systems. However, these newer approaches may be prohibitively expensive for amputees without insurance [7]. Less common actuation schemes such as hydraulically and pneumatically actuated hands are mainly used in research and are limited in amputee usage due to their bulky actuation schemes, weight and appearance.

Within passive prostheses, passive cosmetic hands focus on restoring the aesthetics of the amputated limb and can be either static or passively reconfigurable. Task-specific passive devices are niche devices aimed to improve a specific repetitive activity such as a sport or work related

task. Although passive prostheses do not aim to fully restore human hand function, they are favored for their low cost and aesthetic appearance in social situations. Amputees in the workforce or in athletics may prefer them over active prostheses because they are more robust and can be customized for a certain task [4].

Within active prostheses, body-powered devices are biomechanically actuated through a single driving cable input connected to a shoulder harness. A majority of these devices are hooks with a single moving member; however, simple anthropomorphic devices with passive digits also exist. Body powered devices are favored for their better control feedback, control ease, grasping speed, robustness, reduced weight, reduced noise and low cost [1]. The main drawbacks of these devices are that the user can develop fatigue and that the devices are nominally single grasp, limiting the device functionality. Electrically actuated hands include a range of devices from single actuator powered hooks to anthropomorphic hands with six actuators – one for each finger and one for thumb abduction / adduction. These devices are preferred for daily use, multiple grasp types and functionality, increased comfort with no required harness, better grasping of heavy objects and minimal user fatigue [1]. Some disadvantages of these devices are that they require a battery, are difficult to control, require several weeks of training for more complex devices and are heavy and expensive. Although both body-powered and electrically actuated devices are the most common method of restoring upper limb function, these devices still see very high adult rejection rates at 26% rejection for body-powered devices and 23% rejection for electronic devices. Additionally, amputees pay around 10,000 USD for a body-powered split hook device and over 20,000 USD for an anthropomorphic electrically actuated device [5]. Even including the amputees that are fortunate enough have insurance that covers prosthetic hand cost, the average amputee pays approximately 10,000 USD on average for a device that fits their needs [7]. Low cost functional

alternatives are a focus in both research and commercial fields to provide devices to those who cannot conventionally afford one.

Many research and commercial hands fell short because they were too weak, too heavy, too difficult to control, too fragile or not profitable when it comes to prosthetist billing metrics. Additionally, a robotic prosthetic hand that can replicate the human hand's 20 active degrees of freedom, 17,000 tactile sensors, up to 300°/s finger joint angular velocity [8] and exert above 25N of force at the distal finger with high medial-lateral force production [9], is far from feasible with current portable actuator and sensor technology. The sustained high rejection rates and necessary improvement in device performance signal that there is still much improvement to be made in the field of active prostheses before users are willing to fully adopt the prescribed devices.

Practical limitations in weight, control, fragility and cost have led to many designs that aim to approach the versatility of the human hand through the implementation of underactuated mechanisms [10][11], which can reduce the demanding control of fully actuated devices and passively adapt to objects being grasped. The differential coupling mechanisms in these hands transfer the actuation torque to larger contact areas, providing secure grasps with delicate handling [12]. These underactuated devices rely on differential mechanisms to couple the joints and/or fingers, such as transmissions [13], Geneva mechanisms [14], moveable pulleys, various geared differentials, and whiffletree mechanisms [15]. Regardless of actuator quantity, most commercial terminal devices still employ a single degree of freedom closing motion in each grasp type. Although a single actuator is the minimum required to drive such a motion, a significant number of underactuated hands use two to three dc motors, typically actuating the forefinger and thumb flexion as well as the thumb position [16-18]. One design [19] grasps with a single actuator and uses an additional actuator to provide discrete starting postures. However, more than one actuator

creates a tradeoff between maintaining anthropomorphism and actuator size due to limited packaging within the hand. An underactuated hand with a single larger actuator provides power density and packaging benefits over several smaller actuators. Some single-actuator underactuated hands [20-22] have successfully used a single actuation input to control and balance forces in all five fingers with manually posable thumbs, while others have used mechanical means of fixating or varying finger motion [23][24]. Alongside force balancing and grasp adaptability, these hands do not require haptic feedback to adapt to an object and are anthropomorphic, easy to control, lightweight and low cost. Significant reduction of actuators and mechanical simplicity leads to a significant reduction in device weight, which can help reduce user fatigue. However, highly underactuated single-actuator hands have still not seen widespread usage, lacking in the combination of distinct grasp types and the durability of transmission architecture seen in more complex anthropomorphic hands [25][26].

1.3 Current State of the Art

A prosthetist has two main categories to choose from when fitting an active terminal device - biomechanically actuated body-powered devices and electrically actuated robotic devices with varying control schemes. A vast majority of body-powered designs that have become commercially relevant include single grasp terminal devices that have either a two “finger” precision or a three finger tripod grasp where one active member is connected to the driving harness. The most commonly used device is the split hook (APRL, Hosmer, Fillauer)[27][28] which takes the form of a canted hook allowing passive swing grasping when closed and a voluntary-opening lateral two surface pinch grasp when actuated. A more recent implementation of the split hook, the RIC VO/VC (Research Institute of Chicago) [29], uses a sliding cam mechanism that allows the user to switch between voluntary-opening and voluntary-closing

modes. Another common hook design is the Grip 5 (TRS Prosthetics) [30] which instead of closing laterally is oriented vertically to perform a voluntary closing pinch grasp with a wide range of motion. This device is designed to grab larger objects than a normal split hook because the passive link is designed to more effectively retain and cage objects within the grasp. The most commonly used anthropomorphic body-powered device is the APRL hand (APRL, Fillauer) [31] which has two active fingers that are voluntarily closed against a passive thumb and two passive fingers. The thumb can be moved to two different positions, one for power grasp and one for tripod to effectively changing the grasp span. This hand also has a pull-to-lock mode using a friction lever to sustain grasp force over a long period of time. The APRL hand is the only widely used anthropomorphic body-powered terminal device outside of the maker community; which includes the popular underactuated Cyborg Beast hand [32]. Although technically not a commercial device, the Cyborg Beast is an easy to assemble wrist flexion driven 3D printed hand aimed as a temporary solution for children with minimal access to prosthetic devices.

When fitting electrically actuated commercial prostheses, a prosthetist can choose between a single actuator terminal device or a multi-actuator high degree-of-freedom prosthetic hand. Single actuator devices include powered split hooks, parallel jaw graspers or anthropomorphic tripod graspers with passive ring / pinky fingers. Two common commercial powered split hooks are the Axon Hook (Otto Bock) [33] and the ETD2 Hook (Motion Control, Fillauer) [34] that have a single actuated member and features such as rubber surfaces and grooves to grasp objects with complex geometries. Commercial powered parallel graspers include the Electric Griefer DMC (Ottobock) [35] and PR2 Hand (Willow Garage) [36] which both use a single actuator and coupled linkagevariations to create simultaneous parallel motion at the two fingertips. The Electric Griefer DMC grasping surface is shaped like a split hook while the PR2 hand has two rubber rectangular

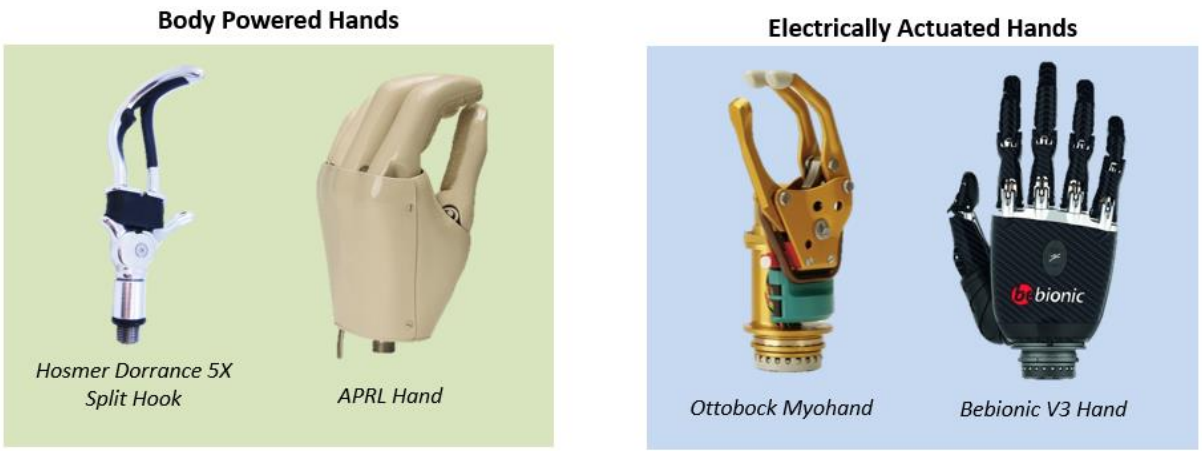

Figure 1. Examples of body powered and electrically actuated hands that are either task specific (Hosmer Dorrance Split Hook, Ottobock Myohand) or anthropomorphic (APRL Hand, Bebionic V3 Hand).

blocks that are used as fingertips. Another successful single actuator hand is the Ottobock Speed Hand (Ottobock) [37] which is preferred for its quick two finger precision grasp and the option to pair it with an anthropomorphic cosmetic glove. Most commercial multi-actuator hands – including the popular Bebionic V3 (RSL Steeper, Ottobock) [38], I-Limb Quantum (Touch Bionics) [39] and Taska Hand (Fillauer) [40] – are anthropomorphic designs which have six total actuators, one for the flexion and extension of each finger and abduction/adduction of the thumb joint. Although these hands have a similar actuation scheme, they vary in finger design, power transmission, control scheme, size and weight. For example, the I-Limb Quantum has gesture recognition and grip chips making it favorable for someone who requires quick switching between multiple grasp types whereas the Taska Hand is larger, waterproof and has compliant joints making it favorable for working conditions. A multi-actuator commercial hand that is used heavily in research conditions is the DEKA hand (Dean Kamen) [41] which when combined with the Luke Arm is the most sophisticated commercial arm platform. This hand takes advantage of six actuators and force sensing to both detect object grasping and to provide feedback to the user. Each of the

above commercial electronically actuated terminal devices is then paired with a control scheme and electrode placement that is determined to be the best for the given patient.

1.4 Research Objective

Although there are several successful terminal devices in a variety of actuation schemes, there is still a need for a hand that can address the tradeoffs in functionality and control simplicity – a middle ground between single and multi-actuator systems [42]. I propose for my research the creation of a prosthetic hand with a single actuation input that can fuse the multi-grasp functionality and anthropomorphic appearance of more complex robotic hands with the control simplicity and low cost of body-powered devices. This device employs a novel combination of underactuation and passive compliance, differential mechanism design and composite manufacturing to create a lightweight, functional and low-cost prosthetic hand with multiple selectable grasp types.

In the next chapters, I will discuss the progression of my doctorate from initial hand prototype to final design and testing. I will first describe the problems that are faced in the field of upper limb prosthetics and how under I will then walk through the initial feedback and steps taken to improve hand performance on activities of daily living. This includes creating new lightweight fabrication methods, optimization of finger kinematics and geometries and improving transmission design. I will then discuss the findings from a finalized benchtop and human subject testing to evaluate the performance of the final design.

II. INITIAL SINGLE ACTUATOR HAND PROTOTYPE

2.1 Initial Design Goals

The focus of my initial prototype was to design a single-actuator anthropomorphic robotic hand that improved upon the previous body-powered hand that I worked on my first two years in the

lab. The goal for this hand to be underactuated with three grasp types that can be driven by a single electrical actuation input. First, given feedback from the body-powered hand, the mechanical design of the hand was improved and the chassis was adjusted to replace the body-powered input with a single actuator and non-backdrivable gearbox. Next, the weak two fingered precision grasping capabilities were improved by first adding additional points of contact, moving from a two fingered precision grasp to a three fingered tripod grasp. Last, I wanted to improve the transmission to allow for the three grasp types to be selected either by the actuator or physical motion of the thumb. In this first phase, I would keep these transitions manual to ensure that the initial mechanism design is sufficient. Once simple kinematic parameters, contact geometry and mechanism design is finalized the device was tested to evaluate the initial changes. The initial prototype was evaluated on activities of daily living and everyday object tasks and compared against other devices currently available on the market to determine the next step forward and what I should focus on improving during the course of my candidacy.

2.2 Initial Single Actuator Robotic Hand Design

The initial prototype of the single actuator hand is a 50th percentile female sized anthropomorphic robotic hand with a single degree of actuation that drives five two-jointed fingers for ten total degrees of freedom. The single actuation input is a brushed DC motor (*5.3 Watt Faulhaber 1524SR*, 6.98 mNm stall torque) attached to pulley-driven Spectra tendons that actively flex all five fingers using PID control. The fingers are passively extended by torsional springs at the metacarpophalangeal joint (MCP) and elastic flexures at the proximal interphalangeal joint (PIP). Finger position is controlled by a position controller that uses information from a high count 2-channel magnetic encoder as well as a current sensor used to detect contact. An additional degree of freedom is provided by a passive switch-locking rotational joint that allows the thumb to abduct

and adduct orthogonal to either the palm or lateral index finger. The palm of the hand is anthropomorphically sized [47] including MCP joint locations which are accurate in relative elevation, lateral positioning and abduction angle. The palm of the prototype hand is a 3D-printed ABS plastic shell with features to mount the internal transmission mechanisms. The front of the palm has urethane gripping surfaces to help secure objects in wrap grasp and the bottom of the palm has a standard ½”-20 threaded post for socket integration. There is a void by the wrist to allow for rotational abduction and adduction of the thumb. This area also houses the spring-loaded button mechanism that allows for repositioning of the thumb MCP joint. This mechanism is located on the bottom of the palm and can be pressed using affordances to aid thumb rotation. This is particularly important for bilateral amputees who may have issues when complex sequences of motions are required to move the thumb position.

The fingers of the single-actuator hand are tendon-driven underactuated anthropomorphically-sized [47] fingers with two joints. Each finger includes an MCP joint passively extended by a torsional spring, an elastic flexure PIP joint, a distal tensioning mechanism, grip pads and a fingernail. A spring plunger pin joint attaches the finger to the base at the MCP joint, allowing the finger to eject under lateral or other unfavorable loading conditions and can easily be reattached. The elastic flexure PIP joint allows for out-of-plane motion and passive reconfiguration of the distal link, promoting the adaptability required for a wrap grasp of a non-uniform object. This flexure has embedded cloth on the neutral axis to mitigate axial stretch, adding kinematic precision and creating a smooth bending motion during finger actuation. Finger flexure geometry, durometer and cloth location were investigated to determine optimal finger motion, input force to closing force, hysteresis and stiffness. A tensioning mechanism in the distal end of the finger consists of a cannulated screw that holds the terminated screw knots, and a hex nut that is integrated

into the distal link. This is used to even the pretension in each finger to ensure uniform closing rates and force transmission. This mechanism is located under a fingernail which helps grasp small thin objects. Due to the rounded nature of the anthropomorphic fingers, the fingertips and distal fingernails have a flat surface to help prevent ejection of smaller objects during tripod and power grasp. There are several friction reduction mechanisms, such as flared tubing in the fingers and v-groove pins in the palm, that help reduce friction from tendon redirection.

The power is transferred from the actuator to the five fingers using a custom transmission and force balancing whiffletree mechanism displayed in Figs. 3 and 5. The transmission connects to the planetary stage of the actuator through a single-start worm gear pair. This non-backdrivable mechanism allows the hand to maintain grasp force for each motor position without requiring onstant exertion from the motor. The worm gear is attached to a pulley transmission that couples the motor force to two driving tendons, one for the thumb and one for the forefingers. The two coaxial pulleys rotate on a keyed shaft and have holes to anchor the driving tendons. The forefinger pulley is located outside of the gearbox in plane with another underactuated coupling mechanism while the thumb pulley is located inside the gearbox in plane with the thumb in lateral position. The pulley radius for each tendon is identical to ensure a similar closing rate and balance the opposing torques of the thumb and forefingers. All the fingers have a similar required excursion to fully close, meaning the pulley radius ratio could be adjusted to provide different closing rates and applied torques to better suit the user. The forefinger driving tendon connects to a coalesced two member whiffletree. This mechanism allows tendon force to be even distributed among the forefingers, allows movement of the forefingers after single finger contact and provides an adaptive human-like grasping response. The connecting link in our whiffletree is coalesced allowing the finger bars to pivot within the driving bar. This reduces the mechanisms size and

required travel, similar to the whiffletree layout in windshield wiper blades, however, it slightly limits the independent finger movement. The two outputs connect the index-middle and ring-pinky pairs where motion is inversely coupled. Our group has investigated using floating pulleys [48] to alleviate forefinger motion constraints. The second tendon from the transmission travels through the palm to the opposite side of the palm to drive the thumb.

The differential tendon routing that splits output from the motor to the eight joints of the forefingers and two joints of the thumb provides a high degree of underactuation that allows the hand to be controlled with single input control. The coalesced whiffletree allows for an adaptive underactuated grasp behavior that allows for increased conformation and contact locations with grasped objects. The routing of the tendon passively over the finger joints and the elastic PIP flexures each aid the underactuated grasp response within each finger, allowing out of plane motion and improved passive reconfiguration around objects. The high degree of underactuation decreases the relative cognitive burden associated with controlling the device when compared to other devices with additional actuators and similar degrees of freedom.

The hand is capable of three distinct grasp types, a power grasp, a tripod grasp and a lateral grasp, that were chosen based on their frequency in everyday activities [46]. The combination of thumb movement and locking the ring-pinky member of the balance bar changes the grasp type of the hand, acting like a transmission that alters the forces, closing rates, timings and fingers used for each grasp type. In power grasp, the thumb opposes the index and middle fingers and each finger closes at an identical rate until contact. The motor torque is equally distributed between the balanced forefingers and the thumb. The whiffletree allows additional finger reconfiguration and changes in grasp force to occur if one finger does not contact the object. In tripod grasp, the ring-pinky member of the whiffletree is locked down creating a new lever arm driving motion. The

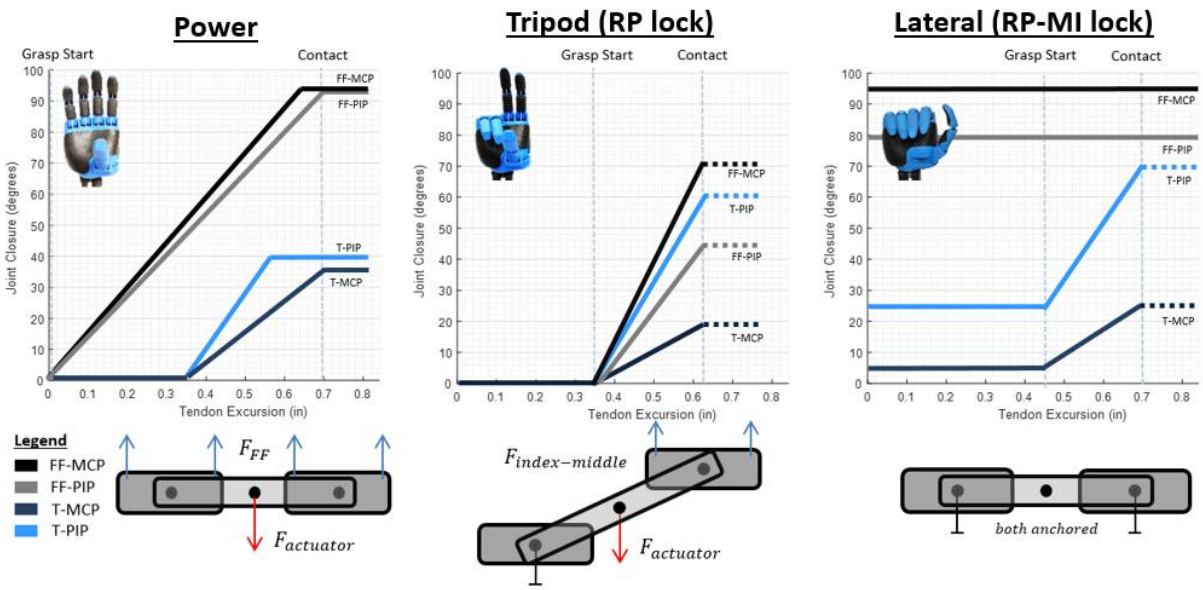

Figure 2. Three distinct grasp types with varying closing rates made possible through different poses in the underactuated whiffletree mechanism. This includes a wide aperture and adaptive power grasp, a fast closing and reduced force tripod grasp and a lateral grasp where the thumb is reposition to oppose the lateral index finger.

starting grasp position is altered to remove all driving tendon slack from the system, introduced from locking down one side of the whiffletree. The index-middle pair then closes on the thumb at twice the closing rate with the same force in power grasp. This is because although the new actuation lever arm is reducing the tendon force only two of the four members are receiving torque from the transmission. This provides a quick tripod grasp, however, reduces the potential grip force and creates a slight force imbalance between the thumb and opposing fingers.

In lateral grasp, a spring-loaded button located on the bottom of the palm is pressed to rotate the thumb to lateral opposition. This button releases a spring plunger located on the bottom of the thumb block that holds the thumb in the power and lateral positions. The spring plunger then slides in a slot until the thumb reaches the next position where it automatically locks into place. The thumb rotation displaces a tendon, which is normally slack, connected to the index-middle whiffletree pair which also slightly closing the thumb. This closes the remaining fingers of the

hand and locks them into place. In lateral grasp, the forefingers are rigidly locked down by the thumb rotation, providing the user with a passive hook grasp that can be used to fixate or carry objects with no motor expenditure or an active lateral grasp that receives all the actuator torque. The grasp types are currently set manually, however, we have investigated methods to mechanically automate these changes [49] so that the full hand functionality and each grasp type can be controlled from a single actuator with a single input. A successful grasp is determined by the motor controller when the actuator has either reached the final position for the given grasp type or a current limit is reached, notifying that an object has been grasped by the hand. The current limit while grasping is determined as a safe value for intermittent usage of the actuator; this value could be increased or decreased depending on the user's preference.

The second iteration of the hand is fabricated using a variety of molding, machining and additive manufacturing techniques. The hand is also highly customizable including custom geometry grip pad molds created in a polyjet 3D printer and potential scalability of the palm and finger chassis to larger sizes. The hand materials include ABS plastic for the palm chassis, finger bodies and thumb block; urethane rubber for the grip pads (*Vytaflex 40*) and flexure joints (*PMC 780*), aluminum for the power transfer components, spring steel MCP torsional springs, and stainless steel for spring plungers, flared guiding tubing, bearings, screws and v-groove pins.

2.3 Motor and Controller Selection

There are several important decisions to be made when determining which type, size and power motor to use in a robotic system. To determine the required motor wattage, a power analysis using finger kinematics estimated the necessary required fingertip force and hand closing rate. The power analysis assumed an approximately 3-in finger link and 90°/s closing rate with 15N of force directed to both the thumb and forefinger driving tendons requiring 5.1 Watts of power. I decided

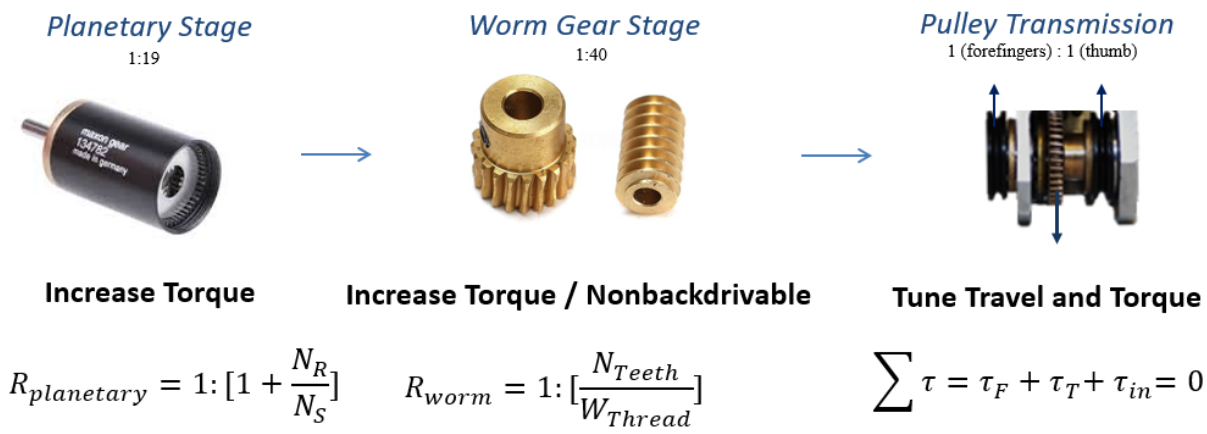

Figure 4. Electrical actuators are nominally high-speed and low torque. The geartrain developed here increases the motor output torque, provides non-backdrivability and helps distribute torque between the thumb and forefingers.

to use a 5.3 Watt brushed DC motor (Faulhaber 1524SR) motor for our single actuator due to its high power density relative to linear actuators, steppers and servos; aw well as its ease of control relative to brushless DC motors. The motor is 15mm in diameter and 43.9mm long; running off of a 6 volt supply the motor has a stall torque of 6.98mNm (2.9mNm continuous), an efficiency of 80%, a rated speed of 3860 rpm and 0.56A continuous operating current. This brushed motor had the highest efficiency and stall torque compared to other leading brands (Maxon, Turnigy, HiTec) at this diameter and length. Due to the high speed / low torque nature of DC motors, the motor is paired with a two-stage 19:1 gear reduction and a nonbackdrivable worm gear reduction of 40:1. The worm gear is integrated into a custom gearbox which drives the stacked pulley mechanism connected to the thumb and forefinger driving tendons. Given these gear ratios we can expect the hand to close at a rate of approximately 72°/s, which is slightly slower than our target. The maximum expected efficiency for the two gear stages (78% for planetary and 80% for worm gear) is 62.4%.

Given the pulley radii and negating friction, we can very roughly estimate that the expected tendon forces are approximately 86N going to the forefingers and thumb producing an extreme distal contact force of 5.86N. There is a two-channel magnetic incremental encoder integrated on the back of the motor which provides 1024 count per revolution feedback for the position and velocity controller. The control board that drives the motor is a Faulhaber MCDC3002RS board which is able to simultaneously measure and control the motor speed, position and current. This board is made specifically for the Faulhaber brushed series motors and allows the motor to be run in speed control, position control or torque control modes. Two breakout boards are used to connect the control board to the motor and to connect the USB programmer to the controller. The simulated myoelectric control signal is currently run directly into a digital input port on the controller and is simulated using a simple high/low switching button. The motor communicates over a simple RS232 protocol that talks to the Faulhaber Motion Manager software: a programmable environment that can control and monitor the motor status. If the integrated system becomes more complex, the MCDC3002RS control board also has the option to communicate via the CANopen protocol if additional system nodes are required. Other alternatives to this control board were investigated using an Arduino platform to potentially reduce the size of the control system; however, this approach would have required additional components, complexity and encoders to control the motor.

2.4 Low-Level Controller Architecture

The low-level motor controller was programmed in Visual Basic using RS232 communication protocol alongside the Faulhaber Motion Manager user interface and motion control toolbox. The current architecture is simple and requires an open and close input from the myoelectric control system which is simulated by a simple button press. The motor starts in a disabled state and is

enabled when the button press occurs. The hand closes until the motor reaches either the end “hand closed” grasping position or the current exceeds the threshold signaling a successful grasp. If either condition is reached, the motor immediately is disabled and the nonbackdrivable worm gear mechanism holds the grasp force. When the button is pressed again to open the hand, the motor enables and drives backwards to the base position of the fully opened hand and the motor is disabled. This same architecture is used for all three grasp types with the exception of the earlier starting thumb and grasp position in tripod grasp. Lastly, the controller was tuned using a PID controller to reduce the overshoot and settling time required to reach a given motor position. The current architecture is limited to the current mechanical specifications of the hand and will be expanded once the thumb switch is automated and mechanisms are introduced to automatically switch between power and tripod grasp.

2.5 Testing Methods

In benchtop testing, two custom sensor embedded objects and a hand grasp force dynamometer (*Camry EH101 Digital Dynamometer*) were used to evaluate the maximum grasp force in each grasp type. Two average measurements were taken in power grasp using a 2.5in diameter sphere with an embedded load cell (*Transducer Techniques MLP-25*) and the 2in span grasp dynamometer. A 1.5 in span cube with an embedded load cell was used to evaluate the fingertip force in precision and lateral grasp. In each test the devices were fixated for distal link contact and the motor was run to stall at the continuous operating voltage within the current thermal limit. It is noted that distal contact produces less contact force than proximal contact in the underactuated fingers. Less contact force is observed at a constant actuation radius for smaller grasp spans that require more finger and passive elastic element motion.

The time to close the hand in each grasp was determined using the time difference measured in the motor controller software (*Faulhaber Motion Manager*) between when the command was signaled and when the encoder reached the final position. The final joint angles for the MCP and PIP joint for the forefingers and thumb were recorded at the end of each grasp using a goniometer and divided by the total closure time to receive the average finger angular velocity for each grasp type. It is noted that the closing rate of each finger varies with angular position and the closing rate of the anthropomorphic forefingers vary slightly due to the slight differences in link length. Starting aperture of each grasp was then measured as the distance between the distal thumb and distal link of the opposing members for each grasp.

The able-bodied testing consisted of five subjects, 4 males and 1 female, who are right hand dominant with no impairments (average age 24.6) and no previous usage of the device (HIC #1608018242). The testing consisted of five minutes of training where subjects could practice grasping sample objects. Next, each subject completed five trials of the Box and Blocks test, where the subject moves as many cubes as possible from one box to another within one minute to evaluate rapid grasping, holding and repetitive motion. Last, each subject completed a full Southampton Hand Assessment Procedure consisting of 26 tasks, 12 abstract object and 14 activities of daily living, recording the time to complete the task. In this test, subjects are encouraged to practice the task sufficiently and attempt to perform it as fast as possible. The Index of Function scores is then generated where an approximate score of 100 represents unimpaired human function, which varies by participant [50] but is nominally accepted. Testing was completed using an able-bodied adapter (*TRS Prosthetics*) to rigidly connect the prosthetic hand to the user. A mechanical button was used to simulate a single myoelectric input to open and close the hand. This was removed to focus on

Figure 5. Initial prototype of the hand with motor controller, mounted to an able-bodied adapter so that able-bodied participants can evaluate the performance of the hand through repetitive motion tasks, abstract object tasks, and activities of daily living (ADLs).

device performance as well as decrease the training time commonly associated with sEMG control. If required, grasps were switched manually in between tasks in the SHAP test.

The preliminary Box and Blocks and SHAP performance of the single actuator hand was compared to the performance of similar myoelectric terminal devices. In [51], eight trans-radial amputee subjects with significant myoelectric experience completed static wrist trials of the Box and Blocks and SHAP test using a single actuator hook (*Motion Control ETD ProPlus*) and a single actuator tripod gripper with an anthropomorphic glove (*Ottobock DMC plus*). In [51], six trans-radial amputees with significant myoelectric experience completed passive wrist trials of the Box and Blocks and SHAP using a two actuator myoelectric (*Ottobock Michelangelo)* anthropomorphic prosthetic hand. In [53], a single wrist disarticulation amputee with significant myoelectric experience evaluated two versions of a five finger anthropomorphic prosthetic hand with five actuators (*Touch Bionics i-Limb, i-Limb Pulse*) using the SHAP test with slight supination and pronation. Both studies included up to a month in training and practice with the

device before completing the functionality assessment. It is noted that grasping techniques employed may differ between subjects with minimal wrist motion [53] and passive wrist motion seen in [51][52] and our study. In evaluation metrics, such as the Box and Blocks and SHAP tests, it is difficult to evaluate device performance without evaluating the user's ability and experience with the device.

2.6 Preliminary Evaluation Results

The average maximum grasp force using sensor embedded objects was 15.21N in power grasp for a 2.75in diameter cylinder, 3.56N in tripod grasp of a 1.5in cube and 18.20N in lateral grasp of a 1.5in cube. In power grasp, the hand was able to grasp the dynamometer with 19.61N at a grasp span of 2in. The increase in dynamometer power grasp force from a smaller span could be due to loss of force from moments in the cylindrical testing setup. When compared to commercial multiple grasp type anthropomorphic hands with multiple actuators the force production is rather low in tripod and power but similar in lateral [54]. This could be due to off-axis force losses when using a single-axis load cell or extreme distal contact in tripod and precision, however, it is difficult to compare because the exact methods of evaluating force production vary by paper. Notwithstanding, the force production in the single actuator hand was still significant enough to grasp and lift each object in the SHAP test. The tripod grasp produced significantly low force partly due to an inefficiency and force reduction that occurs in the whiffletree when one member is anchored. This lever arm produces twice the closing rate but halves the force which should be addressed in future versions. Last, operating at continuous operating voltage and current limits the hands potential grasp force. Due to the inherent intermittent motion of grasping, there are methods to increase grasp force by operating at currents and voltages above continuous operation for short

durations. This is something we could investigate in the future, however, this leads to excessive heating and could potentially harm the electronic components.

The measured grasp aperture for the power and tripod grasp were 113.8 mm due to identical starting positions and the grasp aperture of lateral grasp was 25.4 mm opposing the lateral index finger. The joint range of motions in each grasp type, measured with a digital goniometer, were recorded. The thumb motion was significantly less in power grasp because the thumb is delayed and is obstructed by the closing forefingers. In lateral grasp, the thumb rotation causes a slight excursion creating a smaller motion that starts with the thumb partially closed. In tripod grasp, the fingers contact one another before full joint closure in the forefingers and thumb. The average closing time in was 1.113 seconds in power grasp, 0.476 seconds in tripod grasp and 0.508 seconds in lateral grasp. Tripod grasp was quicker on average than power grasp because the required motion envelope is reduced and a lever arm caused by anchoring half of the whiffletree doubles the closing rate of the forefingers. The lateral grasp was rather slow for its aperture, however, is the strongest of the three grasp types. In [55], the recommended closing rate for a tripod grasp should not exceed 0.8 seconds with a span greater than 90mm to have minimal effect on proprioception. In [56], adequate full closure of the hand in any grasp should be from 1 to 1.5 seconds. Our tripod grasp falls within dictated specifications in [55], however, it may be advantageous to increase the speed of the power grasp which falls outside this recommendation but within those in [55]. When compared to the closing rates of the fully actuated anthropomorphic Bebionic V3 Hand [38], our hand has a slower power grasp (1.1 seconds compared to 0.5 seconds) but a faster tripod and lateral grasp (0.5 seconds compared to 1 second for both grasps). This shows promise for a single actuatorhand on tasks that require precision or small motions. Power grasp speed can be addressed

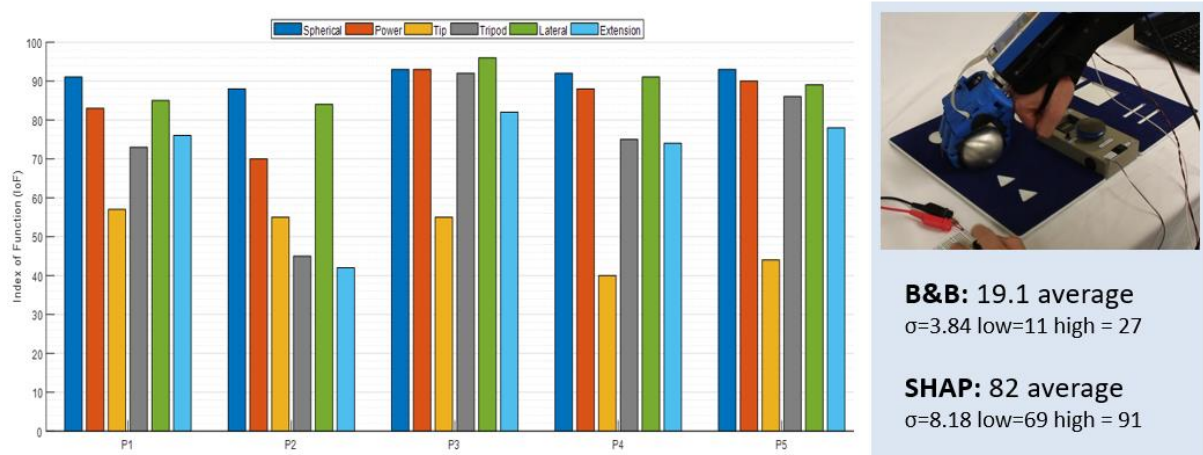

$\mu_{Spherical} = 91.6$ $\mu_{Power} = 84.8$ $\mu_{Tip} = 50.2$ $\mu_{Tripod} = 74.2$ $\mu_{Lateral} = 89.0$ $\mu_{Extension} = 70.4$

Figure 6. Southampton Hand Assessment Protocol (SHAP) results for the initial hand prototype including category scores for spherical, power, tip, tripod, lateral and extension. The overall scores, standard deviation, low and high for each of the two assessment are displayed to the right.

by adjusting the pulley ratios in the gearbox, however, this reduces the maximum tendon force output.

The single actuator hand closing rates are displayed above. Our hand is not close to the 300°/s capability of the human hand, however is rather quick for its force production. In [8], it is rare to see human finger angular velocities exceed 100°/s during grasping, including approximately 50% human grasping with all finger angular velocities under 10°/s. The speed of the hand is promising, approaching joint angular velocities of near or above 100°/s for all three grasp types. There is a discrepancy into why the tripod grasp, only half the joint range of motion with faster finger closure, is not twice as fast as the power grasp which should be assumed by the grasp topology and whiffletree kinematics. This is because as the hand is closed the pulley radius about the MCP joint increases, decreasing the force required to produce a given torque. This mechanical force increase occurs at a quicker rate than the linear spring force increase, causing the fingers to accelerate across the trajectory until contact. The force increase also places the actuator at a more favorable point on its load curve making the stall torque at a given voltage higher. This also explains the rapid

motion of the thumbs PIP joint which starts significantly pre-flexed during lateral grasp. The closing rates and joint angular velocities of the hand can be decreased to align more with [8][56] to align the grasp force with that of the fully actuated commercial prosthetic devices in [54].

The single actuator hand successfully transferred 19.1 blocks (σ = 3.84, low: 11 high: 27) on average over the course of a minute. On average there were 3.7 unsuccessful grasp attempts in each trial; occurrences when the subject closed the hand and was not able to grasp a block. For the SHAP test, the average IoF of the single actuator hand was 82 which is promising for a robotic prosthetic hand with any grasp topology and actuator count. The full index of function distribution by participant is displayed in Fig. 7. Our hand struggled on the tip grasp, scoring a 50.2 on average across participants. This could be due to the weak precision grasp and slightly different closing rates between the index and middle fingers. Additionally, slight variations in tendon tension, either from inaccurate pre-tensioning or stretching, can cause grasp misalignment for all three grasp types. We expected using a button as the input source to marginally aid certain tasks, such as the Box and Blocks and the SHAP abstract object tasks, however, also increase the time to complete bimanual tasks, such as the SHAP button board and jar lid. We believe this advantage would be mitigated when compared to someone with significant myoelectric training. The average Box and Blocks and SHAP index of function (IoF) scores are displayed in Table 3**.**

When compared to a single-actuator robotic split hook in [50] (*Motion Control ETD Proplus)* our hand performed 19.3% better on the Box and Blocks and 41.3% better on the SHAP test. When compared to a single-actuator anthropomorphic robotic tripod grasper [51] (*Ottobock Transcarpal DMC Plus)* our hand performed 19.3% better on the Box and Blocks and 60.8% better on the SHAP test. Although all the devices have a single actuation input, the relative increase in performance on the SHAP test, focused on activities of daily living, could have been bolstered by

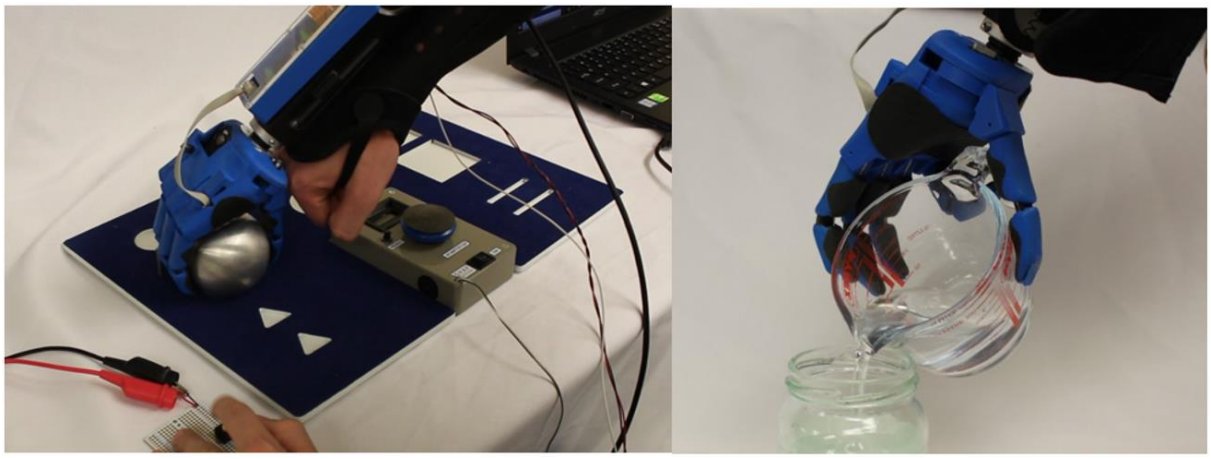

Figure 7. A participant completing two SHAP test tasks. (Left) The heavy sphere task in power grasp and (Right) the bimanual water pouring task. During this assessment the participant attempts to complete the task in as little time as possible without error.

the ability to have more than one grasp type. This would provide less of a benefit on the SHAP test where a simple split hook and tripod grasper could suffice. In both evaluations the wrists were secured in their neutral positions. In [50] amputee subjects with significant training used myoelectric control while in our study a mechanical button was used for able bodied testing. We believe that novice users with a button would provide only a slight advantage, if any, over a trained prosthetic user.

When compared to a two actuator anthropomorphic robotic prosthetic hand [52] our hand performed 31.7% worse on the Box and Blocks and similar on the SHAP test after three months of practice. When compared to a fully actuated five actuator anthropomorphic robotic hand [53] (*Ossur Touch Bionics i-limb)* we performed 57.7% better on the SHAP test after one month of practice and 7.8% better after one year of practice with the i-Limb device. Compared to the newer device (*Ossur Touch Bionics i-Limb Pulse*), our hand performed 7.3% worse after one month of practice and 6.1% worse after four months of practice with the device. Our hand had similar results in the SHAP over the two actuator hand with a static wrist, however, our hand lacked in the Box and Blocks. This could be due to the hand's weak precision grasp compared to the Michelangelo's

two motor precision grasp and the significant training time allowed for the participant. Minimal grasp variety in the Michelangelo hand could have been a negative component to the overall index of function. Compared to the five actuator hands our hand performed favorably against the i-Limb and slightly worse than the i-Limb Pulse. Although there is only one participant in [53], he had the ability to actively flex and extend his wrist which could provide a benefit in the SHAP test for complex motions. All amputee subjects in [52][53] had significant training with myoelectric control which should have provided minimal benefit over the button.

2.7 Initial Prototype Conclusions

The initial results were promising, displaying similar performance to some commercially available devices that have five or more actuators. The initial grasping rates with the current transmission were in line with proprioceptive standards and produced enough force to adequately grasp most objects amputees will run into in daily life. However, significant improvements in certain areas are necessary to improve the hand. First, the misalignment and slight instability of the new tripod grasp caused grasps to fail, especially for smaller objects, heavier objects or while moving objects after grasping. The finger kinematics will have to be improved to produce more secure precision grasps. Next, the rounded gripping surfaces sometimes do not produce enough contact area to sufficiently fasten devices post-grasp. We will further investigate soft contact mechanics and see how we can improve these gripping surfaces. Next, ABS plastic is not a final solution for the hand which saw structural components breaking during testing or excessive external loads to the hand. We will investigate new manufacturing techniques to create rigid and lightweight underactuated prosthesis. Last, the grasp types are currently manual and should be automated with new mechanism design and software control to allow the hand to transition between grasps with minimal effort from the amputees using the device.

III. OPTIMIZING KINEMATICS FOR PRECISION GRASPING

In this chapter, a constrained optimization framework for evaluating the post-contact stability of underactuated precision grasping configurations with a single degree of actuation. Relationships between key anthropomorphic design parameters including link length ratios, transmission ratios, joint stiffness ratios and palm width are developed with applications in upper limb prosthetic design. In addition to grasp stability, we examine post-contact system work, to reduce reconfiguration, and consider the range of objects that can be stably grasped. External wrenches were simulated on a subset of the heuristically evaluated optimal solutions and an optimal configuration was experimentally tested to determine favorable wrench resistible gripper orientations for grasp planning applications.

3.1 Background on Grasping Stability

Underactuated mechanical systems with significantly more degrees of freedom than actuators have been utilized in the field of robotic grasping to provide a grasp that is adaptive and robust without the need for complex control. This approach is extensively applied in the field of upper limb prosthetics [57-60] in which nominally ten to fifteen degrees of freedom are controlled by only a few actuators using coupling mechanisms in the palm and fingers. The compliance in these mechanisms facilitate multiple points of contact during enveloping grasps that can accommodate the arbitrary object positioning, orientation and size seen in unstructured environments [61][62]. However, in a two-fingered precision grasp, which is generally necessary to grasp small objects, unconstrained degrees of freedom and decreased force production from passive elastic elements provide potential reconfiguration and instability. An ideal underactuated hand should combine both wrap grasp performance with precision grasps stability to be effective for a variety of objects.

To ensure that the precision grasp of an object remains stable, the hand-object system must remain stable at contact and as it reconfigures. To determine stability, concepts such as force closure and the equilibrium point may be examined. Finger stability occurs in underactuated two link fingers when the equilibrium point, the location in which the contact, actuation and interlink force lines of action intersect, is within the friction cone [63]. An object is considered to be stable in precision grasp when it satisfies force closure, indicating the forces applied between antipodal contact points on an object are positive or zero, the contact line lies within each friction cone and net wrench on the object is zero [64].

Recent research has taken many different approaches to address the stability issue seen in underactuated precision grasping. In [65], the equilibrium point was investigated to develop mechanical joint limits and determine optimal contact locations for a single actuator grasper with a force differential. On-contact stability was further investigated in a finger that could manipulate its static equilibrium point by mechanically changing its transmission ratio [66]. A constrained optimization was implemented to determine finger parameters for successful form closure of a single actuator multi-link robotic gripper [67] and to determine the passive wrench resistibility of a two-fingered hand fixed in force control [68]. Stable reconfiguration has been investigated for controlled manipulation of two separately actuated, underactuated fingers [69] and for the motion compensation of a similar underactuated gripper [70]. Although stability has been investigated in two finger precision grasping, minimal research addresses the optimality of these configurations for grasping where sophisticated control of the end effector is not possible due to limited number of actuators nominally controlled open loop.

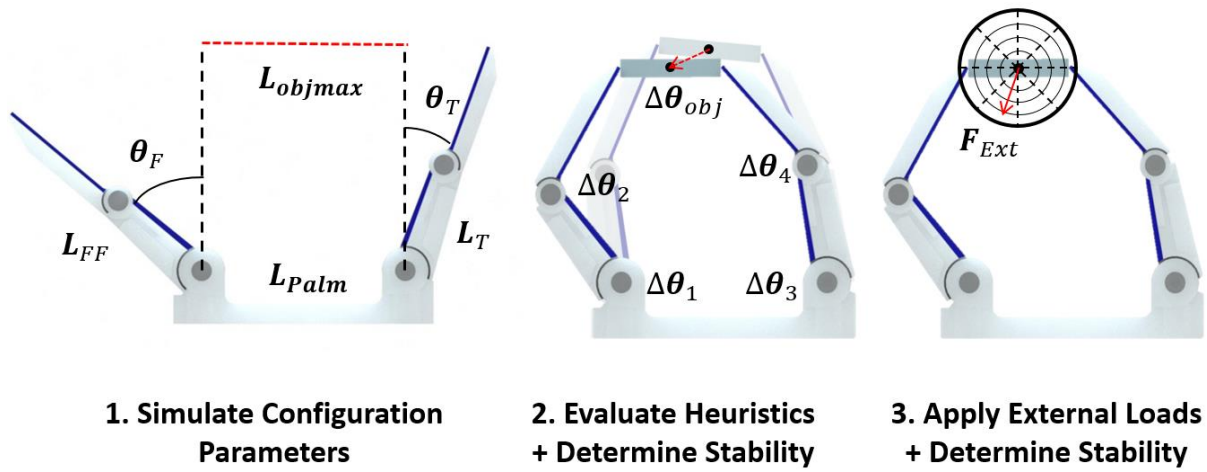

Figure 8. An overview of the three step process for creating and evaluating precision grasping configurations. This included first simulated initial parameters and bounding constraints create the systems kinematics. Once a configuration was established it was evaluated on several heuristics necessary for a stable grasp. Last, favorably performing configurations were exposed to external loads evaluating the stability of the hand-object configuration.

3.2 Constrained Optimization Framework

When defining stability of the hand-object system in precision grasp, we determined that both the finger and object should be in quasistatic equilibrium at contact and while reconfiguring. The underactuated hand was modeled as two symmetric two-link fingers grasping orthogonal rectangular objects in point contact with coulomb friction, where contact force vector $\vec{\boldsymbol{F}}_c$ can be applied at any direction with the friction cone angle $\alpha = arctan(\mu)$. Force closure determined object stability in this model, requiring the forces applied between antipodal contact points on an object to be positive or zero, the contact line to lie within each friction cone and the net wrench on the object is zero. However, the antipodal grasp theorem tells us that the object will remain stable with our contact model. As an additional heuristic, the equilibrium point P_{EQ} location relative to the friction cone, was introduced to evaluate the quality of grasp stability for a given grasp. When the equilibrium point is within the friction cone there exists a wrench that the finger can exert without slipping or reconfiguring to stabilize the object [63]. We described this equilibrium point

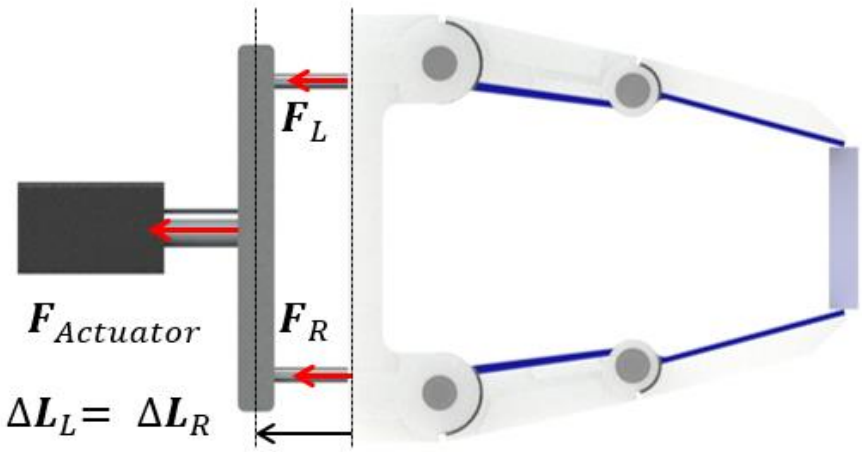

Figure 9. Initial model of precision grasping an object with two two-jointed fingers driven by a single actuator.

configuration as a reliable precision grasp and implemented grasp reliability as an additional criteria for evaluating finger stability under arbitrary external disturbances.

Failure to stabilize the object was determined when force closure of the object was broken or finger equilibrium was not ensured with the grasp reliability heuristic. This was simplified into four main stability criteria for each finger, the tendon force magnitude $\boldsymbol{F}_T$ being positive or zero, the contact force magnitude $\|\boldsymbol{F}_c\|$ being positive or zero, the contact force vector $\vec{\boldsymbol{F}}_c$ between antipodal points is located in the friction cone manifold given object tilt θ_{ob} and the finger contact force vector and contact moment arm $\vec{\boldsymbol{F}}_c, \vec{\boldsymbol{r}}_c$, interlink force vector and moment arm $\vec{\boldsymbol{F}}_l, \vec{\boldsymbol{r}}_l$ and tendon force vector and moment $\vec{\boldsymbol{F}}_T, \vec{\boldsymbol{r}}_T$ are in force and torque equilibrium. It is noted that under external wrenches the contact force vector and antipodal line are not collinear, when the contact force vector points outside of the friction cones the object experiences slip. When these criteria, listed below, are satisfied the hand-object system reconfigures like a constrained six bar mechanism.

$$\boldsymbol{F}_T \geq 0 \quad , \quad \|\boldsymbol{F}_C\| \geq 0 \tag{1}$$

$$\mu - \tan(\theta_{ob}) \leq \frac{|\boldsymbol{F}_{cy}|}{|\boldsymbol{F}_{cx}|} \leq \mu + \tan(\theta_{ob}) \tag{2}$$

$$\sum \vec{\boldsymbol{r}}_i x \, \vec{\boldsymbol{F}}_i = 0 \tag{3}$$

Constraints were placed on feasible parameters to reduce the sample space of the optimization. Configurations were normalized and sampling ranges were limited to reflect that of anthropomorphic configurations that were kinematically feasible. Anthropomorphism was preferred for the underactuated hand parameters because these configurations nominally produce favorable wrap grasp performance [63] and we aimed to retain these benefits as we further optimized the precision grasping performance. The initial sampled parameters were simplified to three normalized independent variables, the distal radius r_d, the distal link length L_d, and the palm width L_{palm}. The proximal finger length L_p was determined by keeping the total finger length constant such that $L_p = 1 - L_d$. The value for the proximal radius r_p was kept consistent to determine the transmission ratio and the proximal joint stiffness $K_p$was kept consistent to determine the distal stiffness K_d given a predetermined anthropomorphic free swing trajectory constant $\boldsymbol{c}_{fs}$ that maps the relative movement of the finger proximal joint θ_p and distal joint θ_d in free swing.

$$\boldsymbol{c}_{fs} = \frac{r_d}{r_p}\frac{K_p}{K_d} \tag{4}$$

The post-contact reconfiguration of the system from increased actuator force or external disturbances was modeled as a constrained six bar mechanism. The system kinematics were evenly constrained to regularize the optimization producing a unique solution for each of the eleven variables that kinematically determined our model. Variables included θ_1, θ_2 and θ_3, θ_4 the proximal and distal joint angle for the left and right fingers, the object tilt θ_{ob}, the left and right tendon forces F_{TL}, F_{TR} and the X and Y components of the contact force for the left and right finger F_{XL}, F_{YL} and F_{XR}, F_{YR}. First, the tendon tension must balance the actuator force F_{act} so that the

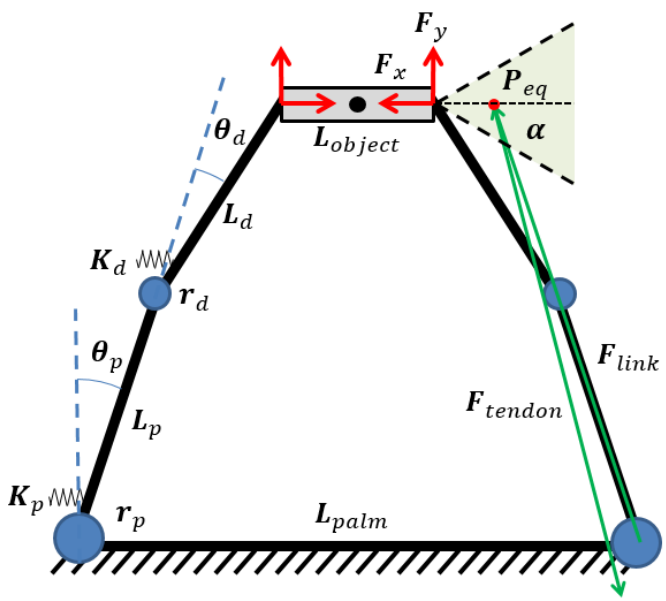

Figure 10. General kinematic model of a precision gripper in static equilibrium. This includes the palm, object and link lengths, relevant spring stiffnesses and transmission ratios, joint angles and tendon forces.

fingers remain in equilibrium with the actuator. Coupled tendons also inferred that the tendon length change in the fingers ΔL_{TL}, ΔL_{TR} must be equal. The next two constraints, evaluated at an initial configuration θ_0, required that the six bar linkage closure constraints were unviolated to ensure object contact was maintained throughout the grasp.

$$F_{act} = F_{TL} + F_{TR} \tag{5}$$

$$r_p\theta_1 + r_d\theta_2 = r_p\theta_3 + r_d\theta_4 \tag{6}$$

$$\begin{bmatrix} L_p c_1 + L_d c_{12} \\ L_p s_1 + L_d s_{12} \end{bmatrix} + \begin{bmatrix} L_{ob} c_{ob} \\ L_{ob} s_{ob} \end{bmatrix} = \begin{bmatrix} L_p c_3 + L_d c_{34} + L_{palm} \\ L_p s_3 + L_d s_{34} \end{bmatrix} \tag{7}$$

Where s_{12} and c_{34} are shorthand for $\sin(\theta_1 + \theta_2)$ and $\cos(\theta_3 + \theta_4)$ and angles are evaluated in the direction of closure. The finger torque balance provides four equations and ensures both fingers are in static equilibrium while grasping the object. In this formulation, the actuator torque must equal the elastic element restoring torque plus the contact torque. The product between the actuator jacobian, describing the actuation lever arms $\boldsymbol{J}_{act}^T = [r_p \ r_d \ r_p \ r_d]$, and the tendon force F_{act}

consisting of F_{TL} and F_{TR} produces the actuator torque. The product of diagonalized spring stiffness $\boldsymbol{K}_{1-4}$ and the net closure $\Delta\boldsymbol{\theta}_{1-4}$ produces the spring restoring torque. Last, the product of the contact jacobian, mapping the moment arms of the joints to the contact point, $\boldsymbol{J}_c^T(\theta_i, \theta_{ob})$, and the contact forces $\boldsymbol{F}_{cL-R}$= $[F_{XL}\ F_{YL}\ F_{XR}\ F_{YR}]$ produces the contact torque. The last three constraint equations are generated from the object static equilibrium conditions that must balance an applied external wrench. In this constraint which $\vec{F}_c$ is the concatenated contact force vector for each finger, G is the grasp matrix that maps the contact forces to the object frame and $\vec{\boldsymbol{F}}_{\boldsymbol{ext}}$ is the external wrench. The contact jacobian $\boldsymbol{J}_c^T(\theta_i, \theta_{ob})$ and grasp matrix $\boldsymbol{G}$ form are explained in further detail in [69].

$$\boldsymbol{J}_{act}^T\boldsymbol{F}_{act} = \boldsymbol{K}_i\Delta\boldsymbol{\theta}_i + \boldsymbol{J}_c^T(\theta_i, \theta_{ob})\boldsymbol{F}_c \tag{8}$$

$$\boldsymbol{G}\vec{\boldsymbol{F}}_c + \vec{\boldsymbol{F}}_{ext} = 0 \tag{9}$$

Constraints and failure criteria were considered in every step of the constrained optimization. Configurations that violated the constraints or failure criteria were eliminated during each step of the parameter search. The initial set of stable solutions were configurations that remained stable at contact and during reconfiguration up to a determined maximum tendon force F_{Tmax} for objects from 0% to 50% of the finger length. These percentages were chosen to represent precision grasping of a variety of small to large objects. The configurations that passed this initial stability heuristic were passed through two additional criteria to evaluate their performance for practical robotic grasping focused on reliably grasping a large variety of object sizes and reducing post-contact work. Two additional criteria were established to evaluate stable configurations for favorable performance in grasping tasks. Due to instability in two-fingered underactuated precision grasping from slipping or ejection [71], one is usually limited to grasping a small variety of objects. This is partly attributed to reconfiguration that can occur in underactuated hands post-

contact requiring compensatory movement to adequately place an object [70]. Thus, favorable designs of underactuated hands include the ability to stably grasp a variety of object sizes with minimal system reconfiguration.

The first objective was to find configurations that produce grasp reliability across the largest span of object sizes. This was calculated using the previous constrained optimization and varying L_{ob} > 50% finger length until failure. The second objective was to minimize post-contact work of the hand-object system to reduce post-contact joint motion and object reconfiguration. Post-contact work $\Delta \boldsymbol{W}_{pc}$ was calculated as the integral of product of the post-contact change in actuator force, $\boldsymbol{F}_{Tpc} = F_{Tmax} - F_{Ti}$, and the difference in tendon length $\Delta \boldsymbol{L}_{Tpc} = L_{Tf} - L_{Ti}$. Where F_{Tmax} is the maximum actuator force, F_{Ti} is the tendon force at contact, L_{Tf} is the tendon length after reconfiguration and L_{Ti} is the tendon length at contact. Minimizing this metric reduces the amount of compensation a robotic system may have to do to account for this motion.

$$\Delta \boldsymbol{W}_{pc} = \int F_{Tpc}\, \Delta L_{Tpc} \tag{10}$$

To evaluate configuration performance, an optimization function was incorporated to produce a weighted value of the given configuration combining the stable grasp width and post-contact work. The weighted value C_{score} is a maximization of the three elements, the post-contact work for a very small object $\boldsymbol{S}_1 = 1/\Delta \boldsymbol{W}_{pc0\%}$, the post-contact work for a large object $\boldsymbol{S}_2 = 1/\Delta \boldsymbol{W}_{pc50\%}$, and the maximum reliable grasp span $\boldsymbol{S}_3 = L_{mso}/L_{finger}$. The constant $\boldsymbol{A}_i$ determines the weight of each element in the optimization function. Each individual value is normalized against the maximum and minimum range of values in the stable configuration solution space to eliminate bias in the case elements have different variability.

$$C_{score} = \sum \boldsymbol{A}_i \frac{\boldsymbol{S}_i - \min(\boldsymbol{S}_i)}{\max(\boldsymbol{S}_i) - \min(\boldsymbol{S}_i)} \tag{11}$$

Once weighted values were determined, an external wrench was applied to the already grasped object for the top 40% of maximally performing configurations to determine configuration stability. The external disturbance was applied in the global frame and acted in the center of the grasped object to determine the maximum resistible wrench, a measure of configuration post-contact stability [72]. This metric also further evaluates the stability of fringe cases where maximally performing solutions fall close to the stability solution hull. External disturbances can create force asymmetry which removes the mirrored motion of the proximal and distal joints (θ_p, θ_d), allowing nonzero object tilt (θ_{ob}) and differences in tendon force (F_{TL}, F_{TR}). For simplicity the system can be modeled as an asymmetric constrained six bar linkage, subject to elastic elements and joint limits, to solve for displacement of hand-object system. To experimentally test and validate the simulation a two-fingered precision grasper was developed using parameters from a sample optimal solution. A single linear actuator drove two symmetric fingers in open loop force control. The object was acquired and the actuator tendon was tensioned to a designated force allowing the system to reconfigure. To simulate an external disturbance in the global frame, the apparatus was placed in a variety of orientations and weights were slowly added to the center of the object until object slip occurred. The maximum resistible wrench and external disturbance profile was calculated and compared to the simulation results.

3.3 Symmetric Optimization Results

A parameter search of three independent variables (r_d, L_d, L_{palm}), bounded by initial sampling constraints on anthropomorphism and kinematic feasibility, was conducted to determine stable configurations using gradient descent of a constrained nonlinear multivariable function in MatLab

Table 1. Final Symmetric Kinematic Parameters

Parameter	Stable Contact and Reconfiguration (0%-50% L_{finger})				
	Minimum	***Mean***	***Maximum***	***Sampled Range***	***Test Config***
Link Length Ratio (L_d/L_p)	0.680	1.085	1.460	[0.68 – 1.46]	1.403 (43.2mm/30.8mm)
Transmission Ratio (R_d/R_p)	0.383	0.503	0.583	[0.01 – 1]	0.583 (6mm/3.5mm)
Stiffness Ratio (K_d/K_p)	0.548	0.719	0.833	[0.01 – ∞]	0.833 ($0.037\frac{N}{m}/0.044\frac{N}{m}$)
Palm Width (L_{palm}/L_{finger})	0.500	0.945	1.500	[0.5– 1.5]	0.770 (57mm)

[73]. The free swing trajectory constant c_{fs} was set to 0.7 to resemble an anthropomorphic hand [74] with a large grasp envelope. Given our initial model, 0.1% of tested configurations (n = 3.2 million) remained stable for an object size of 0% to 50% finger length in the bounded parameter search. The simulated friction coefficient was conservative at μ = 0.7. The link length ratio was sampled from 0.68 to 1.46 which represented a 10% L_{finger} variation of the PIP joint location from the middle of the finger. This limitation was imposed as an anthropomorphic design constraint to sample joint positions near the location of the human PIP joint [47]. The entire sampled range provided stable configuration existing at varying transmission ratios, stiffness ratios and palm lengths. The mean link length ratio for a stable configuration was approximately one, inferring stable link length ratios with anthropomorphic joint positions exist. The transmission ratio was sampled from 0.01 to 1 to avoid kinematical infeasible zero distal radius r_d= 0 and diverging force action lines at $\boldsymbol{R}_i$ > 1 for grasp reliability. The stable parameter space was only 20% of the initial sample space with a mean transmission ratio of $\boldsymbol{R}_i$ = 0.503. A proximal tendon level arm being twice that of the distal tendon lever arm when paired with the mean link length ratio produces an equilibrium point centered in the friction cone for small angles. This alignment is intrinsically favorable for stably grasping objects that are large relative to the palm width. The stiffness ratio was calculated from the anthropomorphic free swing trajectory and transmission ratio. Configurations with a stiffer proximal spring were preferred with a mean K_r= 0.719; this

would decrease if a larger motion envelope ($\Delta\theta_p \gg \Delta\theta_d$) is preferred or increase if a smaller motion envelope ($\Delta\theta_p \ll \Delta\theta_d$) is preferred. Palm width normalized to finger length was sampled from 50% to ensure an object 50% of the finger length could fit within the grasp, to 150%, to ensure symmetric contact of a very small object. There was at least one stable configuration for every sampled palm width, although the transmission ratio, link length ratio and stiffness ration parameters varied. The average normalized palm width was slightly below one, however, optimal solutions discussed in the next section exist slightly higher than this average.

After stable configurations were determined for an object ranging from 0% to 50% finger length, the maximum reliable object size was calculated for each configuration. The solution volume was reduced to a planar representation of varying transmission ratios $\boldsymbol{R}_i$. These specific ratios were chosen because most of the stable solution hull existed within the anthropomorphic constraints. The graph axis compares the link length ratio to the normalized palm width and solution spaces are graded by their respective optimal criteria or combined optimal criteria. For the smallest listed transmission ratio R_1 = 0.42 the local maximum was $\boldsymbol{L}_{obmax}$ = 0.946 and for the largest R_5 = 0.42 the local maximum was $\boldsymbol{L}_{obmax}$ = 1.081. A trend of increasing max reliable object width with increasing transmission ratio was observered. The local optimum solution by transmission ratio occurred at palm widths slightly larger (1.0 < L_{palm}/L_{finger}< 1.1) than the length of the finger. The global optimum $\boldsymbol{L}_{\boldsymbol{obmax}}$ = 1.15 was recorded at the largest transmission ratio R_{opt} = 0.583. Without anthropomorphic sampling limitations, we would expect this value to increase as the allowable palm width and link length ratio increase. It is noted that although there is a favorable correlation for increasing palm width and link length ratio for a given transmission ratio, the local optimum of our model is located at palm lengths near the finger length. Palm designs of similar width to the finger length could be favorable for contact stability in underactuated robotic hands.

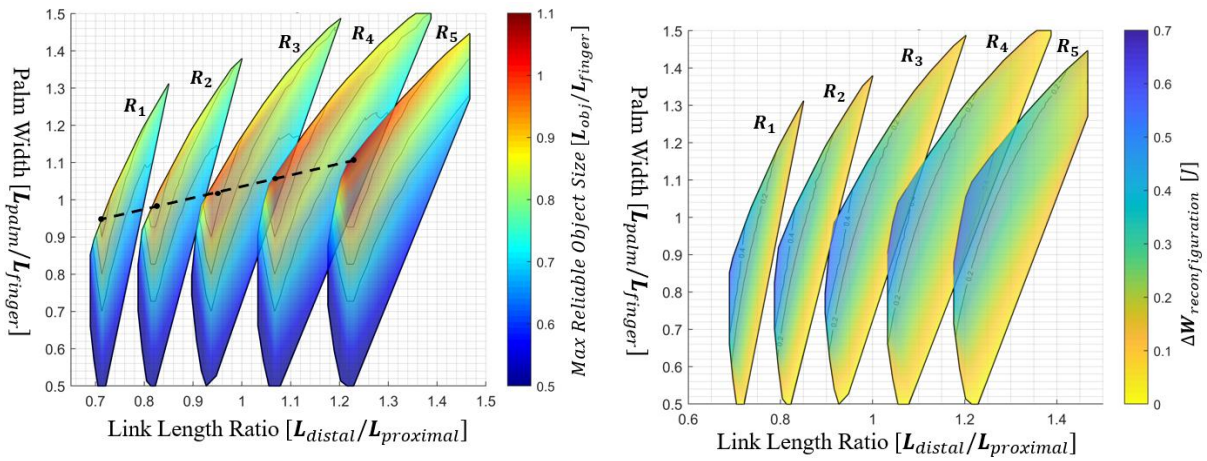

	R_1	R_2	R_3	R_4	R_5
Transmission Ratio $[R_2/R_1]$	0.42	0.45	0.48	0.51	0.54
Normalized Max Stable Object Size	0.946	0.973	1.027	1.054	1.081

	R_1	R_2	R_3	R_4	R_5
Transmission Ratio $[R_2/R_1]$	0.42	0.45	0.48	0.51	0.54
Average Work [J]	0.163	0.151	0.141	0.131	0.133

Figure 11. Results from the maximum reliable object size relative to palm width (left) and the average post contact work for the symmetric configurations (right).

It is noted that the normalization of maximum reliable object width to finger length skews the optimal solution space towards larger palms, which have a greater potential to grasp larger objects because they have a larger initial grasp span. The approximately linear relationship between the design parameters when evaluating max stable grasp span provides a practical guideline of relative palm width, link lengths and transmission ratios for effective two-fingered precision graspers. We can conclude that the wider the range of object sizes that can be reliably grasped improves the quality of the device, especially when it comes to underactuated grippers where precision grasp is typically difficult to stabilize under arbitrary loading conditions in open loop [71].

When calculating post-contact work for the second evaluation criteria, a max actuator force of 60 N was applied, dividing 30 N to each tendon. This force represents a value near the max force production for compact highly geared DC motors commonly found in robotic hands. A reasonably strong proximal spring stiffness $K_p = 0.044\,\frac{N}{m}$ was selected. The post-contact work was simulated for the same transmission ratios R_i for objects that were 0%, 25% and 50% of the finger length.

The minimum average post-contact work by transmission ratio and the global optimum post-contact work were observed for grasping the 50% finger length object. In Fig. 5b, the local average minimum of $\Delta\boldsymbol{W}$ = 0.131 J was observed at R_5, this was also true for the 0% finger length configurations where minimum average $\Delta\boldsymbol{W}$ = 0.407 J at R_5 and at the 25% finger length configurations where minimum average $\Delta\boldsymbol{W}$ = 0.263 J at R_5. The transmission ratio being inversely proportional to average post-contact work was consistent across the three object widths. We believe this because a higher r_d increases the tendon force and excursion required to contact a given object, reducing the required work to reconfigure to a max actuator load. Increased performance with increased object width was also observed. Less finger motion ($\Delta\theta_p, \Delta\theta_d$) to contact an object produces a longer lever arm, reducing reconfiguration because force is less effectively transferred to the object from the actuation tendon. The global minimum for both the 25% and 50% graphs is essentially ΔW = 0 J and is located at the maximum transmission ratio, minimum palm length and largest link length ratio. The contact line, centered in the friction cone, acts as an asymptote in which incrementally larger increases in tendon force are required for an equilibrium point to reconfigure towards this line, reducing the overall magnitude of finger reconfiguration. The low reconfiguration of these solutions indicates that the system is already near a stable position at contact where the equilibrium point is on or approaching the contact line. The combined weighted score from the optimization function is displayed in Fig. 5c. The weighted values for this evaluation were $\boldsymbol{A}_1 = 0.25$, $\boldsymbol{A}_2 = 0.25$ and $\boldsymbol{A}_3 = 0.50$ to equally balance max reliably object width with post-contact reconfiguration. The average $\boldsymbol{C}_{score}$ increased with increasing transmission ratio and the optimal solution was observed to be $\boldsymbol{C}_{score}$ = 0.907. The maximally performing 40% of stable solutions are located in the bounded lines for each transmission ratio, these values were considered for the additional stability testing.

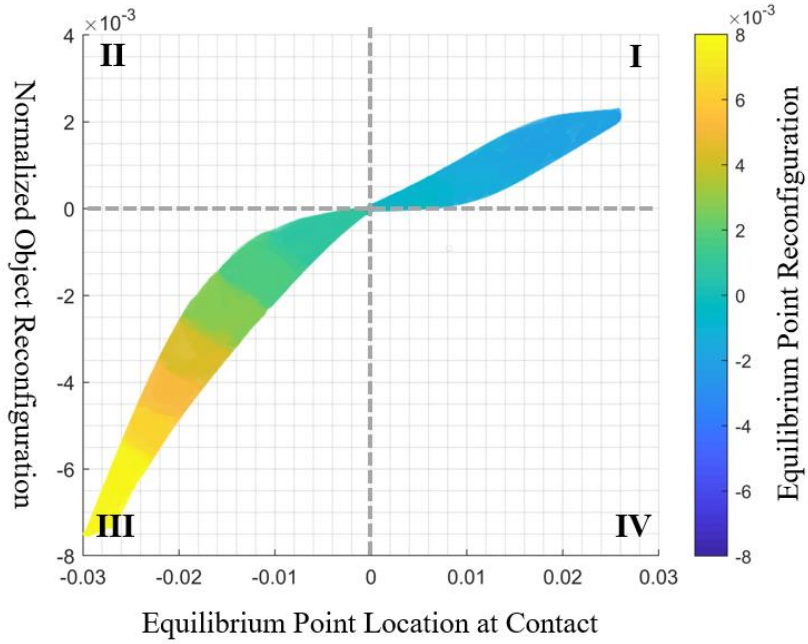

Figure 12. Equilibrium point reconfiguration during grasping trials displaying the nominal contact location and post-contact reconfiguration of the fingers when driven to full actuator load.

Stability of the top 40% of stable solutions from the optimization function were evaluated by applying external disturbances. When evaluating these configurations, the link lengths were determined to be the anthropomorphic basis for the physical values. The finger length was set to 74mm or the size of a small female index finger [47] and the proximal tendon radius was 6mm for practical design considerations. The starting position of the configuration was the acquisition of a 37 mm object that reconfigured to an actuator load of 60 N. Each configuration was radially applied a force in 30° increments until failure criteria were reached. It was seen that all of these configurations were stable to external disturbances being able to resist a minimum of 0.98 N in all directions with the optimal configuration being able to resist 1.85 N in all directions or about 3.1% of the actuator force. A maximum resistible wrench greater than zero verifies that final stable configurations are in force closure and can resist arbitrary external wrenches. This is important to note because a significant amount of the final configurations exist on the hull of the stable solutions. Nominally the configurations were weakest in the $\pm$Y direction to force resistance and

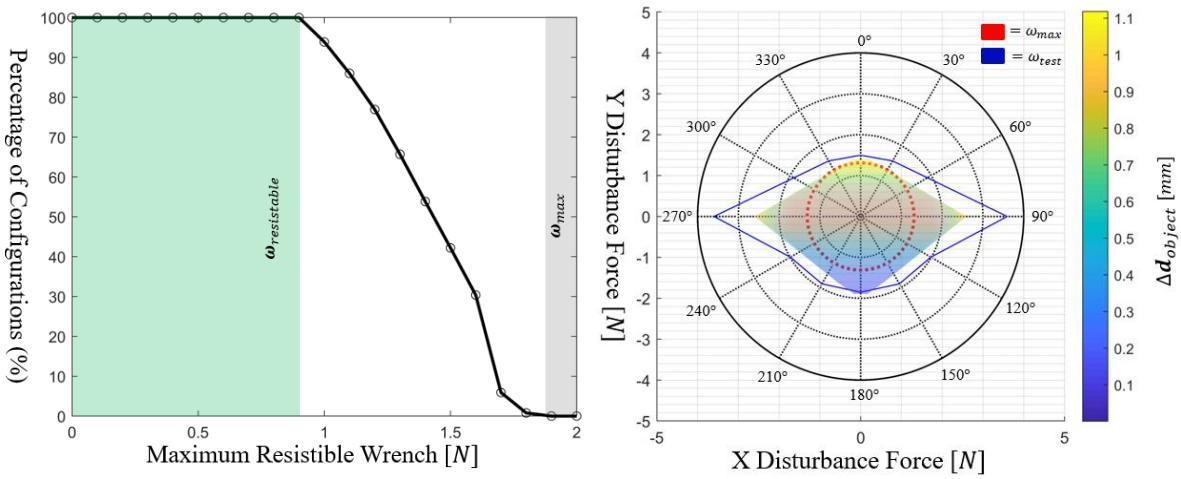

Figure 13. Results of applying external wrenches to the top 40% of stable symmetric configurations (left) including the fully stable range of resistible wrenches and the max resistible wrench. The max resistible configuration was then simulated for its full resistible force profile including results in simulation and from an experimental study.

strongest in the $\pm$X direction. We believe this is because the slipping failure mode was the most common, and given the initial configuration vertical disturbance forces were more likely to move the contact force vector $\vec{\boldsymbol{F}}_c$ out of the friction cone. Reconfiguration of the object and equilibrium point location were plotted to further understand how the system would adjust to additional actuator force. In quadrants I and III, It was seen that for all solutions the object reconfigured towards the equilibrium point. No solutions existed in quadrants II and IV which would display an object reconfiguring away from the equilibrium point with force, heading towards unstable finger poses. We can assume these configurations will remain stable with additional actuator force because the contact force line of action acts as a kinematic force asymptote and our solution space is reconfiguring towards this asymptote.

A sample configuration in the top 40% of maximally performing solutions was simulated and experimentally tested for external wrench resistivity (Fig 6C). The simulation provided stable resistance of approximately 2.5 N in the $\pm$X directions while resisting 1.3 N in the +Y and 1.9 N in the -Y directions. The minimal resistible wrench of this configuration in simulation was 1.31 N,

approximately 2.2% of the actuation force. The physical test displayed an external disturbance profile similar to that of the simulation that was slightly elongated in the X directions. The gripper saw a stable resistance of approximately 3.5 N in the $\pm$X directions, 1.5 N in the +Y direction and 1.8 N in the –Y direction. The minimal resistible wrench of this configuration was 1.53 N which was similar to the 1.31 N of the simulation. Although the profile was similar, the average error between the simulated and experimental results was 22%. This can be primarily attributed to a slightly higher coefficient of friction and difficulties of visually assessing slip in the horizontal configuration where rolling instead of slipping tends to occur. These results are rather substantial as the gripper was able to withstand applied object disturbances nearly five times the weight of the initial 30 gram object in all directions and nearly times the initial weight in the X direction.

When planning to manipulate, knowing the direction of maximum force resistance is favorable to orient the gripper such that loading is applied in the direction of maximal disturbance resistance. For example, when navigating with an already grasped object one could orient the gripper with the direction of max resistance facing potential collisions. Additionally, when grasping and transporting a heavy object it would be beneficial to orient the gripper such that the system could optimally resist gravity.

3.4 Asymmetric Optimization Results

The asymmetric optimization was completed in a similar multi-step constrained optimization investigating maximum reliable object width and post-contact work for a variety of object sizes. The parameter search was extended to seven independent variables for the for (r_{Fd},r_{Td}, L_{Fd},L_{Td}, L_{palm}, θ_F, θ_T), bounded by initial sampling constraints on anthropomorphism and kinematic feasibility, was conducted to determine stable configurations using gradient descent of a constrained nonlinear multivariable function in MatLab. Anthropomorphism was considered

when implementing the rest angles of the left, forefinger equivalent, and right, thumb equivalent, fingers. Object contact was still considered about the center of the palm, requiring significantly more motion in the forefingers than the thumb which is consistent with human precision grasping. Although the motion of each finger was different, the free swing trajectory $\boldsymbol{c}_{fs}$ was consistent with the symmetric trials. This caused the force in the forefinger and thumb tendons to differ and as a result required a larger thumb pulley radius to account for less thumb motion. To avoid a brute force approach to the optimization, thumb pairs were created for each forefinger configuration during the parameter search that contact the forefinger and have the equilibrium point centered in the friction cone at contact. This was done to avoid infeasible configurations that never contact one another or are far from post-contact stability. The offset in initial finger angles from vertical increased the grasp span width relative to the palm width. The maximum reliable grasp span was then evaluated at the initial grasp span, allowing objects to be grasped that were greater than the width of the palm. The weighted configuration performance used to determine optimal solutions, C_{score}, was calculated in the same manner as the symmetric optimization using the maximum reliable grasp span and the post-contact work.

Given our initial symmetric model, 0.1% of tested configurations (n = 3.2 million) remained stable for an object size of 0% to 50% finger length in the bounded parameter search (Table 1). Given our initial asymmetric model, 0.008% of tested configurations (n = 28.8 million) remained stable for an object size of 0% to 50% finger length assuming the generated thumb provided contact and stability. We attribute this lower percentage of stable configurations for the asymmetric testing to two factors. First, given the anthropomorphic constraints on the forefinger, generated thumb and palm width, many configurations did not have a feasible thumb inside the kinematic constraints to match the sampled forefinger. Second, some of the simulated “objects” had too large

Table 2. Final Asymmetric Kinematic Parameters

Parameter	Stable Reconfiguration (0% to 50% L_f)					
	Min	***Mean***	***Max***	***Range***	***Tested***	***Local***
Transmission Ratio (R_2/R_1)	0.083	0.233	0.550	$[0.083 - 1]$	0.0833	0.077
FF Joint Position (L_2/L_1)	0.682	0.831	1.450	$[0.68 - 1.45]$	0.682	0.514
FF Stiffness Ratio (K_2/K_1)	1.273	3.585	8.400	$[0.01 - \infty]$	8.400	9.130
Transmission Ratio (R_4/R_3)	0.025	0.054	0.066	$[0.01 - 1]$	0.055	0.049
T Joint Position (L_4/L_3)	1.098	1.099	1.100	$[0.9 - 1.1]$	1.100	1.100
T Stiffness Ratio (K_4/K_3)	10.63	13.35	28.11	$[0.01 - \infty]$	12.623	14.220
Initial FF Angle (θ_{FF})	50.00	50.51	70.00	$[50 - 70]$	50	55
Initial T Angle (θ_T)	10.00	15.83	30.00	$[10 - 30]$	20	18
Normalized Palm Width (L_p)	1.243	1.456	1.500	$[0.5 - 1.5]$	1.456	1.473

of an initial tilt – due to large variance in the forefinger and thumb instantaneous velocity – leading to slip in the hand-object system.

The mean and optimal link length ratio for a stable asymmetric configuration were fairly close being low for the forefinger (opt = 0.682 μ = 0.831) and slightly higher for the thumb (opt = 1.1 μ = 1.09). We found that these aligned fairly closely with the index PIP joint location and thumb IP joint location in human hand with the index proximal link being slightly shorter and the thumb proximal link being slightly longer. The generated thumb was also recorded to be slightly shorter (86.5%) on average than the sampled forefinger with a normalized length. We believe the asymmetric joint locations vary from each other and the symmetric solutions due to the varying initial angle constraints $(\theta_{Fi}, \theta_{Ti})$ for the asymmetric testing. We must note that due to the complexity of human finger actuation we did not expect our single actuation model to reflect anthropomorphic solutions that were favorable. Solutions did exist across most joint locations, however, our optimal solutions may provide insight into the underactuated nature of the human hand.

The transmission ratio was sampled from 0.01 to 1 to avoid kinematically infeasible zero distal radius r_d= 0 and diverging force action lines at R_i > 1 for grasp reliability. For the asymmetric

configurations, the mean transmission ratio was rather low for both the forefinger (μ = 0.233) and thumb (μ = 0.054). These low values are representative of the larger required finger joint angles to contact a given size object when compared to symmetric. This is because the starting angles widened the initial finger span relative to the symmetric case requiring additional motion to grasp objects of a given size. This finger configuration requires the equilibrium point to be closer to the joint for the system to remain stable. Variations in object tilt and joint location required the forefinger equilibrium point to be further from the joint than the thumb to provide a viable grasp.

The stiffness ratio was calculated from the anthropomorphic free swing trajectory and transmission ratio. For the asymmetric case, the mean stiffness ratio was very high for the forefinger (μ = 3.585) and thumb (μ = 13.35). We believe that this was to balance the motion from the relatively low transmission ratios for both fingers. The palm length for the asymmetric case (μ = 1.456) was larger on average than the symmetric case. This is because a larger range of motion with a fixed anthropomorphic free swing trajectory caused the instantaneous velocity of the fingers to displace laterally instead of palmar and laterally in the symmetric case.

After stable configurations were determined for an object ranging from 0% to 50% finger length, the maximum reliable grasp span was calculated for each configuration. For the asymmetric case, we decided to evaluate the kinematic parameters comparatively (Fig 5B) to more succinctly describe how relative forefinger-thumb design decisions affect our heuristics. We found that larger objects can be grasped at lower forefinger angles across the entire range of thumb angles. The most favorable configurations existed in the middle of the thumb solution space around 50˚ for θ_{Fi} and 20˚ for θ_{Ti}. Due to the low variance in both joint position and transmission ratio for the generated thumb, we found successful configurations with lower forefinger transmission ratios and link length ratios were ideal. Similar stiffness between the forefinger and thumb distal links provided

advantages for grasping larger objects. We believe a shorter distal link helped the forefinger take more of the reconfiguration burden allowing less object motion relative to joint angle rotation. Lower stiffness values allowed the hand to exert more force on the object across the entire grasp span. Many of the final configurations were able to grasp objects from infinitesimally small to greater than the palm width with the maximum being L_{objmax}/L_{finger} = 1.26 times the original palm width or approximately equal to the starting grasp span. Similarly, we observed this for the symmetric configurations where the equilibrium point had good alignment with minimal reconfiguration across the free swing of the finger.

The approximately linear relationship between the design parameters when evaluating max stable grasp span provides a practical guideline of relative palm width, link lengths and transmission ratios for effective two-fingered precision graspers. We can conclude that the wider the range of object sizes that can be reliably grasped improves the quality of the device, especially when it comes to underactuated grippers where precision grasp is typically difficult to stabilize under arbitrary loading conditions in open loop.

When calculating post-contact work for the second evaluation criteria, a max actuator force of 60 N was applied, dividing 30 N to each tendon. This force represents a value near the max force production for compact highly geared DC motors commonly found in robotic hands. A reasonably strong proximal spring stiffness K_p = 0.044 $\frac{N}{m}$ was selected. The post-contact work was simulated for the same transmission ratios R_i for objects that were 0%, 25% and 50% of the finger length.

For the asymmetric results in Fig. 6, the variation in performance based on relative kinematic parameters was less defined. Solutions on the hull of the space tended to perform significantly worse that those in the center of the solution space, forcing most of the solution space to be similar and viable in post contact work performance. For the 0% finger length object configurations the

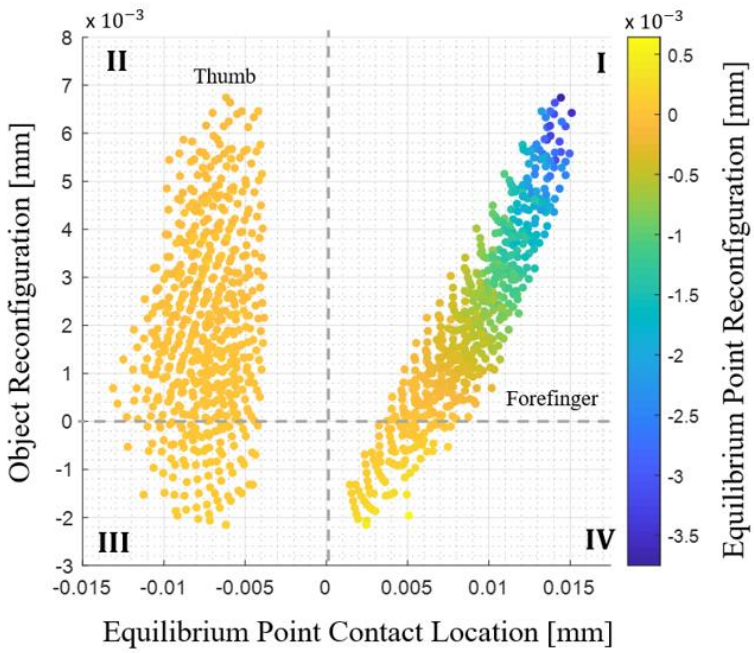

Figure 14. Equilibrium point reconfiguration during grasping trials displaying the nominal contact location and post-contact reconfiguration of the fingers when driven to full actuator load for asymmetric configurations.

average post contact work for all configurations was ΔW = 0.750 J with the global minimum being essentially ΔW = 0. For the 50% finger length object configurations the average post contact work for all configurations was ΔW = 15.48 J with a global minimum of ΔW = 6.16 J. The asymmetric nature created larger reconfigurations for a given increase in actuator force because of the heavily varying instantaneous velocities and trajectories of the two fingertips when compared to the symmetric configurations. The solution space was less homogenous than the symmetric solution space with bifurcations occurring on the solution space hull where large reconfigurations would occur.

The combined weighted score from the optimization function is displayed in Fig. 5C. The weighted values for this evaluation were $A_1 = 0.25$, $A_2 = 0.25$ and $A_3 = 0.50$ to equally balance max reliably object width with post-contact reconfiguration. For the symmetric case, the average C_{score} increased with increasing transmission ratio and the optimal solution was observed to be

C_{score} = 0.907. For the asymmetric case, most of the value was derived from differences in the maximum reliable object width and the optimal solution was observed to perform well in all three weighted categories with a C_{score} = 0.965. The maximally performing 40% of stable solutions are located in the bounded lines for each transmission ratio, these values were considered for the additional stability testing.

Stability of the top 40% of stable solutions from the optimization function were evaluated by applying external disturbances. When evaluating these configurations, the link lengths were determined to be the anthropomorphic basis for the physical values. The finger length was set to 74mm or the size of a small female index finger and the proximal tendon radius was 6mm for practical design considerations. The starting position of the configuration was the acquisition of a 37 mm object that reconfigured to an actuator load of 60 N. Each configuration was radially applied a force in 30° increments until failure criteria were reached.

The asymmetric cases were also all able to exert a maximum resistible wrench greater than zero, with a minimum resistance of 0.16 N and a maximum of 4.17 N or about 6.8% of the actuator force. Nominally the configurations were weakest in the +Y and -X directions which caused the object to eject from either a loss of force (flagged as mainly X direction failures) or slip (flagged as mainly Y direction failures). The force resistance direction that was strongest was in the +X direction towards the thumb. This was due to generated thumb having an equilibrium point near the antipodal force line, providing additional stability in this direction. The asymmetric configurations had a higher optimal resistible wrench than the symmetric configurations and this could be attributed to the stiffer distal springs as most failures were attributed to significant buckling or collapsing of the distal link for both symmetric and asymmetric cases. The asymmetric

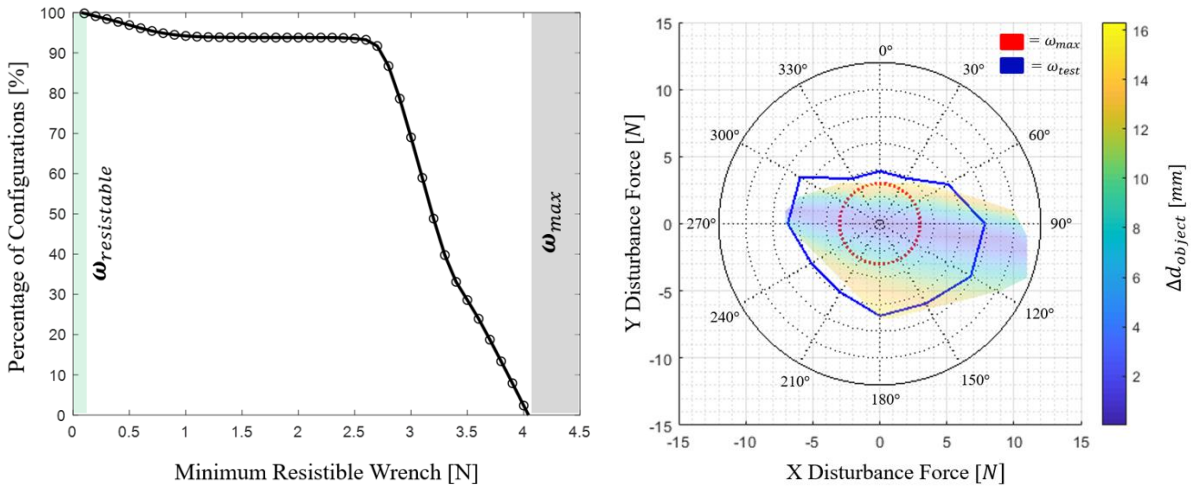

Figure 15. Results of applying external wrenches to the top 40% of stable asymmetric configurations (left) including the fully stable range of resistible wrenches and the max resistible wrench. The max resistible configuration was then simulated for its full resistible force profile including results in simulation and from an experimental study.

case also had a larger range of possible resistible wrench by configuration which we attribute to the larger solution space for favorably performing configurations.

In Fig. 7B, reconfiguration of the object and equilibrium point location were plotted to further understand how the asymmetric configurations would adjust to additional actuator force. The asymmetric forefinger also shows that the equilibrium point is reconfiguring towards the force asymptote. This is seen with the horizontal inflection line, between I/II and III/IV, inverting the object reconfiguration and equilibrium point reconfiguration values. In the asymmetric case the equilibrium point contact location can be above or below the object center because the object can easily tilt. The thumb and forefinger indicating two separate vertical regions indicates that its favorable for a slight object tilt during reconfiguration. The thumbs had approximately zero reconfiguration when increasing actuator force after contact because they were generated with the equilibrium point on the force asymptote. This could be leveraged for interesting hand designs, such as high stiffness thumb configurations that caused either zero object reconfiguration or pure rotation about the thumb contact area. Less stiff thumbs were still able to reconfigure with little

equilibrium point reconfiguration. In the future, we would like to investigate constraints that can be placed on the generated thumb to perform different manipulation tasks with reconfiguration.

A sample configuration in the top 40% of maximally performing solutions, parameters displayed in Table 1 and test setup in Fig. 4, was simulated and experimentally tested for external wrench resistivity (Fig. 8). The asymmetric simulation provided a stable resistance of approximately 15.8 N in the +X direction, 10.4 N in the -X direction, 4.1 N in the +Y direction and 10.2 N in the -Y direction. The physical testing of a gripper with the given kinematic parameters provided a stable resistance of 12 N in the +X direction, 10.5 N in the -X direction, 6 N in the +Y direction and 7 N in -Y direction. The minimum resistible wrench of the simulation was 4.1 N compared to 5.9 N for the experimental evaluation. We believe this error was decided from the gripper slightly outperforming the simulation in the +Y direction. The average error between the simulated and experimental asymmetric results was 15.8%.

The higher error observed in the X-direction can be attributed to difficulties in visually assessing slip in the horizontal configuration where rolling and rotation instead of slipping tends to occur. These values could also be confounded by an imperfect estimate of the friction coefficient between the fingers and the object. When planning to manipulate an object, it is favorable to know the direction of maximum force resistance so the operator can orient the gripper such that external loading is applied in the direction of maximal disturbance resistance or so that gravity is optimally resisted.

3.5 Conclusions

In this chapter, we determined optimal kinematic parameters for a range of symmetric and asymmetric precision gripping configurations. A heuristically optimal set of link lengths, palm length, transmission ratio and spring stiffness ratios from the asymmetric optimization were

implemented in a new version of the prosthetic hand. This version uses a tripod precision grasp so both the index and middle finger were fabricated with identical kinematic properties and directly oppose the motion of the thumb. Starting angles were set with hard stops on each of the fabricated fingers and the palm length was set as the distance between the center of the thumb and forefinger revolute joints. We believe, that although this may not maximize grasp force, this kinematic configuration will allow us to reduce post contact motion and increase resistance to external wrenches when picking and placing objects in precision grasp.

IV. INVESTIGATING FINGER PAD GEOMETRY

In the initial testing of the prosthetic hand prototype, we ran into issues creating enough contact area to successfully lift large heavy objects due to the thin rounded finger pads. Prosthetic and robotic grippers rely on these soft finger pads to better acquire objects of varying size, shape and surface. However, the frictional behavior of soft finger pads of different designs and geometries have yet to be quantitatively compared, in large part due to the difficulty in modeling soft contact mechanics. In this chapter, we experimentally examined the frictional behavior of several common primitive contact geometries in terms of their performance under shear loads that would tend to cause the contact to slip and the grasp to potentially fail. The effective static and kinetic coefficients of friction were recorded for each finger pad under a range of common grasping loads. The results show that the variance in contact curvature, contact patch geometry and pressure distribution have influences on key parameters for grasping at low forces. The advantages and disadvantages of these simple geometries are discussed for design of single finger, multi-finger and manipulation-based robotic hands.

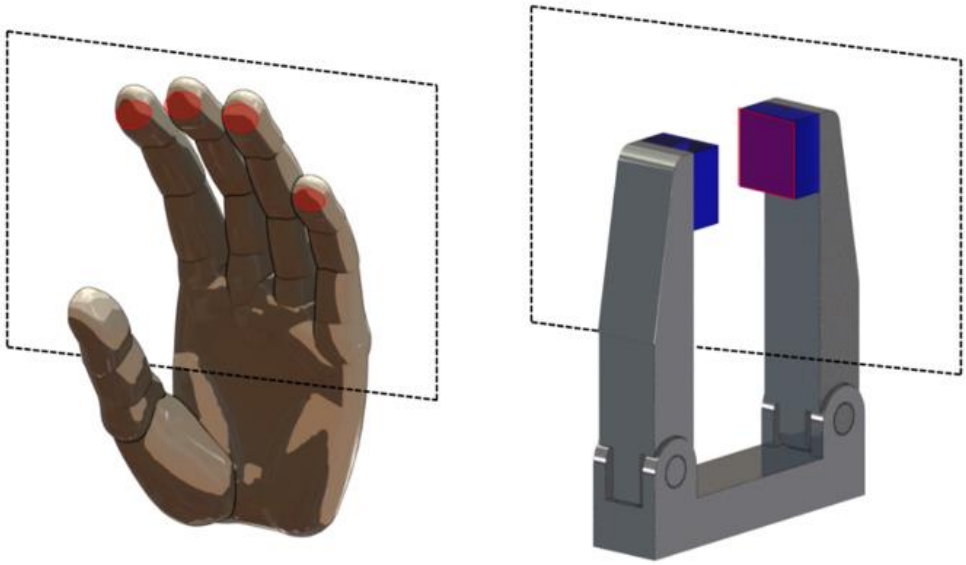

Figure 16. Example of the elastic contact areas touching a planar surface for a hand and robotic gripper.

4.1 Background on Robotic Finger Pads

General-purpose robotic and prosthetic hands and grippers typically utilize a small set of common fingertip designs: hemispherical, flat, or cylindrical [75-77]. These common geometries, the underlying structure generally fabricated from smooth metals or plastic, are often covered with soft rubber-like finger pads to improve the stability of the contact through high friction [78]. However, the performance of these basic fingertip and finger pad geometries have yet to be quantitatively analyzed and compared to one another. In this paper, we experimentally compare the frictional performance of these three basic finger pad geometries as a function of their size, contact geometry and loading conditions.

The effectiveness of soft elastic finger pads in grasping environments is dependent on the object stability maintained while grasping. The local contact geometry and friction coefficient are key aspects to determining the stability of an antipodal precision grasp or multi-contact wrap grasp used commonly in modern robotic hands [78]. To ensure that the grasp of an object remains stable, the

hand-object system must remain stable by either satisfying force closure [12] or by sufficiently caging the object within the gripper [79]. Simple point contact coulomb friction models are generally sufficient for determining object stability for contact between a rigid finger and object. However, this is complicated in elastic models where contact is distributed over an area and pressure distributions can be non-uniform. Hertzian contact mechanics initially focused heavily on frictionless relationships, analyzing the close-form solution of stresses and displacements to linear elasticity equations [80], which alongside experimentation led to several models that can describe frictional properties of soft materials [81]. Although there has been significant progress in the modeling of elastic contact [82-83], the approaches taken are still very much incomplete and require significant computational time for simple structures. Furthermore, the complexities and uncertainty in robotic grasping have proved to be an additional challenge for designing generalizable soft finger pads.

Many experimental approaches have been made to fabricate effective finger pads for robotic hands to overcome the difficulty of modeling soft contacts. Designs are split between complex finger pads that are experimentally optimized for a discrete subset of objects or tasks [84-85], or simple geometric shapes, that provide an intuitive framework for grasping [75-77], planning [86] and learning [87]. These finger pads, primitive or complex, are either iterated through virtual evaluation or experimental evaluation. For virtual evaluation, a set of virtual objects in the form of point clouds or tessellated surfaces are first simulated [88]. These virtual objects are used to plan antipodal grasps for parallel or multi-fingered grasps [86-87] during the finger pad optimization. When creating optimal finger pads given specific gripper kinematics, the goal is to maximize the contact and force between local object geometry and finger pad geometry [79] [89-90]. Similarly, in an experimental setting a finger pad is produced and a sample set of objects are grasped. The

effectiveness of the gripper is determined by the amount of objects the gripper can successfully pick and place, nominally using a multi-fingered hand and a robotic arm [90-91]. However, there is limited research evaluating the performance of finger pads alone, the analysis of which is necessary for creating more advanced grippers architectures.

In this paper, we set out to experimentally compare the frictional properties of three common finger pad shape primitives seen in research and commercial hands [75-77]. Due to the variability in gripper kinematics, architecture, and object geometry seen in robotic grasping applications, we use a simplified experimental framework consisting of a single contact loaded vertically on a flat contact surface mounted to a high-resolution force sensor. This contact surface is then displaced laterally, and the normal and tangential force profiles are recorded, from which effective coefficients of static and kinetic friction are calculated. The finger pad sizes are selected such that they produce contact areas matching those of the human index finger at three different orientations. The performance of these grip pads were then compared to each other and the human finger pad to provide insight into developing effective artificial finger pad geometries for robotic grasping applications.

4.2 Key Parameters and Experimental Model

Elastically deformable objects create a variety of contact area geometry and pressure distributions depending on the object's initial geometry, the loading and the half space the object is in contact with [82]. We selected three common primitive finger pad geometries used in research and commercial hands: a cube, a cylinder and a sphere, and modeled those geometries as a single finger pad in contact with a normal planar half space "surface". These finger pad geometries create unique contact areas (square, rectangle, and circle) and unique pressure distributions when loaded onto an elastic or rigid half space [82]. Assuming a point load centered on the finger pad, elastic

cubic objects distribute the loading pressure heavily towards the edges whereas elastic spherical objects distribute pressure towards the middle of the contact surface area. A cylinder is a mix of these two geometries and creates a pressure that distributes force toward the center of the rounded profile and towards the edges of the cylinder length [82]. We would like to experimentally determine how different key variables, including the loading magnitude, contact geometry and contact area, vary parameters that are key to robotic grasping applications.

Due to the variability in gripper kinematics, architecture, and object geometry seen in robotic grasping applications, we simplified our experimental framework to model the interaction of a single finger pad and a flat rigid half space. Although this model may be simple, we believe it is an accurate representation of a generic grasping scenario between a digit in a multi-fingered hand and the face of an object. When determining whether an object can be grasped by an elastic finger pad, one must ensure that the force is exerted within the friction cone. The larger the friction cone, the more likely the given kinematics of a hand-object system can produce a stable grasp across antipodal points [78]. We assume a simple Coulomb model of friction where the holding force $F_{Friction}$ is less than or equal to the coefficient of friction μ multiplied by the normal force F_{Normal} while the pad and object are static. Similarly, the object and fingertip begin stably sliding when the holding force equates to the coefficient of friction multiplied by the normal force.

$$F_{Friction} \leq \mu_{Static} F_{Normal} \tag{1}$$

$$F_{Friction} = \mu_{Kinetic} F_{Normal} \tag{2}$$

For elastic structures such as Silicone and the human finger pad, tribological literature describes the coefficient of friction as nonlinear, varying in a negative power law relationship with the applied normal force [92-94]. This deviation from Admontons' laws of friction states that there

are nonlinear variations of the coefficient of friction with surface area and applied loads for elastic deformable materials.

$$\mu_{Static} = a(F_{Normal})^{n-1} \tag{3}$$

Where a and n are constants and the coefficient of friction decreases with applied load for flat rigid surfaces. Additionally, the surface level effect of adhesion, $F_{Adhesive}$, also provides the ability to add to the normal force and is observed for different surface materials, temperatures, humidity and pressure variations [92]. In this paper, we characterize this adhesive force as being influenced by our design variables (geometry, pressure) while minimizing effects from variations in materials, temperature and humidity. Under this model, finger pads with a higher coefficient of friction for a given surface area and loading are considered more effective because they create a wider friction cone, providing more holding force before slip and resistance to external wrenches after a successful grasp [78]. This holds for multi-fingered systems commonly seen in robotic grasping, however, other kinematic properties such as force direction at contact, antipodal point locations and caging configurations can alter grasp performance.

$$\mu_{Static} - \tan(\theta_{obj}) \leq \frac{|F_{cy}|}{|F_{cx}|} \leq \mu_{Static} + \tan(\theta_{obj}) \tag{4}$$

$$P_{F-O} = \frac{F_{Normal}}{A_{Contact}} \tag{5}$$

Where μ_{Static} is the static coefficient of friction, F_{cx} and F_{cy} are the x and y components of the contact force and θ_{obj} is the relative orientation of the object and the applied force. Because our test setup is a single finger pad that is orthogonally loaded, we can assume that the θ_{obj} is zero and that the contact holding pressure, P_{F-O}, is equal to the normal force divided by the finger pad contact area, $A_{Contact}$.

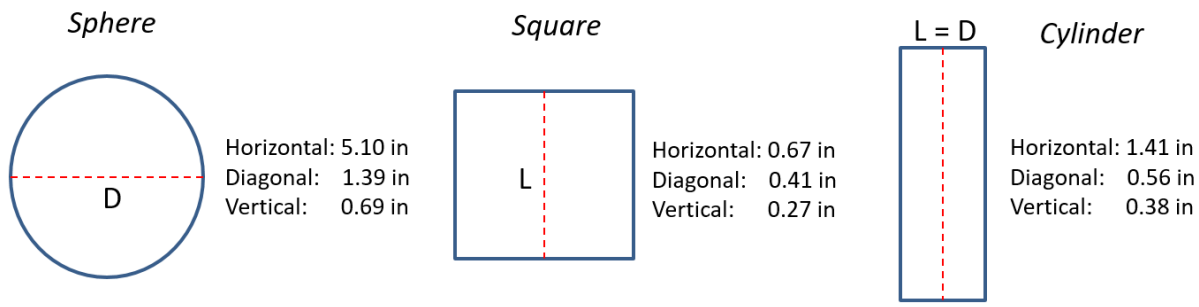

Figure 17. Final pad characteristic lengths for each of the three primitive geometries evaluated.

4.3 Fabrication of Primitive Geometry Finger Pads

A pipeline was created to measure the human index finger pad contact area in the horizontal, diagonal and vertical positions under a common loading to provide three unique target contact surface areas for the artificial primitive geometries (Fig. 2). Although there is a sufficient amount of information available when it comes to the frictional properties of the human finger pad [92][95-96], the exact relationships between finger orientation and loads that we are interested in for robotic grasping were not comprehensibly reported. While the peak grasp force of the human hand can be more than 75N [97], we decided on a common loading of 12.5N or approximately half the nominal force output of the human finger force across all ages [98]. The finger pads contact area were equated at a single loading force because it would be impossible to equate a sphere, which converges to a point contact at arbitrarily low force, to a cylinder, converging to a line contact, and a cube, converging to a surface. Thus, when comparing lower forces, we can assume contact area does vary between the finger pads, however, minimal contact area variation will occur for loads higher than the common load assuring there is no plastic deformation or yielding. It is noted that the normalized contact area could have been any arbitrary area, however, we aimed to create finger pads with easily relatable geometries, rigidity and thickness that allow us to compare and contrast them from the human finger pad.

A single participant with approximately a 50th percentile male sized hand transferred his fingerprint (EZ ID #3 Ink) to a graph paper on top of a load cell. The applied loading force was gradually increased in real time until the loading threshold was met. A custom orthosis with a digital angle gauge (Wixey Digital Angle Gauge) was attached to the finger to ensure the correct orientation (0°, 45°, 90°) was maintained during contact and loading. This graph paper was then scanned in high resolution and the ink finger print was isolated from the background grid. The grid lines were used to normalize the pixel width to millimeters allowing us to calculate the area using the prints convex hull because all three orientations provided fingerprints that were ovular and convex in shape as seen in Figure 2. Each finger orientation was recorded one hundred times and the average surface areas were recorded in Table 1.

A similar pipeline was used to create the nine artificial finger pads consisting of three primitive geometries at the three predetermined contact areas. The artificial finger pads were fabricated out of a silicone rubber (Smooth-On Dragonskin 30A) that is a similar durometer to the human finger pad [100] and the surface was a quarter inch acrylic (PMMA). A single combination of object and finger pad material were selected to maintain a consistent relationship between coefficients of friction during testing. The thickness of the pads varied based on size, with the large pad resembling the horizontal orientation at 4mm thick, the medium pad at 3mm thick and the small pad at 2mm thick to resemble the distal human finger pad [100]. Each finger pad was experimentally evaluated using the fingerprint loading pipeline above until the surface area fell within 5% of the estimated human index contact area for each given orientation. The finger pads were then characterized by their largest linear dimension. The cubic finger pads are characterized by side length L, the spherical finger pads by the diameter D, and the cylindrical finger pads by the diameter D that was set equal to the length L for this study. The nine finger pads were each

molded directly onto a rigid mounting block that was screwed onto the testing apparatus described in the next section (Fig. 3). It is noted that the vertical edges for the cube and cylinder edges were only one millimeter thick to mitigate excessive deflection of the pad while sliding and the cylindrical and spherical pads were created in halves so that they could be more easily mounted to the loading axis. We believe that these modifications improved the consistency of the kinetic and static coefficients of friction during testing.

4.4 Testing Procedure

A testing apparatus was developed to align with the ASTM D1894 standard [91] providing guidelines for evaluating the effective static and kinetic coefficients of friction for thin elastic materials. Although this standard is not explicitly designed for the evaluation of artificial finger pads, we found it to be the closest fit for our testing. The sphere was slid in a single direction, the cube was slid along its edge and the cylinder was tested in both the radial and axial directions. We established five loads that are representative of robotic grasping conditions to evaluate the static and kinetic coefficients of friction for the primitive robotic finger pads. The chosen loading magnitudes describe full force (25N), half-force (12.5) and low-force (1N, 2N, 5N) measurements relative to estimated human finger force production [98]. The low force range of 2N and 5N were recorded because they are critical for determining the power law relationship between loading and coefficient of friction seen in the human finger and elastic materials [92]. It is noted that although these normal loads are representative of robotic grasping, the finger pads were only loaded vertically and do not have the same force-position relationships as a normal robotic hand.

For a given trial, the finger pad was mounted to a mechanical optical micrometer with high resolution and a normal load was applied to a quarter inch thick acrylic sheet that was mounted on a six-axis load cell (ATI). The load was applied gradually to minimize viscoelastic effects and the

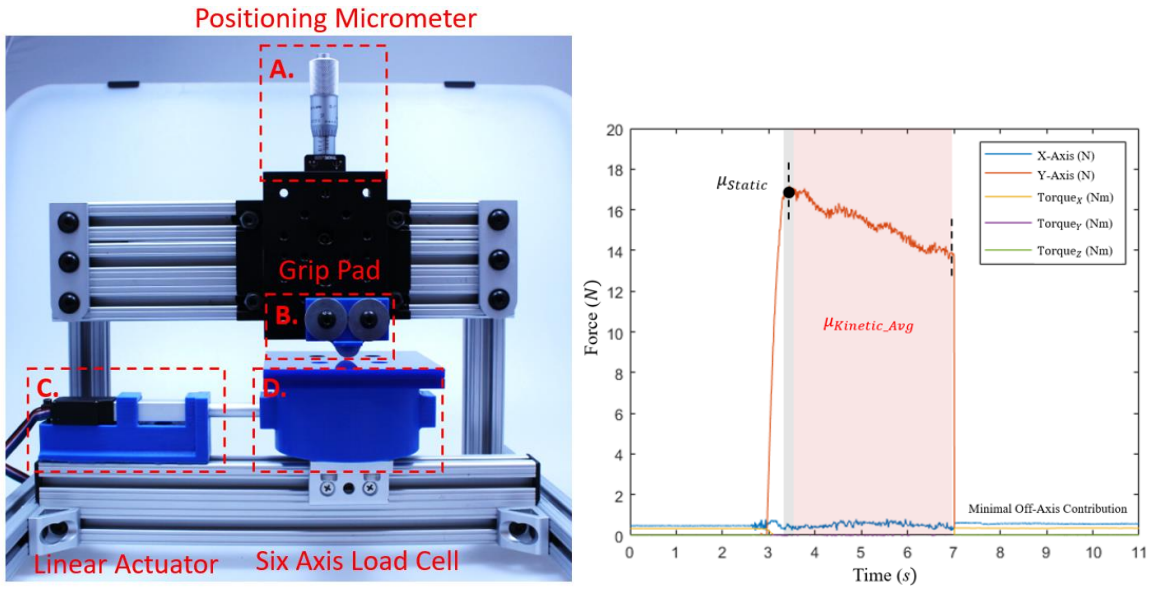

Figure 18. (Left) Testing apparatus including the positioning micrometer to apply a load, the mounted grip pad, the linear actuator driving pad motion and a six axis load cell. (Right) A sample output from a test extracting the static and kinetic coefficients of friction relative to the applied load.

micrometer stage was locked before sliding was forced. A linear actuator (Firgelli L12-50-210) was used to horizontally drive the loaded acrylic surface mounted on low friction rails across the finger pads. The linear actuator was driven at a load exceeding the static friction limit at the ASTM prescribe rate of 150 mm/sec. This fast driving rate helped avoid stick-slip behavior improving the isolation and classification of the coefficient of kinetic friction. We confirmed that the linear actuator was strong enough for the vertical loading to have negligible effects on the sliding rate of the acrylic surface. The static friction coefficient was determined as the maximum ratio between the frictional and loading force. The kinetic friction coefficient was the average ratio between holding and loading force while the pad was stably sliding over the surface (Fig. 4). These calculations and more details on the testing procedures are described in [91].

Additional precautions were taken above the ASTM standards when preparing the robotic geometric primitives and test setup. First, the room temperature and humidity was recorded because it had a significant effect on the coefficient of friction for smooth materials [94-96]. The

testing was completed in a climate-controlled room with minimal variance in temperature and humidity. Next, before each primitive was tested, both the acrylic half space and primitive surface were cleaned with a 70/30 isopropyl alcohol solution to remove any dust or surface contaminants. The pads were molded with a smooth molding surface (Stratasys Objet30 Pro VeroClear) to ensure consistency and to remove ridges that occur from machined or FDM 3D printed molds. Last, the pads were removed after molding and adhered with a specialty super glue (Loctite 4471) designed with high shear strength to mitigate variations in pad adhesion to the supporting 3d printed chassis.

4.5 Experimental Results

To normalize the contact surface area of the fabricated primitives, the contact area of the human index finger of a single participant (Male 26, approx. 50th percentile male [47]) was used under a common load of 12.5N in the horizontal, diagonal and vertical orientations. The measured horizontal, or finger in plane with the surface contact, surface area was 311.11 mm^2 with a standard deviation of 17.96 mm^2. The measured diagonal, or finger 45 degrees offset from the surface plane, contact area was 103.14 mm^2 with a standard deviation of 10.81mm^2. The measured vertical, or the finger 90 degrees offset from the surface plane, contact area was 60.12 mm^2 with a standard deviation of 4.61 mm^2. All three contact geometries were ovular, in the horizontal orientation largest linear dimension is in the y-axis, in the diagonal orientation it is approximately circular and in the vertical orientation largest linear dimension is in the x-axis (Fig. 2). The surface area and largest linear dimension for the human index finger and fabricated primitive finger pads are recorded in Table 1.

The fabrication of the final nine finger pads for testing were revised until their contact areas were within one standard deviation of the human index finger contact area ($F_N = 12.5$N, $n_{samples} = 100$) . This deviation was to account for variations from the molding and loading

Table 3. Finger Pad Surface Areas at 12.5N Contact Force

Pad Type	Contact Surface Area by Orientation		
	Horizontal (0° x 4mm)	***Diagonal (45° x 3mm)***	***Vertical (90° x 2mm)***
Human Index	$A = 311.11\ mm^2$ $\sigma = 17.96\ mm^2$	$A = 103.14\ mm^2$ $\sigma = 10.81\ mm^2$	$A = 60.12\ mm^2$ $\sigma = 4.61\ mm^2$
Cube	$A = 315.48\ mm^2$ $\sigma = 12.84\ mm^2$ $L = 17.02\ mm$	$A = 109.60\ mm^2$ $\sigma = 5.94\ mm^2$ $L = 10.41\ mm$	$A = 60.00\ mm^2$ $\sigma = 5.72\ mm^2$ $L = 6.86\ mm$
Sphere	$A = 304.52\ mm^2$ $\sigma = 20.34\ mm^2$ $D = 129.54\ mm$	$A = 107.74\ mm^2$ $\sigma = 2.41\ mm^2$ $D = 35.31\ mm$	$A = 59.35\ mm^2$ $\sigma = 4.34\ mm^2$ $D = 17.53\ mm$
Cylinder	$A = 300.64\ mm^2$ $\sigma = 17.33\ mm^2$ $L{=}D = 35.8\ mm$	$A = 100.00\ mm^2$ $\sigma = 3.14\ mm^2$ $L{=}D = 14.22\ mm$	$A = 58.06\ mm^2$ $\sigma = 1.02\ mm^2$ $L{=}D = 9.65\ mm$

Table 4. Friction Characteristics for Robotic Finger Pads

Pad Type	Effective Coefficient of Friction			Power Law Coefficients	
	1 N	***12.5 N***	***25 N***	*Static*	*Kinetic*
Cube 0°	$\mu_S = 6.10$ $\mu_K = 2.50$	$\mu_S = 1.71$ $\mu_K = 1.49$	$\mu_S = 1.17$ $\mu_K = 1.09$	$a = 6.159$ $n = 0.462$	$a = 2.534$ $n = 0.756$
Cube 45°	$\mu_S = 3.87$ $\mu_K = 1.90$	$\mu_S = 0.78$ $\mu_K = 0.70$	$\mu_S = 0.62$ $\mu_K = 0.58$	$a = 3.794$ $n = 0.361$	$a = 1.931$ $n = 0.361$
Cube 90°	$\mu_S = 1.67$ $\mu_K = 1.04$	$\mu_S = 0.49$ $\mu_K = 0.43$	$\mu_S = 0.33$ $\mu_K = 0.30$	$a = 1.688$ $n = 0.534$	$a = 1.056$ $n = 0.634$
Sphere 0°	$\mu_S = 2.99$ $\mu_K = 1.99$	$\mu_S = 1.11$ $\mu_K = 0.97$	$\mu_S = 0.85$ $\mu_K = 0.82$	$a = 2.994$ $n = 0.594$	$a = 2.039$ $n = 0.722$
Sphere 45°	$\mu_S = 1.56$ $\mu_K = 1.03$	$\mu_S = 0.58$ $\mu_K = 0.51$	$\mu_S = 0.43$ $\mu_K = 0.41$	$a = 1.635$ $n = 0.615$	$a = 1.045$ $n = 0.711$
Sphere 90°	$\mu_S = 1.16$ $\mu_K = 0.82$	$\mu_S = 0.45$ $\mu_K = 0.40$	$\mu_S = 0.32$ $\mu_K = 0.30$	$a = 1.163$ $n = 0.627$	$a = 0.789$ $n = 0.694$
Cyl. T. 0°	$\mu_S = 2.72$ $\mu_K = 1.71$	$\mu_S = 1.11$ $\mu_K = 1.00$	$\mu_S = 0.80$ $\mu_K = 0.75$	$a = 2.933$ $n = 0.681$	$a = 1.763$ $n = 0.760$
Cyl. T. 45°	$\mu_S = 1.90$ $\mu_K = 1.29$	$\mu_S = 0.64$ $\mu_K = 0.58$	$\mu_S = 0.44$ $\mu_K = 0.42$	$a = 1.929$ $n = 0.563$	$a = 1.270$ $n = 0.663$
Cyl. T. 90°	$\mu_S = 1.42$ $\mu_K = 0.90$	$\mu_S = 0.44$ $\mu_K = 0.38$	$\mu_S = 0.31$ $\mu_K = 0.29$	$a = 1.412$ $n = 0.529$	$a = 0.887$ $n = 0.642$
Cyl. A 0°	$\mu_S = 3.17$ $\mu_K = 1.71$	$\mu_S = 1.12$ $\mu_K = 1.03$	$\mu_S = 0.83$ $\mu_K = 0.80$	$a = 3.209$ $n = 0.593$	$a = 1.720$ $n = 0.783$
Cyl. A 45°	$\mu_S = 1.52$ $\mu_K = 0.99$	$\mu_S = 0.50$ $\mu_K = 0.45$	$\mu_S = 0.37$ $\mu_K = 0.34$	$a = 1.545$ $n = 0.568$	$a = 0.983$ $n = 0.693$
Cyl. A 90°	$\mu_S = 1.30$ $\mu_K = 0.72$	$\mu_S = 0.36$ $\mu_K = 0.31$	$\mu_S = 0.26$ $\mu_K = 0.24$	$a = 1.283$ $n = 0.466$	$a = 0.719$ $n = 0.664$

process such as air bubbles and slight variations in thickness. The final finger pads largest linear

dimensions (LLD) were recorded in the horizontal orientation (large), diagonal orientation (medium) and vertical orientation (small) in Table 3. To produce a given contact area, the sphere required the largest linear dimension followed by the cylinder then the square which required the smallest linear dimension. The spherical pad was so much larger than the other pads for a given contact area that in order to produce the contact area of the human index finger at 0° (~25mm LLD) under 12.5 N of loading the sphere would have to have five times the LLD whereas the cube would only require two thirds the LLD. These linear dimension relationships agree with current hertzian theory seen in [8] given the L=D assumption for our cylinder geometry.

The effective coefficient of friction for the human index finger was recorded in different orientations under different loading magnitudes. We found that at lower loads the coefficient of friction differed visibly based on orientation with the coefficient of friction increasing with surface area. For the lowest load of 1N, the horizontal orientation had a coefficient of friction of $\mu_{HI\_0^\circ}$ = 1.437, the diagonal orientation with $\mu_{HI\_45^\circ}$ = 1.212 and the vertical orientation with $\mu_{HI\_90^\circ}$ = 0.922. At the higher normal forces we observed that orientation and contact area had less of an effect on the coefficient of friction at 12.5N ($\mu_{HI\_0^\circ}$ = 0.494, $\mu_{HI\_45^\circ}$ = 0.473, $\mu_{HI\_90^\circ}$ = 0.429) and at 25N ($\mu_{HI\_0^\circ}$ = 0.300, $\mu_{HI\_45^\circ}$ = 0.332, $\mu_{HI\_90^\circ}$ = 0.289). The highest average deviation across normal force levels was recorded for the diagonal orientation and the lowest average deviation for the vertical orientation. We found that the human index finger tested using the ASTM D1894 standard followed a similar power law to that recorded in a meta study [92] which averaged the coefficient of friction of the human finger under varying loading conditions, orientations, surface moisture and surface materials (Fig. 5).

The artificial finger pads displayed rather different power law relationships between the applied normal load and coefficients of friction. The cubic contact geometry observed the highest

coefficient of friction at a low load (1N) as indicated by *a* in Table 4. The spherical and cylindrical transverse observed a similar coefficient of friction with axial sliding producing a slightly higher coefficient at low loads. This indicates that there could be a friction benefit when sliding axially versus transverse with a cylindrical finger pad. The power law coefficient *n* was formed such that as the load increased the coefficients of friction monotonically decreased in a non-linear fashion until converged to similar coefficients at higher loads. The only outliers were the 0° (large) and 45° (medium) cubic finger pads that displayed slightly elevated coefficients at the higher loads. This indicates that a cubic geometry and square contact area may be favorable to generate a higher coefficient of friction under most grasping loads for a flat surface. We observed smaller variance in the artificial finger pad coefficient variance than in the human finger coefficients which we believe is due to slight inconsistencies while loading and positioning the finger and finger pad moisture.

When measuring the differences between static and kinetic coefficients, the cubic grip pad had the largest difference for $\mu_{K\_Cube\_0^\circ}$ = 2.491 or only 41% of the static coefficient at the lowest load. This was consistent for all the artificial finger pads that recorded larger differences between the static and kinetic coefficients in the lower normal force range. Conversely, for higher normal forces we observed smaller differences in static and kinetic coefficients for all finger pads. On average, the kinetic coefficient of friction was 60.4% static for 1N and 93.5% static for 25N loading across all geometries. The artificial finger pad with the smallest nominal difference between static and kinetic coefficients of friction was the sphere with 83% and the primitive with the largest nominal difference was the cube with 76%. When the static and kinetic coefficients are similar it is difficult to determine whether or not the finger is frictionally sliding, frictionally sticking or rapidly transitioning between the two [91]. This required us to complete more tests at

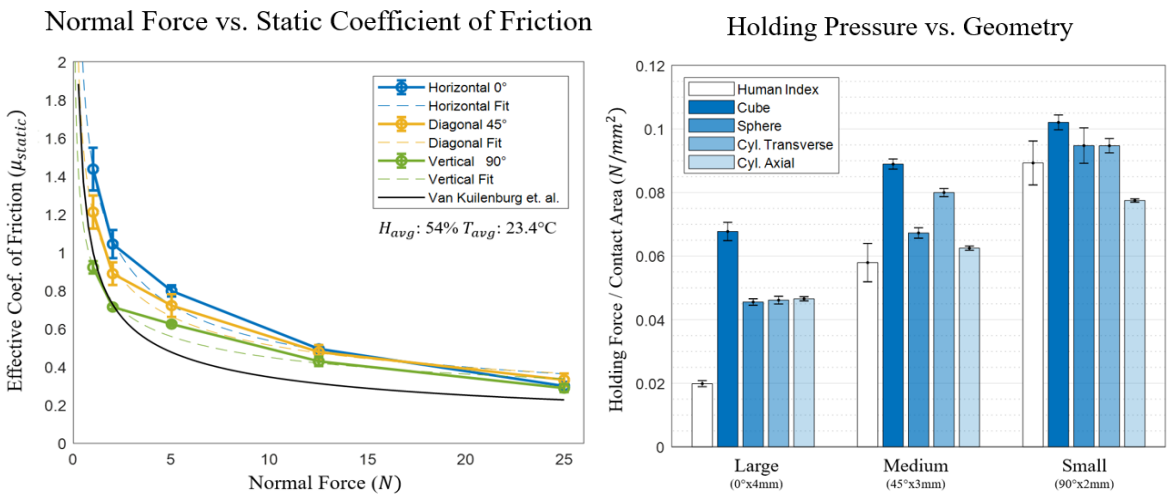

Figure 19. (Left) Study validation displaying the inverse power law relationship between normal force and coefficient of friction seen in a meta study and with our testing apparatus. (Right) The variance in holding pressure for the human finger pad and the three sizes of artificial fingerpads.

the higher loads to find areas where we could observe stable sliding. Although we observed minimal variance in finger pad coefficient measurement, we believe the higher nominal variance in kinetic coefficients over static occurred from difficulties in determining stable sliding.

The effective "holding pressure" was measured as the holding force divided by the contact area and was larger for the smaller finger pads for each given geometry (Fig. 6). The effective holding pressure of the smallest finger pads and index in the vertical orientation under this loading was similar, measured at approximately 0.090 $\mathrm{N/mm^2}$. For the largest contact area finger pads, the Cubic finger pads had the highest holding pressure, measured at 0.068 $\mathrm{N/mm^2}$, the spherical and cylindrical finger pads were in the middle, measured at approximately 0.046 $\mathrm{N/mm^2}$, and the human finger horizontal orientation had the lowest, measured at 0.020 $\mathrm{N/mm^2}$. Holding forces were measured to determine the relative holding force, at which the object shears from the hand, of the finger pads for use in a robotic gripper. Variations of this holding force with area, benefits of higher and lower coefficients of friction and practical design insight using these experimental parameters will be discussed in the next section.

4.6 Comparison and Key Takeaways of Finger Pad Geometries

We set forth to evaluate simple artificial primitive finger pads made of silicone rubber by varying applied loading, contact area and contact geometry. We defined an effective single contact as one that would produce that largest coefficient of friction and holding pressure between the hand-object system. A larger static coefficient of friction correlates to a larger frictional or holding force before slip occurs for a generic contact assuming minimal variation in adhesive forces between the finger and object [78]. We observed that the cube had the highest coefficient of friction for all three orientations. We expect our power law extrapolation to hold for higher forces until the elastic material yields, however, at forces lower than 1N we would expect this trend to round off as the cylinder and sphere converge to a line or point contact. This inverse power law relationship indicates that coefficient of friction is not constant during grasping, especially in the low force ranges as the object is being acquired. The relationships between normal load and surface traction presented can bolster models for the motion planning and manipulation communities, that are presented tasks that require repetitive grasping or grasps with varying force.

At 12.5N loading force, where the pads have almost identical surface areas, we observed that all the robotic primitives monotonically increased in holding force with an increase in surface area. The human finger had only a small increase in holding force with surface area with 5.4N for the vertical orientation and 6.2N for the horizontal orientation. The largest increase was for the cubical finger pads with 6.2N holding force in the vertical orientation and 21.4N of holding force in the horizontal orientation. Higher holding force for a given loading force is favorable in robotic grasping tasks because it requires less electromechanical power for an equivalent grasp. Along with maximizing holding force for a given applied load, another important metric to designers is to maximize the holding force relative to the finger pad size. Having excessively large finger pads

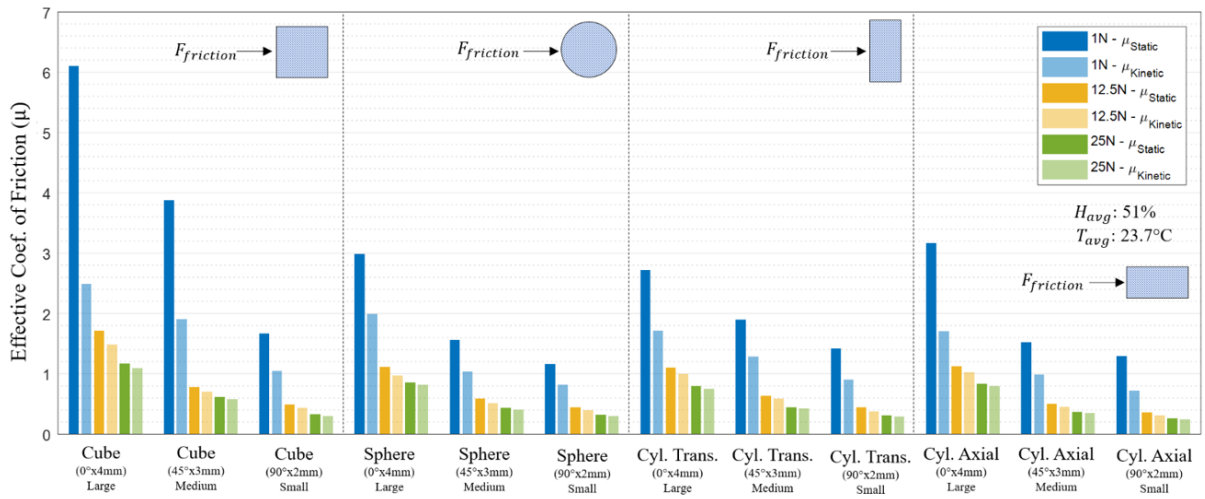

Figure 20. The full distribution of static and kinetic coefficients for each of the three evaluated geometries. The results are first segmented by the equivalent contact area and then subdivided by the applied force.

affects the weight, packaging and maximum object size that can be grasped for a given kinematic architecture. We defined this aspect "packaging" and evaluated it by normalizing the frictional holding force of each pad by its largest linear dimension, providing a ratio between the compactness and grasping effectiveness of the finger pad. This analysis further favored the cubic grip pads that were relatively compact with high coefficients of friction and disfavored the larger spherical pads. When evaluating the "packaging" of each of the three sizes for the geometric primitives, smaller grip pads outperformed larger pads for the spherical and cylindrical pads while the cubic pads remained fairly similar across orientations. Due to the diminishing returns, smaller grip pads could be optimal for grasping conditions that are compact and higher frictional forces are not required. Relevant applications include small surgical grippers, precision grippers, fingertips, hands that require multiple points of contact and caging grippers.

All three finger pads were deemed more effective for robotic grasping applications over that of the human finger in this test setup. We believe this was an artifact of the surface moisture, human finger ridges and the propensity to resist injury. As an additional analysis, we wanted to compare

the required normal force the artificial pad's gripper would have to maintain to exert a similar frictional force to the human finger. The only grip pad configuration that was unable to equate to the human finger pad in our test setup was the smallest surface area cylinder in the axial orientation under the 12.5N and 25N loadings in which the value was comparable. The cube performed the best only requiring 1.53N of loading force to output the same frictional force of the human finger with 25N loading. The largest sphere and cylinder also performed well, requiring from two to four times less normal force to provide the same frictional force as the human finger. This implies that for smooth dry surfaces grip pads are more efficient than the human finger for grasping.

4.7 Design Guidelines for Artificial Fingerpads

In examining the results, we can see several performance advantages from the primitive geometries that could be useful for engineers wanting to design simple and effective robotic finger pads. First, the cubic finger pad observed favorable frictional, shear and holding force performance at low forces and we believe this is due to the finger pad's relatively even distribution of pressure spawning from matching finger pad and surface geometry. Being able to produce a high holding force at a low load is critical for grasping applications so that the object does not reconfigure or slip as it is being acquired. Next, as the geometry of the finger pad moves further from that of the surface, the pressure becomes more concentrated towards the areas of initial contact and therefore slip initiates on the lower pressure areas. For the simple geometries studied here, the pressure concentration relates to the nature of the contact in the un-deformed state or in a very low force state: a surface contact for the cube, a line contact for the cylinder, or a point contact for the sphere. The closer the finger pad geometry matches the geometry of the surface, the more equal the pressure distribution and the better the frictional performance. This infers that flat finger pads will perform best on flat surfaces, given that they are closely aligned in orientation, and curved pads

on curved surfaces with very similar curvature. In summary, when designing finger pads, one should not only match curvature but also avoid variations in thickness of the pad where low pressure areas may develop when in contact with an object. We foresee a combination of curvature and thickness variation as an ideal solution to developing a simple grip pad for a given application. In future research, we would like to evaluate the performance of simple finger pads under more complex loading conditions and object geometries.

Our previous analysis focused on maximizing the frictional properties of a single contact on a flat surface, however, most practical robotic grippers are far more complex. Applying this idea to practical hands and grasping scenarios, flat finger pads are generally only going to align well to flat surfaces in planar graspers, especially parallel jaw grippers. Most other hand-object configurations that rely on several contacts will produce several line contacts or point contacts. For these scenarios, which represent the vast majority of cases for prosthesis, it is therefore best practice to attempt to increase the radius of the finger pad at the regions of expected contact to be as large as is reasonable, assuming the contacted surface is locally convex. If contact happens on a sharp edge (e.g. the edge of a polyhedron or the leading edges of a cylinder) a near zero-radius contact region will form producing unfavorable holding force and frictional properties. Thus, we recommend that finger pads should be “rounded off” with the largest reasonable radius for their application to mitigate unfavorable contact locations at the pad limits. We recommend this for prosthesis and other multi-finger robotic grasping applications where object uncertainty can force contact in unfavorable locations. If significant uncertainty is expected, one could take this concept to the limits by creating a reasonably sized spherical surface that will provide minimal frictional benefits, however, ensure the object will contact the finger pad away from boundaries and in a predictable manner.

There are some applications where both being able to grasp and then manipulate an object are desired, either with multiple fingers or a single finger and the support plane. This typically involves some amount of pivoting of the object with respect to the initial contact location and surfaces. In these cases, some amount of rolling is typically required and if the contact location is a sharp point contact (of very small or zero radius) the rolling of the object will likely not produce significant contact location changes. This will allow for more free motion because the structure of the fingertip will provide very few constraints to rotation. Thus, a sphere, although slightly underperforming in frictional characteristics, is a favorable contact geometry when designing for manipulation because it allows for more mobility of the object at the contact and a somewhat reliable knowledge of the contact center of rotation for post contact planning. An additional possibility to solving both surface alignment and manipulation issues is to have a simple passively reorienting finger pad that self-aligns with local geometry, allowing slip during manipulation and maximizing contact area passively post-manipulation [84]. In the future, we want to further investigate the combination simple finger pad geometries (cube, cylinder, sphere) and smart finger design to maximize the ability for a robotic finger to not only grasp but manipulate an object.

4.8 Conclusions

In this chapter, we experimentally established the tradeoffs between primitive geometries when used as artificial robotic finger pads. Based on the three primary grasps of our prosthetic hand (power, tripod, lateral), we decided to adjust the finger pads accordingly to accompany each grasp type. The proximal finger pads were flattened and thickened to provide additional contact area for larger objects at high grasp forces. The distal fingertip was increased in size, slightly flattened at the distal tip and extended to now provide contact all the way up to the fingernail. Although this significantly increases the difficulty when creating the distal finger pad molds, we found that this

extra coverage helped significantly when grasping small rigid objects. Last, the index lateral grip pad was extended and the thumb position was more accurately aligned to better secure objects in lateral grasp.

V. FABRICATING COMPOSITE PROSTHESIS

A main component to the high rejection rates for upper limb prosthesis is that they are nominally too heavy to comfortably wear throughout the day. Muscle fatigue from wearing the device can lead to other issues in the amputees proprioceptive and grasping abilities. The idea of 3D printed prosthetics components promises affordable, customizable devices, but these systems currently have major shortcomings in durability and function. In this chapter, we propose a fabrication method for custom composite prostheses utilizing additive manufacturing, allowing for customizability, as well the durability of professional prosthetics. The manufacturing process is completed using 3D printed molds in a multi-stage molding system, which creates a custom finger or palm with a lightweight epoxy foam core, a durable composite outer shell, and soft urethane gripping surfaces. The composite material was compared to 3D printed and aluminum materials using a three-point bending test to compare stiffness, as well as gravimetric measurements to compare weight. The composite finger demonstrates the largest stiffness with the lowest weight compared to other tested fingers, as well as having customizability and lower cost, proving to potentially be a substantial benefit to the development of upper-limb prostheses.

5.1 Motivation for Composite Manufacturing in Prosthetics

Additive manufacturing, or 3D printing, has become a widely accessible and cost-effective method of prototyping due to its ability to quickly create custom modeled parts out of inexpensive thermoplastics and resins. A common method of additive manufacturing, fused deposition modeling (FDM), uses an extruder head that lays down a filament in discretized layers to create a

final part. The thermoplastic filament, acrylonitrile butadiene styrene (ABS), is commonly used in this process due to its high impact resistance, toughness, and light weight. This has made 3D printed ABS a prevalent choice for open-source prosthesis hands with products like the Cyborg-Beast or the Raptor Hand [101-102], which are intended to allow for a low-cost prosthesis that is also customizable. Although 3D printing has made custom prosthetic designs accessible to the public, it lacks the durability and strength to make these devices practical, which then have many shortcomings compared to commercially manufactured terminal devices [103]. We propose a new method that bridges the gap between highly customizable open-source 3D printed prosthetic hands and the professional prosthetic hand market. This process originated with the Hybrid Deposition Manufacturing method proposed in [104], but has been modified to allow for the use of composite materials such as carbon-fiber. This method results in finger/hand components that are lightweight, durable, and include gripping surfaces like those used in the professional prosthetics market. The goal of this method is to improve and refine future terminal device designs to create a cost-effective, customizable, durable, and lightweight prosthetic hand.

5.2 Prosthesis Manufacturing Methods

The current fabrication process for open-source hardware generally includes modeling the solid part geometry in a computer aided design package (CAD) and then 3D printing it in ABS or polylactic acid (PLA) plastic [102] using the most common FDM printing technique. The printing software allows the users to determine the infill amount, therefore allowing the part to be printed partially hollow to save material and reduce weight at the expense of a potentially weaker component. A significant advantage of FDM printing of prostheses is that it allows users to quickly customize the shape and size of components to fit an individual patient. For open source hands

Figure 21. Examples of prosthetic fingers from the Bebionic Hand (aluminum), the Cyborg Beast Hand (ABS plastic) and the MyoAdapt hand (composite).

like the Cyborg Beast Hand, these components are made available online for anyone to print or scale as needed, which is useful, for instance, when children quickly grow out of a prosthesis [102].

One current limitation to FDM printing is the limted number of materials available. When part strength and stiffness is a requirement, most 3D printed parts and materials fall short since they are mostly limited to thermoplastics. Attempts have been made to reinforce 3D printed parts to make them more durable; however, this only provides marginal improvements [105-107]. New printing methods are also being implemented that allow for the 3D printing of composite structures with Kevlar and Carbon Fiber [108]. Although this method may prove beneficial in the future, its processes are currently still under development.

The current fabrication process for commercially available prosthetic hands generally includes a combination of injection molded plastic and cast or machined metal components. The materials include glass-filled Nylon, titanium, and aluminum [103,109]. Urethane rubber grip pads are injection molded and adhered to the surface of the finger tips and palms to increase the grip of the

smooth metal or plastic. All joints (usually pin joints) are assembled, and connected to the aluminum or steel frame and then attached to the actuation system.

The major limitation of this method is that machined titanium or aluminum components are expensive, and the tooling required for Nylon injection molded components limits the customizability of the design. It is likely that only a small number of sizes of the hands are available due the large tooling cost associated with another size option and customizable features specific to each patient are not possible. For example, the i-limb Ultra myoelectric prosthetic hand is only available in sizes medium and small [110].

5.3 Molding and Component Fabrication Pipeline

In this section, we will walk through our process of creating custom composite components utilizing 3D printing to produce professional grade prosthetic component while maintaining the customizability for individual patients. This method is appropriate for prosthetic hand fabrication since the personal nature of prosthetic hands requires frequent design changes and customization for each patient. The method we have developed is roughly based on the hybrid deposition manufacturing (HDM) techniques described in [104]. We have modified the technique to include the use of composite carbon-fiber shells for added strength and rigidity.

The influence for the material composition of our composite prosthetic hand is derived from the manufacturing of ultra-lightweight structural components used in Formula 1 racecars and aerospace components. Here composite materials with various core structures are used to create materials with the highest possible strength to weight ratios. Typical carbon-fiber techniques are rarely used on components as small as prosthetic hands or fingers due to the part contour complexity. Our method of fabrication has overcome many of the previous limitations and allowed

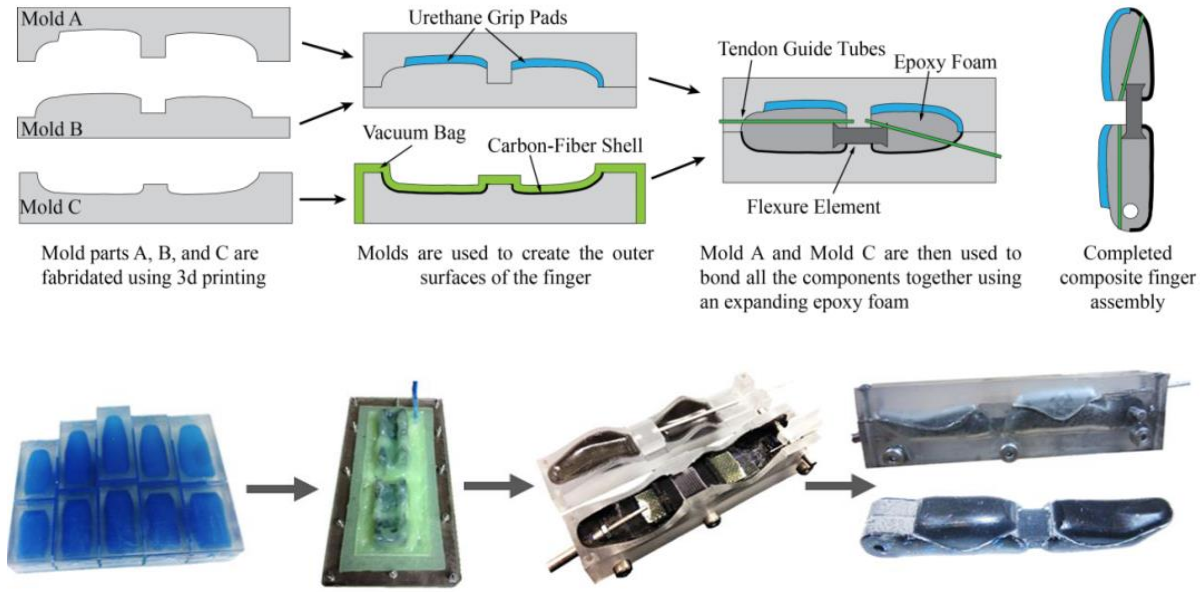

Figure 22. Illustration of the multi-step manufacturing process for custom composite prosthetic components.

us to fabricate prosthetic fingers with the same materials and techniques used in high grade aerospace components.

The desired prosthetic finger composition consists of three main layers; the carbon-fiber structural shell located on the back and sides of the finger, a lightweight foam filler material that serves to bond the internal components together, and a soft urethane grip surface that mates seamlessly with the shape of the structural shell. Each of these individual elements, as well as the fully assembled finger, can be fabricated through the use of three custom molds. Mold A, consists of the geometry of the front of the finger up to the parting line between the grip surface and the carbon-fiber structural shell. Mold B mates together with mold A and forms the inside surface of the urethane grip pad. Mold C, mates together with mold A but forms the back outer surface of the finger. An illustration of the three molds is shown in Fig. 2.

Our process uses multi-part molds created from the customized finger geometry. First, the desired finger geometry is created in CAD software. The parameters such as length, thickness, and

even joint stiffness can be directly altered for each patient. A set of small molds are then automatically created from the desired finger geometry.

The mold is then split along the gripping surface lines and a parting line analysis is then done to minimize undercuts. Significant undercuts can result in die lock, preventing the removal of the solid part from the mold. If necessary, the mold can be split lengthwise and printed in two parts with bolting features that can be removed if die lock occurs. The molds are then printed on an Objet printer using VeroClear material [111]. Alternatively, the molds can be printed in ABS using a standard FDM printer although the authors have been able to achieve better mold surface finish using an Objet, polyjet style printer. The actual material strength of the mold is not important However; thin walls can lead to potential deformations in the finger geometry. This results from the internal pressure build-up of the expanding foam during the final in-mold assembly step.

After the three molds have been printed, they are coated with a wax based or polyvinyl alcohol (PVA) mold release. Molds A and B are brought together to create the geometry of the grip pads on the anterior side of the fingers. To prevent grip pad defects, it is important for the urethane material to be placed in a vacuum chamber before being placed in the mold to degas the resin. In the case inconsistencies persist in the final part, it is recommended to incorporate risers and air vents into the Part B mold to release excess trapped gases. After the urethane material has cured, Part B is removed and excess flashing or riser material is trimmed from the grip pads.

Immediately after the grip pads are cast, the carbon fiber half of the mold, denoted as Mold C in Fig. 2 on page two, should be prepped with a PVA mold release. Two layers of 200 gsm 3k 2x2 twill weave carbon-fiber dry cloth is placed in the mold and trimmed to the appropriate size. To improve overall strength, the orientation of the carbon weave should be offset by 45 degrees between the layers. Epoxy resin is then flooded over the dry carbon-fibers. A custom silicon

vacuum bag, as seen in Fig. 3, is then placed over the wet carbon to remove excess resin and apply pressure to the inside surface of the mold. Once the epoxy resin has fully cured, the vacuum bag and absorption layers are removed and the carbon shell is trimmed to the edges of the mold.

Next, all the previous components are integrated into one final part using mold Parts A and C and additional inserts. Before closing the mold all the necessary inserts and joints are placed in the correct locations. Epoxy expanding foam (Sicomin PB400 [112]) is poured in the middle of the two halves to join the shell and the grip pad to make a finger. The expanding epoxy foam core acts as a lightweight internal structure and a glue to bond all the components together. Please refer to Fig. 2 for details of the full finger assembly mold process. Carefully painted PVA mold release was used to prevent the expanding foam from bonding to selected surfaces such as the center of the flexible urethane finger joint. It is acceptable to allow some of the foam to overflow in this process to reduce pressure and purge additional air. After the recommended amount of curing time the finger can be removed and lightly sanded to remove any flashing from the parting line.

This finger is durable with its carbon fiber shell but also very light with its foam core which bonds joint members and other additional inserts into the finger. The resulting fingers, seen in Fig. 4, have grip pads to improve grasping capabilities, flexure joints to promote out of plane bending, and outer carbon shells for added strength and durability. Different inserts such as a pin joint, tendon tensioning mechanisms, and PEEK tubing to reduce tendon friction are used in these finger examples. The palm structure of the hand is fabricated in a similar process.

5.4 Experimental Structural Testing

Three different measures were used to evaluate the performance of our manufacturing method as well as other manufacturing methods commonly used in prosthetic hands. These methods included a strength analysis, weight analysis, and a discussion of the advantages and disadvantage

Table 5. Three Point Bending Test Results

Specimen	Weight (g)	Density (g/cm^3)	Yield Stress (MPa)	Max Strength / Weight Ratio (GPa*cm^3/g)	Max Stiffness / Weight Ratio (GPa*cm^3/g)
Sparse Printed ABS	17.5	0.71	26.3	0.037	2.03
Solid Printed ABS	23.3	0.95	43.5	0.046	2.08
PB 400 Epoxy Foam	9.3	0.39	6.3	0.016	1.33
Two Layer 2x2 Carbon Twill - PB 400 EEF	11.3	0.46	56.4*	0.123	16.51
6061 Aluminum*	65.2	2.70	276	0.102	25.52

*Yeild stress was equal to fracture stress, **Calculated based on [14]

of the composite molding process. The core materials we will test include 3D printed ABS plastic in both solid and sparse raster filled, epoxy expanding foam, and carbon-fiber composite structures. For reference, we will also include information on the strength of aluminum 6061 since it is also a common material used in commercial prosthetic hands.

To evaluate the relative strength of each manufacturing method, rectangular bar specimens were tested using the ASTM D790 flexural three-point bending test [113]. For each manufacturing method, five specimens were tested. The specimens were rectangular blocks measuring 8.3x19.1x152.4 mm and were sized according to the standard. When testing 3D printed ABS plastic, the layer direction was noted to evaluate the effect of different printing orientations. In a horizontal test the specimen width was parallel with the print tray and extruder layer orientation, while in vertical tests the sample width was oriented vertically on the print tray. For the carbon-fiber shell test specimens, the carbon-fiber was placed on the top and bottom of the foam. No carbon-fiber was placed on the sides of the specimen to better replicate the open shell of the fingers in from the proposed manufacturing method.

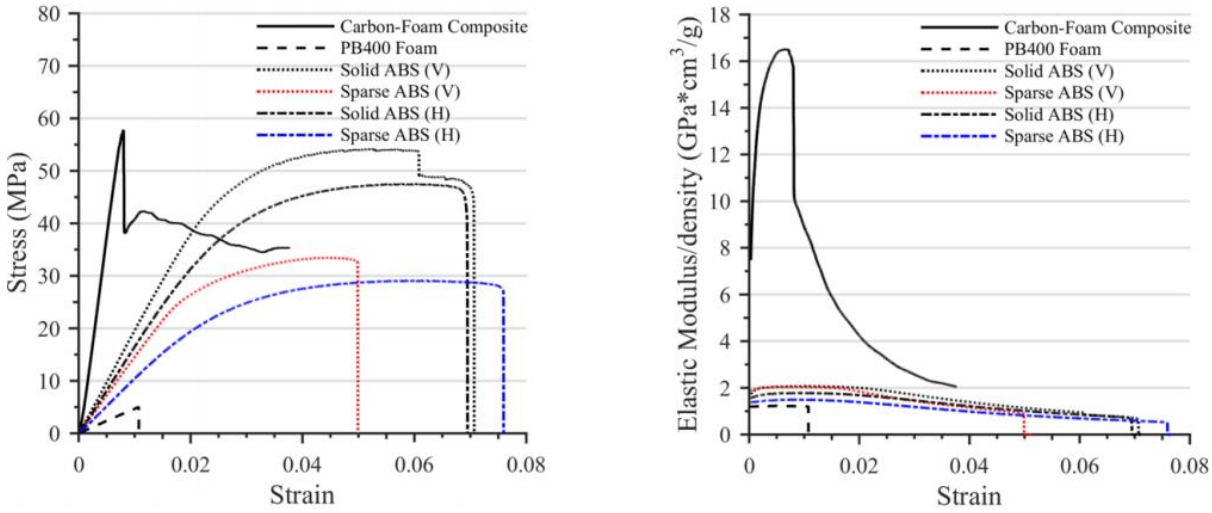

Figure 23. Two graphs of the structural evaluation of solid ABS, sparse ABS, Foam and carbon composite beams in three point bending. (Left) The effective stiffness of the evaluated materials. (Right) The equivalent stiffness per unit mass of the materials.

In order to compare the different materials, each specimen's weight and density were recorded; the stress during the three point bending test was also calculated. A stiffness to weight ratio was then determined for each specimen in order to evaluate the optimal material, shown in Table 1. The stress-strain relationship for each specimen is shown in Fig 4. The stiffness to weight ratio is plotted versus strain as shown in Fig 5. It is seen that the epoxy expanding foam has the lowest average weight of 9.25g, but also has the lowest stiffness to weight ratio. The carbon-fiber with epoxy expanding foam specimen has the next lowest average weight of 11.3g, and also has a significant stiffness to weight ratio of 1.65 GPa*cm^3/g. This ratio demonstrates the added strength and durability of using carbon fiber, with the low weight of the epoxy expanding foam. The calculated values from 6061 aluminum were based on known material properties found in [114].

To evaluate the weight of the fingers, we fabricated equivalent models of a 50th percentile female sized middle finger. The proximal and distal links of each finger were connected with a urethane flexure (Smooth-On PMC [115]) and a two layer grip surface (Smooth-On Vytaflex [116]) was

added to each finger. For the epoxy foam core fingers, the grip pads and flexures were molded and embedded into the foam, while, for the 3D printed parts, grip pads and flexures were bonded on using adhesive. The quantity of adhesive was measured out to be 0.3 additional grams for the ABS printed fingers shown in Table 2. The finger weight was estimated for the machined aluminum finger using the total volume of the finger CAD model and the density of aluminum [114]. The weight of each finger fabricated with each respective material is shown in Table 2. The expanding epoxy foam with and without carbon fiber maintain the lowest weight, with a weight of 8.6 and 8.5 grams respectively. The aluminum is almost four times the weight of the foam fingers, having a weight of 31.6g, however, it is unlikely that aluminum fingers would be fabricated to be solid aluminum.

One advantage of additive manufacturing is the ease of production. A custom model can go straight from design to manufacturing in a matter of hours. Although additional time is required, the durability of a solid printed finger is similar to that of the composite though significantly heavier. Errors associated with using additive manufacturing to create prosthesis fingers include print errors, adhesion loss, and print inconsistency. First, the type of printer used when creating prosthetic fingers has a sizable impact on the quality, strength, and resolution of the part. Printing errors on lower quality printers can lead to open contours and failed parts. Sometimes these errors occur in internal contours or support structure, and cannot be visible from the outside of the part. This can lead to stress concentrations in the finger. Another flaw with the 3D printed method is the loss of adhesion of the grip pads as well as the flexure joint. This could be alleviated with additional epoxy adhesive, however, the potential pulling out of a flexure could be a significant failure while attempting to maintain a grasp. We found the task of embedding a flexure in an

anthropomorphic finger difficult. Attempts to split the finger or have a removable insert and adhering the flexure in place caused severe lateral weakness in the fingers.

The main advantage of machined aluminum is the strength of the material. Complex 3D geometries are difficult to machine with CNC Mills and require multiple readjustments. For larger parts, complete tooling may become expensive and is limited in the ability to prototype or customize a variety of molds.

The main advantage to the carbon fingers was the durability of the finger with respect to weight. We saw that it was also relatively easy to manufacture as the carbon shell and grip pad could be made at the same time. Then, without removing from its respective molds, the two parts making up the outer layers could be sealed together with foam. The carbon shell presented additional advantages such as abrasive resistance as well as a clean surface finish that can be an issue with 3D printed parts and fingers made completely from expanding foams. Errors associated with foam fingers included internal voids and a soft outer surface that was easily damaged. First, a common flaw with intentionally porous expanding foams is that gas pockets or "voids" can form that are bigger than expected. As seen in Fig.8, these voids can cause severe weaknesses in the part or surface blemishes. The addition of a carbon fiber shell allows the finger to have a better durability, however, does not aid in preventing internal voids in the finger.

5.5 Viability of this Composite Manufacturing Process for Prosthesis

We found that our manufacturing method created a durable and lightweight prosthetic finger, properties that are very important for the area [117]. A full hand made out of carbon laminate using our proposed method could potentially be one half the weight of a 3D printed hand and one quarter the weight of a machined aluminum hand. For amputees the prosthetic hand is an extension of

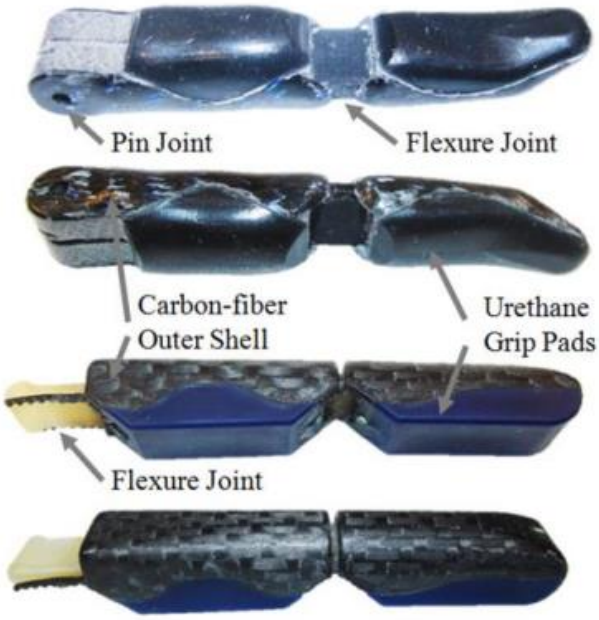

Figure 24. Example output of custom carbon composite underactuated prosthetic fingers made with this manufacturing pipeline. This includes a pin-flexure and flexure-flexure design with different geometries.

their body, reducing weight of the prosthetic can not only help prevent fatigue but can also aid grasping by allowing for easier and quicker movements.

The ability to work in parallel when curing the grip pad urethane and carbon fiber resin allows the process to be simplified to four steps; creating molds, casting urethanes and laying carbon fiber, creating foam core, and removing final finger from molds. The downtime associated with letting resins cure is shared during the production of the carbon fiber and gripping surfaces. This allows the manufacturer to create any necessary inserts for the mold and the finger, such as a urethane flexure joint, while the first two parts are curing. This efficiency is one of the advantages of our composite finger manufacturing process.

If weight, customizability, and cost were not important factors, a machined aluminum finger would be the primary option due its superior strength and durability. The use of composites in prosthetics fingers provides a significant stiffness to weight profile over that of aluminum and

solid ABS plastics. At low strains, we saw that the Grablab composite finger was almost 8 times stiffer than solid and sparse printed ABS plastic. A more durable finger for a given weight allows the user to have the same sturdiness with less fatigue or force required to maneuver the finger.

The current manufacturing process only allows us to produce individual fingers in parallel and would like to eventually extend the use of this method into the fabrication of a palm. As additive manufacturing becomes more available, we believe that this manufacturing method can reach out of prostheses into broader categories like custom lightweight robotics. Rapid prototyping with additive manufacturing allows the user to visualize the size and geometry of a part, however, a current downside of this is the user's inability to use that prototype for the actual application. As a prototyping technique, our manufacturing method can provide the fabricator with a useable and rapidly alterable prototype that can simulate the durability of the final product. The rapid manufacturing of molds to create composites can impact many industries where a durable lightweight replacement part is needed quickly or where access to heavy machinery or casting equipment is limited.

5.6 Conclusions

In this chapter, we presented a multi-step manufacturing technique for fabricating composite prostheses using molds created through additive manufacturing. This method combines the rapid prototyping capabilities of additive manufacturing techniques with the part strength and durability of the professional prosthetics market. Through a three point bending test, weight, and manufacturing analysis we determined that our composite fingers are a viable option for use in prosthetic hands. We created a full prosthetic hand using this manufacturing methods and have added a few methods (support material pockets, chopped fiber infill, and vacuum support structures) to help improve the process. In the next chapter we will present the final hand design,

which due to time constraints uses an abs/composite blend instead of this manufacturing method. However, we are excited to see its potential applications in the field of prostheses as well as other fields where custom lightweight durable parts are essential.

VI. Final Device Design

In this chapter, I will discuss the final design changes made to improve the single actuator prosthetic hand before testing. This will include changes to the finger geometry, transmission and locking mechanisms, and an automated method for transitioning between power and tripod grasp. This will also include considerations from the previous studies - including the optimized finger kinematics for precision grasp and improved artificial finger pads for both the proximal and distal links. These adjustments will be discussed and then compared to the initial prototype in the next chapter through benchtop and human subject testing.

6.1 Underactuated Hand Transmission Design

The concept of underactuation, where a mechanism has less actuators than degrees of freedom, has been leveraged in prosthetic hand designs to decrease control complexity and cost while still providing a compliant multiple finger grasp. Previous research has shown that underactuated hands can adapt to a variety of object sizes and geometry using either open-loop or simple close-looped control [8]. However, these devices are commonly only capable of a single grasp when compared to the multiple grasp types that are made easier in hands with several motors. Our goal was to be able to create a single actuator anthropomorphic hand with the several adaptable grasps seen in more complex multiple actuator hands. This hand, the Yale MyoAdapt hand, is capable of three grasp types including a power grasp, a tripod grasp and a lateral grasp. These three grasp types were chosen based on their higher frequency usage by amputees in everyday activities [18].

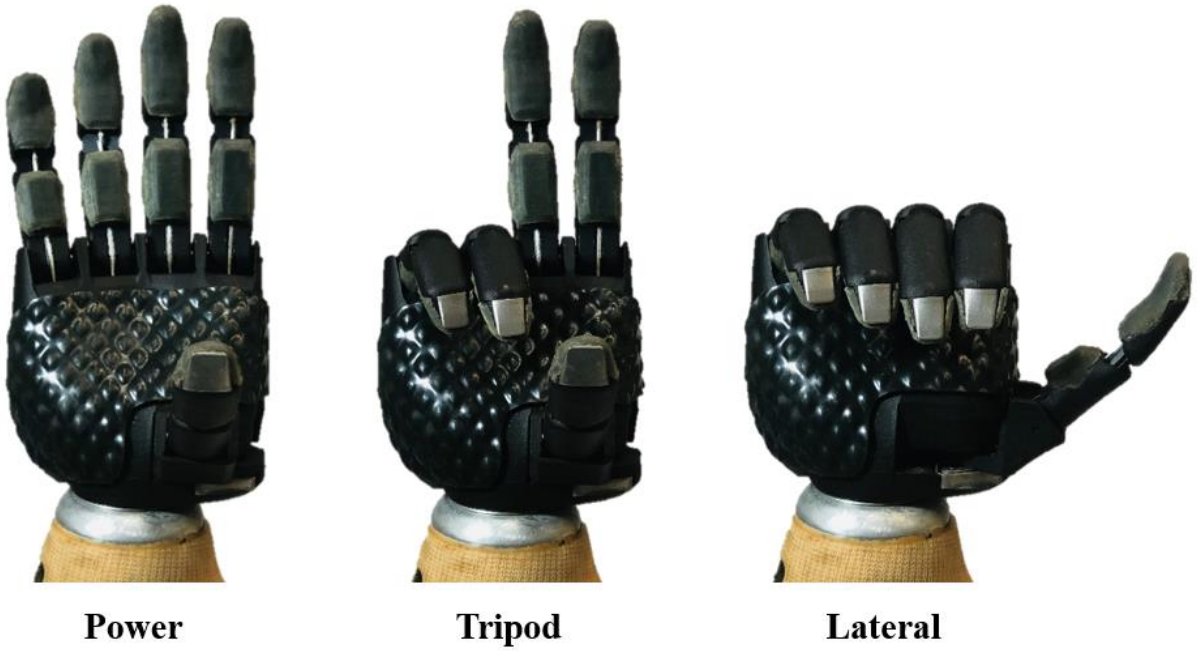

Figure 25. The three main grasp types of the MyoAdapt hand including a wide aperture power grasp, a three fingered precision grasp and a lateral grasp where the thumb opposes the lateral side of the index finger.

The MyoAdapt hand is considered underactuated because it has one degree of actuation (DoA) for its ten degrees of freedom (DoF). This active degree of actuation is from a single brushed DC motor (*Faulhaber 1524SR*) that is diagonally placed in the 50th percentile female sized palm chassis due to packaging constraints (fig 2.). We found this orientation was favorable for fitting larger higher torque motors within the palm. If the hand was to be scaled to 50th percentile male or larger we assume that a higher torque motor – with even better performance – could drive the hand in a similar orientation. The single motor drives five two-jointed fingers totaling to ten degrees of freedom. There is a single manual degree of freedom that allows the thumb to reposition and lock from forefinger opposition to lateral opposition. Last, there is another passive rotational degree of freedom made possible by the flexure spanning each fingers distal interphalangeal joint.

The single actuator is first attached to a planetary gear stage that drives a single worm gear pair. These two initial gear stages provide mechanical advantage through gear reduction. The worm

wheel also provides non-backdrivability to avoid excess power consumption from motor stall while grasping. The worm wheel drives an output shaft which has three main tendon pulley drives attached. The output shaft is keyed at different radii to precisely align the three output pulleys. The anterior palm pulley is slightly smaller and drives the thumb. A larger pulley in the posterior palm drives the forefingers through an underactuated finger coupling mechanism. This pulley is larger because the torque must be split between four fingers creating an asymmetrical rate of closing between the forefingers and thumb. This difference in pulley radius between the thumb and forefingers allows us to provide a more anthropomorphic grasp as well as create unique tripod and power grasp timings through the use of an internal locking mechanism. This locking mechanism is driven by the third output shaft pulley in the middle of the palm and consists of two antagonist tendons that create the transition between power and precision grasp. We will discuss how this transition is automated in the next section.

The grasps are controlled through closed-loop feedback with a simple current sensor to identify when an object has been successfully grasped. If the current limit is not met, each grasp has a calculated excursion that is determined from a high resolution 2-channel magnetic encoder attached to the back of the DC motor. We consider two encoder positions for each grasp, the grasp start (L_{Tendon_Start}) and grasp end (L_{Tendon_End}). These values vary depending on the grasp mode that is currently selected. The power grasp spans the full range of actuator excursion while the precision and lateral grasps both have around half that excursion. This allows for a slower wider aperture power grasp and quick smaller aperture precision and lateral grasps. The varying motor position for each grasp is created through the use of two active locking mechanisms which we will discuss in the next section.

6.2 Finger Coupling and Locking Mechanism

The forefingers are driven by a single differential mechanism that is coupled to the output shaft of the gearbox. This modified whiffletree mechanism has been coalesced to fit within the small size of the hand and provides differential motion between each of the three fingers from the single input tendon. All four fingers have a similar pulley radius and spring stiffnesses at the proximal and distal joints. This ensures that under no loading the forefingers have similar excursion and will close at the same rate. The exact kinematic specifications of these transmission ratios and spring stiffness are decided from an optimization study [19] that will be provided in the next section.

The coalesced whiffletree mechanism consists of three bars, one that attaches to the central output shaft tendon, and then two identical bars that attach to the index-middle pair and ring-pinky pair. Each tendon routing is countersunk and then epoxied to both protect and fasten the knot at the end. The whiffletree provides an adaptive grasp by allowing the two pairs to move independently of one another while allowing each pair to move independently through rotation of the distal bar. This provides a slight coupling between the fingers in each pair which we found to be beneficial during tripod grasping [17]. On the backplate of the main whiffletree backplate, there is a slot that constrains the distal bars to prevent misalignment of the output tendons. With this mechanism we can provide eight degrees of freedom – two for each finger – from a single tendon off of the output shaft. This includes additional adaptability while grasping at the distal flexure joints that have the ability to conform to objects out of the finger grasping plane. Our group has investigated using floating pulleys [20] to alleviate all forefinger motion coupling, however, we believe that this makes the hand significantly more difficult to fabricate with limited benefit especially in tripod grasp.

Along with the whiffletree there is a locking mechanism in the backplate that rotates to automatically switch between power and tripod grasp types. In power grasp, the thumb opposes

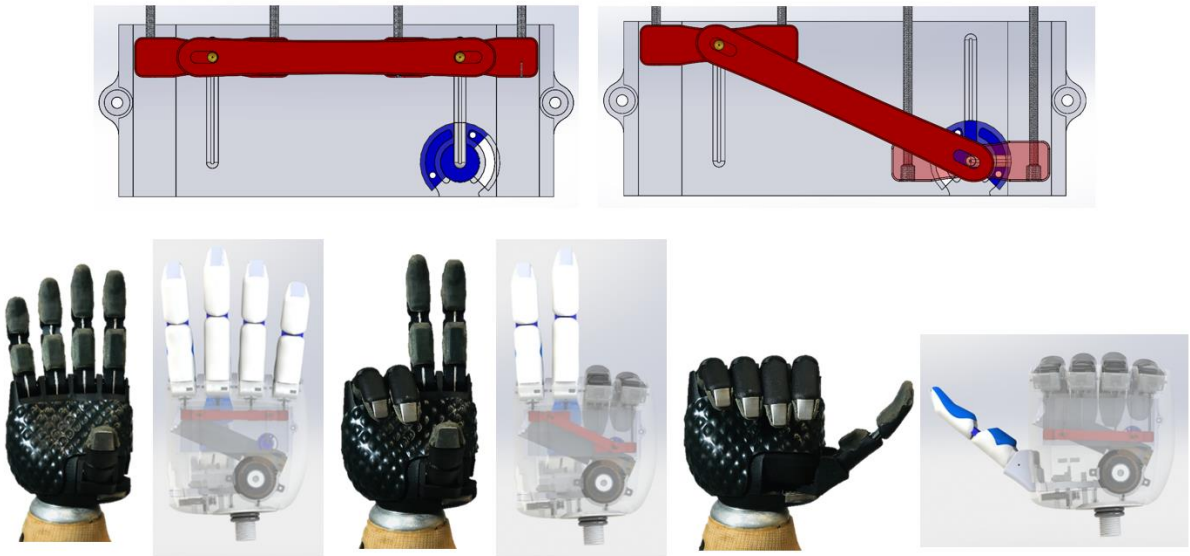

Figure 26. The whiffletree members pose when in power, tripod and lateral grasp. When in power grasp the whiffletree is free to move. When locked using the blue locking mechanism the hand is placed in tripod grasp and the index-middle pair is actuated like a lever arm. In lateral grasp the whiffletree is locked diverting the actuator power to the thumb.

the index-middle pair and each finger closes at a similar rate until an object is acquired or the grasp is completed. In tripod grasp, the ring-pinky pair of the whiffletree is locked closed by this mechanism, creating a new lever arm actuation method with only two degrees of freedom. The new actuation lever arm provides twice the closing rate with a lighter grasp force which is necessary for acquiring smaller or lighter objects. Additional slack is removed so that the grasp starts immediately when the grasping signal is passed. Locking and unlocking is automated through a rotating slotted cylinder that is driven by two antagonist tendons on the output shaft. When the output shaft closes the hand in power grasp, an additional quarter turn of the output shaft will drive the switching tendon, locking the ring-pinky member in place. Because this is a tendon, the ring-pinky will remain locked until it is released. The transition back to power grasp occurs when the hand is completely open in tripod grasp and the motor is run backwards past the initial datum. This drives a tendon resetting the slotted cylinder and releases the ring-pinky member to

open the hand into power grasp.

6.3 Thumb Positioning Mechanism Design

The hands third grasp is a lateral grasp, where the thumb is in opposition with the proximal link of the index finger. This grasp is selected through a manual rotation of the thumb when the hand is already in tripod grasp. This motion displaces a tendon connected to the index-middle whiffletree member with the thumb abductor locking the two fingers closed. In lateral grasp, the thumb aperture is slightly closed due and all force is now allocated to the thumb driving tendon on the output shaft. This allows for a strong small aperture grasp necessary for lateral grasp activities of daily living, including turning a key or holding a mug.

In a previous version [17], the tripod-to-lateral transition was also manual. The user had to press and hold a button to unlock and lock the finger into the power/tripod and lateral grasp locations. We found this was too complicated of a transition for bilateral amputees, requiring the amputee to both press and hold the selector button and then manually rotate the thumb. We found that a four-bar bistable mechanism is a simple and robust solution that can simplify this motion by eliminating the need for a selector button but still provide the required locking.

This four bar mechanism (Fig 3.) provides force through a spring that locks the thumb in the correct anatomical positions for power, tripod and lateral grasps. When designing a planar four bar linkage, there are many things to consider that will alter the coupler curve of the mechanism. First, we considered a planar quadrilateral linkage with four revolute joints (RRRR). Due to the sizing constraints, we required the thumb rotational axis to be small, making a crank-rocker architype ideal. To determine whether or not a planar four-bar linkage will act as a crank rocker, we must first take into account the Grashof Condition to determine if our input thumb motion (crank) will be constrained during the transition.

$$S + L \leq P + Q$$

Where S and L are the shortest and longest links in the mechanism and P and Q are the two middle length links. Once this is satisfied, we have ensured that the crank will be able to fully rotate in the required anthropomorphic range. We can then determine if the relative coupler motion using the below equations corresponding to Fig. 3 [21].

$$T_1 = r_1 + r_3 - r_2 - r_4$$

$$T_2 = r_1 + r_4 - r_2 - r_3$$

$$T_3 = r_3 + r_4 - r_1 - r_2$$

Where r_2 is the input link length, r_4 is the output link length, r_1 is the ground length and r_4 is the floating link length. When all three of these criteria are positive, we can assume our input thumb motion will operate as a crank with a full range of rotation and our output linkage coupler curve will operate as a rocker. The crank-rocker relationship was chosen over a crank-crank relationship because we would like this mechanism to be bistable. Bistability in a crank rocker system will allow us to use a single spring to apply force to lock the thumb in either position by manually sliding the thumb through the mechanisms singularity point. Bistability in crank-rocker systems with a single spring is ensured when the following equation is satisfied [118].

$$K_4(\theta_4 - \theta_{4i})\frac{d\theta_4}{d\theta_2} = 0$$

Where K_4 is the output linkage spring stiffness, θ_4 and θ_{4i} are the final and initial angle of the output link, and θ_2 is the angle of the input link. When this relationship is satisfied, we can solve the systems kinematics to select the starting angles and link lengths that make sense for our given packaging constraints. We solved this using a nonlinear optimization (MATLAB) framework given that we wanted the input crank to have $(\theta_2 - \theta_{2i}) = 90°$, r_2 = 0.5 inches and the point of

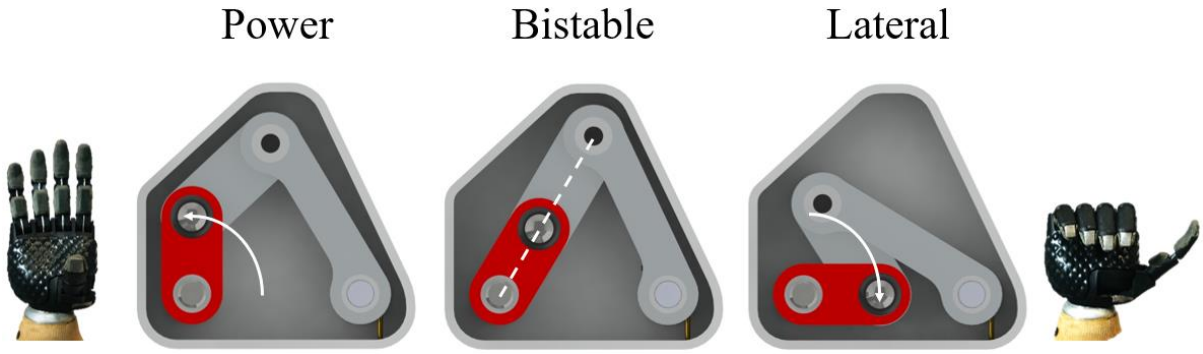

Figure 27. The three poses of the bistable locking mechanism designed to passively provide locking force for the thumb while in power and lateral grasp.

bistability to be when $\theta_2 = 45°$. With these constraints ensured the spring applies a similar amount of locking force in both thumb orientations. We then selected a spring stiffness that was as rigid as possible to ensure the thumb would remain against each hard stop but still allow the amputee to feasibly rotate the thumb through the singularity point.

6.4 Underactuated Hand Transmission Design

The palm and finger components are anthropomorphically sized to a 50th percentile female hand [22]. This includes accurate joint positions for the forefingers and thumb in relative elevation, positioning and abduction angle. Slight differences include a slightly larger protrusion by the thumb MCP for the thumb rotator and a slightly larger proximal link for the index finger to better align the hands tripod grasp. Each finger consists of two links, one proximal and one distal, that begin at the metacarpophalangeal joint (MCP) and the proximal interphalangeal joint (PIP). The proximal link is the measured distance from the MCP to PIP and the distal link is the measured distance from the PIP to the distal fingertip with a slight bend (approx. 20°) at the distal interphalangeal joint (DIP). This slight bend is to improve alignment for the tripod grasp while also providing an additional point of contact during power grasp. At the base of the palm there is

a standard ½”-20 threaded post for socket integration with two rubber o-rings that help passively set the wrist position.

The palm and finger chassis are made of ABS plastic reinforced with 40% fiberglass by volume. This allowed for a slightly stronger and heavier chassis than our initial prototype. However, 3D printed plastic does not have the strength required for everyday use, especially in a commercial product. We have investigated other ways to manufacture stronger and lighter prosthetics using composites [23] that may be more suitable for daily use. Both the palm and finger pads have urethane gripping surfaces (Smooth-On, Vytaflex 40) to help promote more contact during precision and power grasping. The proximal index finger pad has an extended grip pad to promote additional contact for lateral grasp. These grip pads were optimized to promote contact for a variety of object sizes and geometry, which we will discuss in the next section.

The fingers consist of several components on top of the 3D printed chassis and urethane gripping surfaces. For all five fingers, MCP joint consists of three main components to allow the finger to passively open after a grasp and to eject under high loads to protect the finger. On a previous version of the hand [17], the MCP joint consisted of two half spring plungers and a torsional spring that created significant friction at the joint, ejected at too low of forces and misaligned the joint torsional spring. In this version of the hand, we improved this design by using an off the shelf watch quick release spring bar (Barton) that acts as the bearing surface for the joint and allows the finger to eject either by load or by sliding the quick release lever on the back of the finger. This spring bar acts as the joints center of rotation and is fixed within a guiding sleeve attached to the finger chassis. This guiding sleeve has a slot that fixes the torsional spring in place. The distal PIP joint consists of an elastic flexure that provides in-plane bending and passive out-of-plane reconfiguration for the distal link. This flexure has embedded cloth in the neutral axis to

mitigate axial stretch and provide additional out of plane stiffness while still promoting a smooth bending motion during finger actuation.

The finger tendons are tensioned to the differential whiffletree mechanism through a tensioning mechanism in the distal fingertip. This tensioning mechanism consists of a canulated screw and hex nut that can adjust the tendon knot position within the finger. This is necessary to pretension the finger to ensure uniform force transmission and closing rates. This tensioning mechanism is hidden under stainless steel fingernails that were designed to snap onto the distal end of the fingers. Just like in the human hand, our rigid fingernails work with the soft finger pad directly below to create a pocket that provides a soft compliant grasp of very thin or small objects. We found that extending the distal grip pad area up to the fingernail was necessary for grabbing very thin objects, as hard contact would lead to object ejection. Excess friction in the system is mitigated with guiding tubes and capstans to stop the tendon from wearing the 3D printed chassis.

VII. Final Device Testing

In this section, we will discuss how we evaluated our single actuator myoelectric hand and present our kinematic specifications and results. We had two primary ways of evaluating the device. First, bench top testing was completed to evaluate the general performance and specifications of the prosthetic hand. This was also to ensure the hands performance aligns with the specifications necessary for these devices outlined in previous literature. Second, a ten participant able-bodied study and a two participant amputee study was completed to evaluate the hands repetitive motion, learning curve and performance on activities of daily living. During testing, able-bodied participants wore an able-bodied simulator (*TRS Prosthetics*) that is designed to help able-bodied users simulate prosthetic use. This device includes a soft cast with a distal mounted prosthetic hand adapter. The amputee participants wore our device on a body-powered

socket that they provided. This was to ensure that the socket would fit snugly and be comfortable during testing. All the participants actuated the hand using a single external button that both opened and closed the hand to eliminate the potential issues that may come with learning a new control system for the hand. Last, the testing methods above were kept consistent to our evaluation of the preliminary version of this hand to more accurately compare the final and preliminary version.

7.1 Kinematic Specifications and Benchtop Testing

First, general kinematic specifications such as grasp aperture and force output in each grasp type were measured. Grasp aperture was measured using a digital micrometer from the distal opposing surfaces – fingertips for power/tripod and the thumb contact point for lateral grasp. These apertures were 132.5 mm in power grasp, 125 mm in tripod grasp and 52.5 mm in lateral grasp. These grasps were slightly larger than the previous version of the hand (113.8 mm in power/tripod and 15.4 mm in lateral) due to the widening of the initial angle of the thumb from the kinematic optimization study. The slight change in aperture in power and tripod are due to slight adjustments in the pre-tensioning in tripod grasp to keep its closing speed consistent. We believe these larger apertures, coupled with spring stiffnesses to speed the hands closing rate, provided a larger array of possible objects to grasp with minimal proprioceptive loss while grasping.

Next, the time to close the grasp was recorded to see if it aligns with recommended closing rates determined in previous literature. These were measured using the current sensor on the output of the motor which spikes when the hand begins to stall at finger contact. The average closing time was 1.02 seconds in power grasp, 0.53 seconds in tripod grasp and 0.60 seconds in lateral grasp. These timings were consistent with the previous version of the hand with larger apertures, with slightly slower speeds in the lateral grasp due to the aperture almost doubling.

Table 6. Final Prototype Benchtop Testing Results

Grasp Type	Grasp Specifications			Average Angular Closing Rates (°/s)			
	Grasp Force	*Closing Time*	*Aperture*	*FF MCP*	*FF PIP*	*T MCP*	*T PIP*
Power	14.30 N	1.02 s	132.5 mm	92.9	78.2	29.3	48.9
Tripod	5.02 N	0.53 s	125 mm	149.9	74.9	9.4	131.1
Lateral	17.20 N	0.60 s	52.5 mm	0 (fixed)	0 (fixed)	41.5	116.2

Figure 28. Example of force testing the prosthetic hand with two custom sensor embedded objects. This includes a 2.5 in diameter sphere for power grasp and a 1.5 in cube for tripod and lateral grasp.

In [27], the recommended closing rate for a tripod grasp should not exceed 0.8 seconds with a span greater than 90mm to have minimal effect on proprioception. In [28], adequate full closure of the hand in any grasp should be from 1 to 1.5 seconds. Our tripod grasp falls within dictated specifications in [28], however, it may be advantageous to increase the speed of the power grasp which falls outside this recommendation but within those in [27]. We believe that these speeds are adequate, with minimal proprioceptive interference, given the changes in kinematics and increase in grasp aperture.

Additionally, using a digital protractor the angle limits and hardstops were recorded and then divided by the closing rates to produce estimates for the average angular closing rates before contact. We must note that these are not linear but averages of the speed across the closing rate. Although none of these closing rates are near the performance of the human hand, near 300°/s, it

is rare to see human finger angular velocities exceed 100°/s during grasping [7]. For our force production ranges we believe that our grasp types nearing 100°/s are acceptable. These results are examined further in the table 2.

Next, grasp force was evaluated for each grasp type using custom sensor embedded objects that we believe were representative of how that grasp will be used on activities of daily living. For a fair comparison, we used the same actuator with the same gearing (*Faulhaber MCDC 3002S*) and the same sensor embedded object sizes (2.5 in sphere in power and 1.5 in cube in tripod/lateral), positioning and load cell (*Transducer Techniques MLP-25*) seen in figure 6. Additionally, the same grasp dynamometer was used (*Camry EH101 Digital Dynamometer*) to establish power grasp force in a more comparable manner. The average maximum grasp force using the sensor embedded object in power grasp was 14.3 N in power grasp, 5.02 N in tripod grasp and 17.2 N in lateral grasp. The grasp dynamometer produced 17.9 N of force in a 2in grasp span power grasp. First, we found that the force output was lower that the previous version in power and tripod grasp by 1-2 N. We found that this decrease in force occurred because the optimization was based on grasp stability and not directly correlated to grasp force. The best performing hand does not necessarily have the highest grasp force. For example, a hand with high relative grasp force with misalignment at the area of contact can produce more shear forces leading to ejection of the object. We can contribute our better performance in activities of daily living in the next section to the kinematic structure of the hand which although with less force production in these grasps provided more stability across a range of objects. The hand performed slightly better in tripod grasp 5.02 N compared to 3.56 N because the frictional losses have a greater contribution at low forces. The final version of the hand more effectively transferred force in this grasp type with slightly less frictional losses in the new transmission gearbox and backplate. We believe that if these were kept

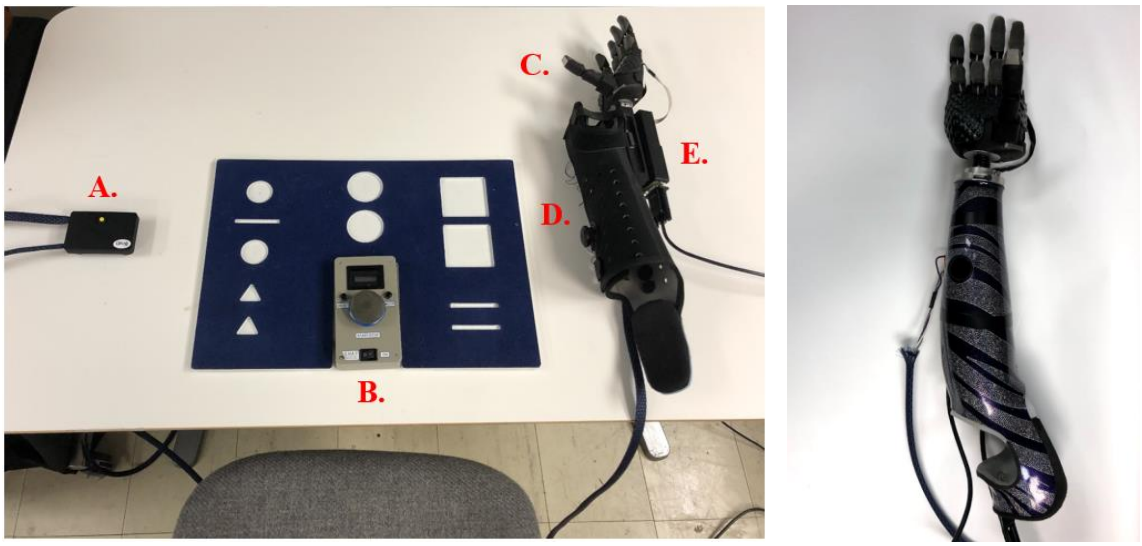

Figure 29. (Left) Example of the human subject testing setup including (A) the button to open and close the hand, (B) the given test that is being evaluated, (C) the hand, (D) the able-bodied adapter or socket for amputees, and (E) the control electronics. (Right) Example of the similar amputee participant system setup on a prosthetic socket.

similar there is a change this grasp type would have fairly similar or even less force production. Last the grasp dynamometer force production was fairly similar 17.9 N compared to 19.6 N previously. We believe that this loss is similar in explanation to the power grasp that hand slightly less force production after the kinematic stability optimization.

7.2 Human Participant Studies

In this section we will discuss our human participant study under IRB (ref#1608018242) where we tested ten able bodied participants (*n*=4 females, *n*=6 males, avg. age = 26.3) performing abstract object tasks and activities of daily living. Two tests were performed twice by each participant, once with their able dominant hand and once with the prosthetic device. This choice was to normalize their prosthetic scores with their able body scores to determine relatively how effective the prosthetic is at performing everyday activities. Next, a two participant amputee study was completed (*n*=2 females) where the participants completed the same two tests with their current myoelectric terminal device and with the MyoAdapt hand. Participant 1 (P1) tested with a

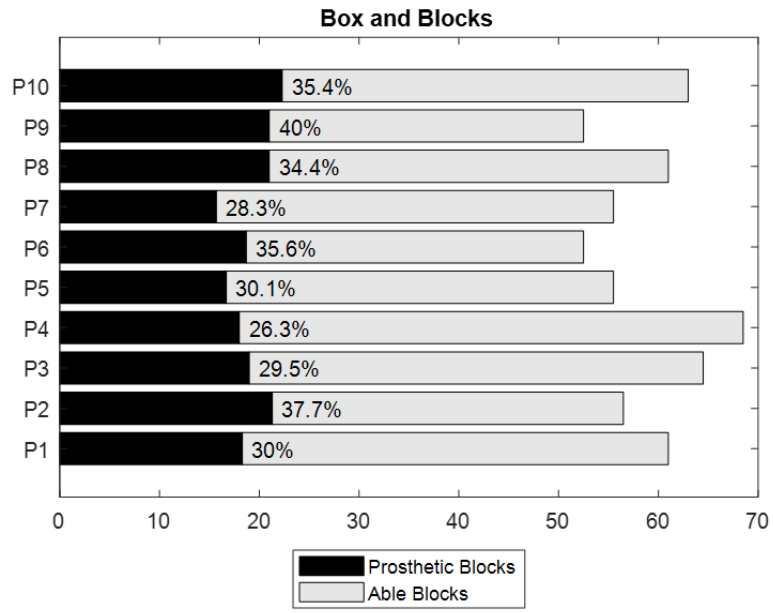

Figure 30. Box and Blocks test results comparing the prosthetic score for blocks moved over a barrier in sixty seconds to the users able hand. The values are expressed in terms of percentages of able-bodied scores.

small iLimb Quantum hand covered in a fabric glove with no active wrist rotation. Participant 2 (P2) completed her testing with a small Taska Hand with an active wrist and pattern recognition control. Each participant was a long time user (15+ years) of myoelectric devices and were familiar with the active control methods they used during testing.

The first test evaluated was the Box and Blocks test that evaluated repetitive motion. This test included three trials of moving 1 in cube blocks over a barrier for sixty seconds. The second test was the Southampton Hand Assessment Procedure (SHAP) [29] which evaluates the hands abilities to quickly complete activities of daily living. This consists of twelve abstract objects tasks and fourteen activities of daily living such as pouring, using a zipper, or turning a page. The goal of this test is to encourage the participant to complete a given task as fast as possible by pressing a timer, completing the task and then stopping a timer. The results of this test are graded on a scale of 100 where 100 is comparable to unimpaired hand function. The test setup and an example of a participant completing a SHAP task can be seen in figure 7.

In the box and blocks, the able-bodied participants scored an average of 19.2 blocks (σ=2.17, high=23, low=15) blocks over the barrier in sixty seconds when compared to an unimpaired μ=59.1 (σ=5.37, high=67, low=52). The average blocks missed while completing a task with a prosthesis was 3.1 blocks average over the course of the trial while with the normal hand a block was never missed during a trial. Outside of unsuccessful grasps, we found the prosthesis users took additional time planning where to grasp. We observed users selecting the nearest block or picking from the middle when using their able-bodied hand, whereas with the prosthesis users attempted to find blocks that were isolated. In the amputee participant study, P1 scored an average of 12 blocks over the barrier with the MyoAdapt hand and an average of 23 with their current iLimb hand. P2 scored slightly better with our hand, averaging 16 blocks over the barrier with our device and 23 blocks over the barrier with their Taska Hand. We found that it took both participants a little bit of time to familiarize with using the button for control. We believe that due to the limited training with the button control, these scores may be slightly elevated if the box and blocks was completed after more training or after the SHAP testing.

Other feedback from this testing includes that the lack of manipulability of the prosthesis including the ability to quickly reorient a block or regrasp a block in a cluttered environment may lead to more failures or added time to correctly place the hand. A second contributor to the added time was that the prosthesis is significantly slower while grasping and releasing the object. Participants that pre-grasped, effectively decreased the aperture of the grasp by prematurely closing before the grasp, had significantly better results. With the prosthesis' simple architecture, barring the ability to manipulate or change aperture, we believe that picking around 30% of the participants able-bodied hand is sufficient given minimal training. We found all participants were roughly in the same range of average blocks picked with the prosthesis with percentage variations

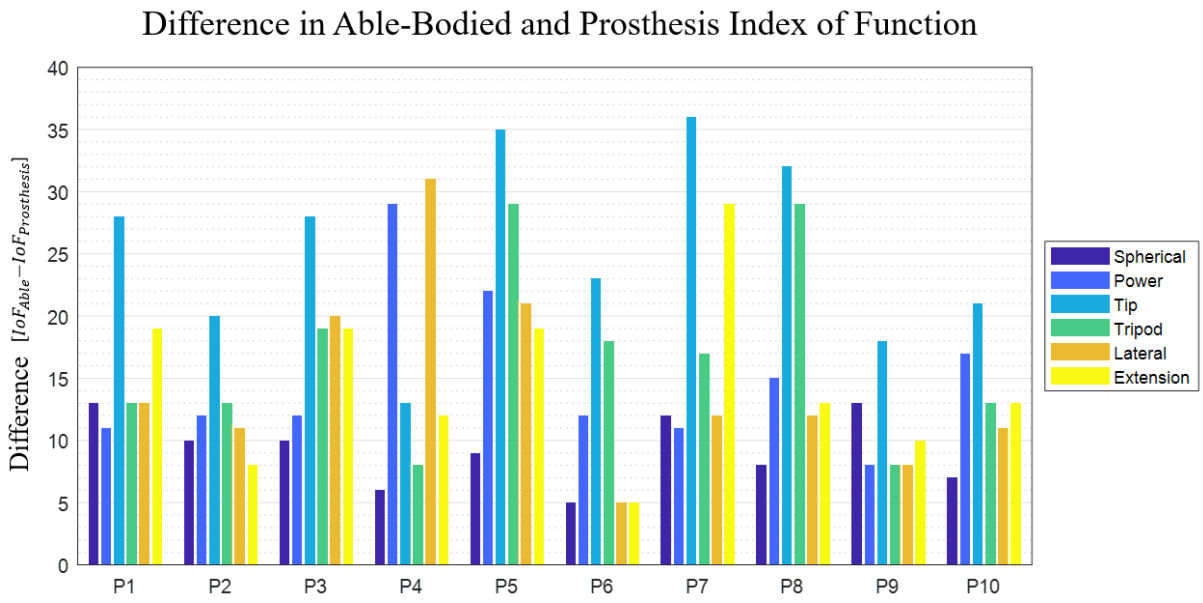

Figure 31. Difference in prosthetic and able-bodied scores for the SHAP by participant. Each participant is segmented by each of the six grasp types that the tests tasks are divided into. The differences between able bodied and prosthesis use describes the percentage of hand function that is lost by the device with larger numbers indicating a larger loss in function.

being influenced by how quick they were with their able bodied hand. The maximum we observed was 40% of able-bodied blocks picked with the prosthesis and the minimum we observed was 26.3% of able-bodied blocks picked with the prosthesis. In the future, we would like to see if the control tradeoff of adding manipulation or aperture adjusting abilities in the control can feasibly increase a prosthetic hands ability in this test. The full results are seen in figure 7.

In the SHAP test, the participants scored an average of 83.7 Index of Function or IoF (σ=4.00, high=90, low=78) with the prosthesis when compared to an average 97.5 IoF (σ=2.72, high=103, low=94) with the participant's able hand. Using the prosthesis, we found difficulties in the tip and tripod tasks with averaging around 75 IoF compared to the able hand averaging 95 IoF. In the amputee participant study, P1 scored a 55 total IoF with her iLimb device performing best in the lateral grasp tasks (74 Iof) and worst in Tip grasp tasks (33 IoF). P1 scored slighntly lower with the MyoAdapt hand scoring 44 total IoF and performing best in Spherical grasp (70 IoF) and

worst in Tip and Tripod grasp (26 IoF, 24 Iof). P2 scored a 62 total IoF performing best in the Spherical grasp tasks (84 IoF) and worst in the Tip grasp tasks (32 IoF). With the MyoAdapt hand P2 scored similarly with a 60 total IoF, performing best in Spherical grasp tasks (83 IoF) and worst in Tip grasp tasks (28 IoF). During the testing, we found that our hand performed better than the previous version, however, still lacked in tripod/tip grasp. We observed that grasps in tripod/tip were approached similarly with the prosthesis than with the able-hand or current prosthetic device, however, we found that participants lost significant time post-grasp attempting to replace the object. This was seen especially when an object was grasped further away from its center of mass causing post-contact rotation of the object in the hand. While underactuation, especially with differential mechanisms, aides force distribution and contact stability we believe kinematic improvements can still be made to further refine the hand. In the future, we believe integrating off-center center of masses relative to the antipodal points in our optimization framework can improve the kinematics and grasping stability of the hand. The prosthesis performed the best on the spherical tasks which averaged 90 IoF for able-bodied and 77 IoF for amputee participants. We believed that this result was excellent for our prosthesis and found that most of the time difference was accounted for the time to open or close the hand relative to the able-bodied hand. Some examples of successful grasps representative of activities of daily living can be seen in figure 34.

Last, no test is perfect and during human participant studies it is hard to evaluate a device without evaluating the user's ability. We found that in every bilateral task, results with the prosthesis were slowed from having to move from the task to the driving button and then back to the task. Additional time was observed on each task when attempting to move to and from the timer. The user's ability to located and correctly hit the button or timer greatly influenced their final score.

7.3 Comparison to the Initial Prototype

In the benchtop testing, we found the change in hand kinematic parameters displayed favorable results when compared to the previous device. This is including a widened aperture, and thus range of motion, in all three grasps by around 20mm with similar average angular closing rates. Because prosthesis have not approached the potential of the human hand, improvement in grasp range of motion and speed is a positive contribution when creating anthropomorphic hands given there is minimal force tradeoff. In underactuated systems with a single actuator and simple transmission, there exists an inverse relationship between grasp force and grasp speed. This tradeoff in the MyoAdapt hand included around 14% average increase in closing rates with around a loss of 1% of average grasp force across all grasp types. Given the increase in grasp aperture and average angular closing rates we found only slight changes in force production. This included an increase in precision grasp force from the optimization with only slight decreases in force production in power and tripod. We believe that the slight decrease in power and tripod is an artifact of improved design of the transmission mechanisms in the hand which more efficiently transferred torque from the motor to the fingers - including the integration of friction reducing mechanisms in the whiffletree mechanisms and gearbox. We found that having unique grasp types such as a slower and stronger power grasp and a faster more delicate tripod grasp helped us navigate this tradeoff for a variety of situations. This includes having the force production to grab a heavy sphere but also have the speed to quickly grasp and regrasp small blocks, coins or buttons.

In the human participant trials, we found improvements in reported scores for the Box and Blocks and SHAP test over the initial prototype. In the Box and Blocks the final prototype scored an average of 19.2 blocks with 2.17 blocks missed and the initial prototype scored 19.1 blocks with 3.7 blocks missed. Although this increase isn’t substantial, we found the increased aperture in tripod grasp made the hand slower at grasping blocks. However, we believe the added stability

bolstered the ratio of blocks that were successfully grasped. This is interesting because we found you can slightly increase scores on this test simply by reducing the amount of blocks dropped. If we were to repeat this test with larger blocks we would expect our hand to perform even better because the change in aperture may have less of an effect. In the SHAP test we found that our average index of function of 83.7 over the previous index of function was 82.0. Although this seems like only a slight improvement, this represents a 17 second gross improvement on the entire test which aggregates to around 150 seconds for an 82. Next, our kinematic optimization was created to focus on the low scores received on the previous devices testing – specifically in the tripod (μ=74.2 IoF) and tip (μ =50.2 IoF) categories. The final version improved significantly on these tasks including a 71.4 IoF in tip and 77.8 IoF in tripod. We found that users had significantly less time required to successfully learn the task before completing a timed trial. This includes additional stability on the heavy objects being grasping in tripod. We noticed that the extended grip pads significantly helped for the tripod grasping abstract object tasks and thin objects such as the page and coins. We also saw minimal change in the performance in power grasp activities even with the slightly decreased power grasp force. We believe this can also be attributed the additional friction and more effective force transfer from the changes in fingerpad geometry.

When comparing participants able-bodied IoF to prosthesis (Fig. 9) we found that participants performed nominally the best on spherical grasp tasks and the worst on tip grasp tasks. In spherical grasp we found participants were only 10 IoF or approximately 10% worse than using their able-bodied hand whereas in the tip they were approximately 27 IoF or 27% worse than their able-bodied hand. All the other grasp types evaluated in the SHAP had participants that either performed very well (<10% from able-bodied) or very bad (>25% from able bodied). We would describe these tasks as user dependent and we believe these could potentially be improved with

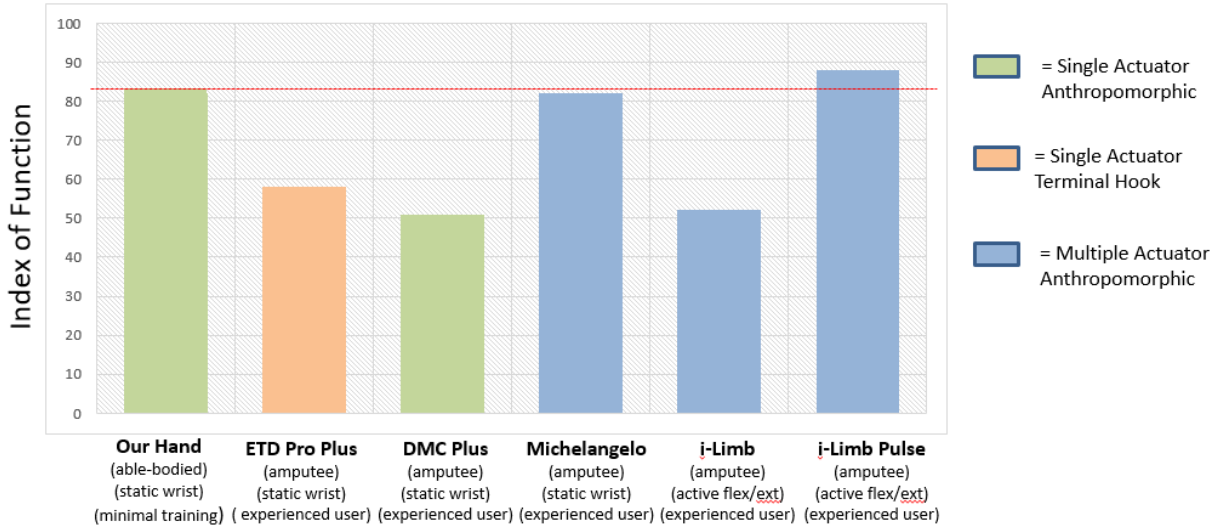

Figure 33. Variance in average SHAP scores for studies involving the MyoAdapt hand, another single actuator anthropomorphic hand (DMC Plus), a single actuator terminal hook (ETD Pro Plus), and three multiple actuator anthropomorphic hands (Michelangelo, i-Limb, i-Limb Plus).

increased training time. Additionally, we had two participants where almost all categories were within 10%-15% of their human hand function which we believe is incredible for a prosthetic device given minimal training. We found these participants, were more likely to approach grasping an object in a different way they would with their normal hand. We believe this creativity, which is necessary for grasping abstract objects with most simple prosthesis, is still beneficial for anthropomorphic devices. Last, we had two participants struggle, specifically when using the hands tripod grasp. This not only talks to the difficulty of grasping small objects like coins with anthropomorphic devices but also to the room for improvement there still is in precision grasping with underactuated devices.

7.4 Comparison to Commercial Prosthetic Hands

When compared to a single actuator robotic split hook in [30] (*Motion Control ETD Proplus)* our hand performed 37.1% better on the Box and Blocks and 44.3% better on the SHAP test for the able-bodied studies. When compared to a single actuator anthropomorphic robotic tripod

Figure 34. The MyoAdapt hand grasping objects in the three grasp types. (Left) Displaying passive adaptability in the power grasp, (Middle) displaying stability for small and large objects in tripod grasp, and (right) displaying activities of daily living in the lateral and passive hook grasps.

grasper [30] (*Ottobock Transcarpal DMC Plus)* our hand performed 37.1% better on the Box and Blocks and 64.1% better on the SHAP test. Although all the devices have a single actuation input, the relative increase in performance on the SHAP test, focused on activities of daily living, could have been bolstered by the ability to have more than one grasp type. This would provide less of a benefit on the SHAP test where a simple split hook and tripod grasper could suffice. In both evaluations the wrists were secured in their neutral positions. In [30] amputee subjects with significant training used myoelectric control while in our study a mechanical button was used for able bodied testing. We believe that novice users with a button would provide only a slide advantage, if any, over a trained prosthetic user.

When compared to a two actuator anthropomorphic robotic prosthetic hand [31] our hand performed 31.4% worse on the Box and Blocks and similar on the SHAP test after three months

of practice. When compared to a fully actuated five actuator anthropomorphic robotic hand [32] (*Ossur Touch Bionics i-limb)* we performed 61.0% better on the SHAP test after one month of practice and 10.1% better after one year of practice with the i-Limb device. Compared to the newer device (*Ossur Touch Bionics i-Limb Pulse*), our hand performed 5.9% worse after one month of practice and 3.8% worse after four months of practice with the device. With a static wrist our hand had similar results in the SHAP over the two actuator hand, however, lacked in the Box and Blocks. This could be due to our single actuator hands weak precision grasp compared to the Michelangelo's two motor precision grasp and the significant training time allowed for the participant. Minimal grasp variety in the Michelangelo hand could have been a negative component to the overall index of function. Compared to the five actuator hands our hand performed favorably against the i-Limb and slightly worse than the i-Limb Pulse. Although there is only one participant in [32], he had the ability to actively flex and extend his wrist which could provide a benefit in the SHAP test for complex motions. All amputee subjects in [31][32] had significant training with myoelectric control and should have provided minimal benefit over the button.

When comparing our amputee participant study to their current devices we found that performance was comparable, but slightly worse, then the current devices the participants were using. P1 scored 20% better with their current iLimb device on the SHAP test compared the MyoAdapt hand summing to an 11 point difference in index of function. In post study feedback, P1 noted that the device got easier after completing a decent amount of the tasks and may have required additional training time (maybe an hour versus the ten minutes allotted) to familiarize better with the button control and hand. She liked that some of the more difficult tasks to complete with her current device were easy with this device and minimal training. This included the

MyoAdapts lightweight, responsiveness and aperture compared to her current device. The task that P1 found most difficult was the zipper task which requires a significant amount of pinch force that the MyoAdapt and iLimb did not have. P2 scored 3% better with their current Taska hand with active wrist and pattern recognition, summing to a 2 point difference in index of function. In post study feedback, P2 noted that she liked the hands wide aperture and ability to grasp round objects in power and tripod grasps. She enjoyed the finger dexterity and the ability to fixate objects within the hand and between the fingers. She found that the hardest task to perform was the coins, which is harder to complete with complaint rather than rigid fingers, and would like the hand in the future to have an active wrist to make adjusting for objects easier. We found that P2 was able to quickly adjust to the new device and control method for the MyoAdapt hand. Overall, we believe that the MyoAdapt hand performing similarly to the amputee participants current devices was a favorable result. We believe that the minimal training and weight could be a significant advantage to long time users or people who are new to amputation. We believe that the MyoAdapt scores would potentially close the slight score differential if other factors, such as the time added from the button control in bimanual tasks, was factored into the overall score. The comparable result shows that significant underactuation in prosthetic hands, or using a single actuator instead of the five or six actuators in most commercial anthropomorphic hands, is appealing in the context of upper limb terminal device design when it comes to weight, power, responsiveness and performance.

VIII. Conclusion

My colleagues and I displayed that through novel underactuated mechanism design and leveraging multiple grasp types, you can create a single actuator anthropomorphic prosthetic hand that is similar in functionality to hands with complex control and multiple actuators. We also found that optimizing the kinematic and geometric parameters of a hand -given identical power, control

and transmission – can lead to better performance on repetitive tasks and activities of daily living. Last, we believe the MyoAdapt hand is a convincing argument for single actuator underactuated prosthesis. An underactuated anthropomorphic hand driven by a single actuator provides the benefits of simple control, passive adaptation and reduced weight that is favorable for many amputees [1]. There is currently no hand that can mimic the functionality of the human hand, however, as control and hand complexity improves, we believe the MyoAdapt hand - alongside other underactuated hands - can serve an important purpose. We believe that a hand with mechanical complexity and simple control can be a great launching pad with people who are new to amputation and can make a stepping stone to familiarizing themselves with upper limb prosthesis.

The goal of my research is to further improve the capabilities of single actuator prosthetic hands through broader impacts by producing scientifically relevant research and providing amputees with a device that they will feel comfortable adopting. This means completing and publishing research that was important to the general robotics, rehabilitation and mechanism design communities. Alongside this research I aligned the hand to the needs of amputees both functionally and financially – including receiving amputee feedback from clinically testing and investigating billing codes to make the device more accessible and affordable. This will included the opportunities to learn more about the needs of upper limb amputees by attending conferences, local clinics and camps. I believe I have achieved my goals of a successful PhD by completing my two main goals; enriching the rehabilitation robotics community with impactful novel research and providing amputees with a low-cost functional underactuated single actuator prosthetic hand.

References

[1] E. Biddiss and T. Chau. Upper Limb Prosthesis Use and Abandonment: A Survey of the Last 25 Years. *Prosthetics and Orthotics International*, 31(3), 2007, pp. 236-257.

[2] W. Knight. "Why Robots and Humans Struggled with DARPA's Challenge." MIT Technology Review, 9 June 2015. https://www.technologyreview.com/s/538156/why-robots-and-humans-struggled-with-darpas-challenge/

[3] D. Childress. Historical Aspects of Powered-Limb Prostheses. *Clinical Prosthetics and Orthotics*, vol 9, 1995.

[4] F. Cordella, A. Ciancio, R. Sacchetti,A. Davalli, A. Cutti, E. Guglielmelli and L. Zollo. Literature Review on Needs of Upper Limb Prosthesis Users. *Frontiers in Neuroscience*, 209(10), 2006.

[5] K. Ziegler-Graham, E. MacKenzie, P. Ephraim, T. Travison and R. Brookmeyer. Estimating the Prevalence of Limb Loss in the United States: 2005 to 2050. *Archives of Physical Medicine and Rehabilitation*, 89(3), 2008.

[6] T. Neri and J. Cregg. New Prosthetic Arms Provide Greater Quality of Life for Amputees, University of Pittsburg, Nov, 2009.

[7] G. McGimpsey and T. Bradford. Limb Prosthetics Services and Devices: Critical Unmet Need Market Analysis. Worcester Polytechnic Institution Bioengineering Institute, 2006.

[8] J.N. Ingram, K.P. Körding, I.S. Howard and D.M. Wolpert. "The statitstics of natural hand movements." *Experimental Brain Research*, Vol. 188, No. 2, pp. 223-236, 2008.

[9] F.J. Valero-Cuevas, F.E. Zajac and C.G. Burgar. "Large index-fingertip forces are produced by subject-independent patterns of muscle excitation." *Journal of Biomechanics*, Vol. 31, 1998.

[10] T. Laliberté and C.M. Gosselin. "Underactuation in robotic grasping hands." *Journal of Machine Intelligence and Control*, Vol. 4, No.3, pp.77-87, 2002.

[11] S. Hirose and Y. Umetani. "The development of soft gripper for the versatile robot hand." *Mechanism and Machine Theory*, Vol.13, pp.351-358, 1978.

[12] L. Birglen, T. Laliberté and C.M. Gosselin. *Underactuated Robotic Hands*. Springer-Verlag, ch. 2, 2008.

[13] M.C. Carrozza, C. Suppo, F. Sebastiani, B. Massa, F. Vecchi, R. Lazzarini, M.R. Cutkosky and P. Dario. "The SPRING Hand: Development of a Self-Adaptive Prosthesis for Restoring Natural Grasping," *Autonomous Robots*, Vol. 16, pp. 125-141, 2004.

[14] M. Controzzi, F. Clemente, D. Barone, A. Ghionzol and C. Cipriani. "The SSSA-MyHand: A Dexterous Lightweight Myoelectric Hand Prosthesis." *IEEE Trans. on Nueral Systems and Rehabilitation Engineering*, Vol.25, No. 5, pp. 459-468, 2017.

[15] L. Birglen and C.M. Gosselin. "Force Analysis of Connected Differential Mechanisms: Application to Grasping." *The International Journal of Robotics Research*, Vol. 25, No. 10, 2006.

[16] J.L. Pons, E. Rocon, R. Ceres, D. Reynaerts, B. Saro, S. Levin and W. Van Moorleghem. "The MANUS-HAND Dexterous Robotics Upper Limb Prosthesis: Mechanical and Manipulation Aspects." *Autonomous Robots*, Vol.16 pp. 143-163, 2004.

[17] B. Peerdeman, M. Valori, D. Brouwer, E. Hekman, S. Misra and S. Stramigioli. "Uti Hand I: A lock-based underactuated hand prosthesis." *Mechanism and Machine Theory*, Vol.78, 2014.

[18] Ottobock Michelangelo Product Brochure, 2018. https://www.ottobockus.com/media/local-media/prosthetics/upper-limb/michelangelo/files/michelangelo-brochure.pdf.

[19] M.G. Catalano, G. Grioli, E. Farnioli, A. Serio, C. Piazza and A. Bicchi. "Adaptive synergies for the design and control of the Pisa/IIT SoftHand." *The Int. Journal of Robotics Research*, Vol.33, No. 5, pp. 768-782, 2014.

[20] J.T. Belter and A.M. Dollar. "Novel Differential Mechanism Enabling Two DOF from a Single Actuator: Application to a Prosthetic Hand." *IEEE Int. Conf. on Rehabilitation Robotics*, Washington, USA 2013.

[21] C.M. Gosselin, F. Pelletier and T. Laliberté. "An Anthropomorphic Underactuated Robotic Hand with 15 Dofs and a Single Actuator." *IEEE Int. Conf. on Robotics and Automation*, California, USA, 2008.

[22] K. Xu, H. Liu, Z. Liu, Y. Du and X. Zhu."A Single-Actuator Prosthetic Hand Using a Continuum Differential Mechanism." *IEEE Int. Conf. on Robotics and Automation*, Washington, USA, 2015.

[23] M. Baril, T. Laliberté, C. Gosselin and F. Routhier. On the design of a mechanically programmable underactuated anthropomorphic gripper. *ASME Journal of Mechanical Design*, Vol.135, No.12, 2013.

[24] P. Wattanasiri, P. Tangpornprasert, and C. Virulsri. "Design of Multi-Grip Patterns Prosthetic Hand with Single Actuator." *IEEE Transactionson Neural Systems and Reahabilitation Engineering*, Vol. 26, No. 6, 2018.

[25] Ottobock Bebionic V3 Product Brochure, 2018. http://bebionic.com/distributor/documents/bebionic_information_for_users.pdf.

[26] Ossur Touch Bionics i-Limb Quantum Product Brochure, 2018. http://www.touchbionics.com/sites/default/files/files/MA01336USrev20January2017/-limbquantum.pdf.

[27] APRL Voluntary Closing Hook see http://fillauer.com/Upper-Extremity-Prosthetics/body-powered-systems/hooks/variable-force-hooks/index.html

[28] Hosmer Dorrance 5X Split Hook see http://hosmer.com/products/hooks/

[29] J. Sensinger, J. Lipsey, A. Thomas and K. Turner. Design and Evaluation of a Voluntary Opening and Voluntary Closing Prosthetic Terminal Device. *Journal of Rehabilitation Research and Development*, 52(1), 2015.

[30] TRS Grip 5 Prehensor see http://www.trsprosthetics.com/product/grip-5-evolution-prehensor/

[31] APRL Voluntary Closing Hand see http://fillauer.com/Upper-Extremity-Prosthetics/body-powered-systems/hands-and-gloves/male-hands/male-APRL-voluntary-closing-hand.html

[32] J. Zuniga, D. Katsavelis, J. Peck and C. Fernandez. Cyborg beast: a low-cost 3d-printed prosthetic hand for children with upper-limb differences. *BMC Research Notes*. 8(10), 2015.

[33] Ottobock Axon Hook see https://www.ottobockus.com/prosthetics/upper-limb-prosthetics/solution-overview/axon-hook/
[34] Motion Control ETD2 Hook see http://www.utaharm.com/etd-electric-terminal-device.php
[35] Ottobock Electric Griefer DMC see https://professionals.ottobockus.com/Prosthetics /System-Electric-Greifer-DMC-VariPlus/p/8E34~59
[36] PR2 Robot Hand see http://www.willowgarage.com/pages/pr2/specs
[37] Ottobock Speed Hand see https://www.ottobockus.com/prosthetics/upper-limb-prosthetics/solution-overview/myoelectric-devices-speedhands/
[38] RSL Steeper Bebionic V3 see http://bebionic.com/the_hand/features
[39] Touch Bionics I-Limb Quantum see http://www.touchbionics.com/products/active-prostheses/i-limb-quantum
[40] Taska Hand see http://www.taskaprosthetics.com/the-taska/features/
[41] L. Resnik, E. Acluche and M. Borgia. The DEKA Hand: A Multifunction Prosthetic Terminal Device-Patterns of Grip Usage at Home. *Prosthetics and Orthotics International*, 2017.
[42] A. Bicchi and V. Kumar. Robotic Grasping and Contact: A Review. *Proceedings of the IEEE International Conference on Robotics and Automation*, San Francisco. California, USA, 2000, pp. 348-353.
[43] A. Dollar and R. Howe. The Highly Adaptive SDM Hand: Design and Performance Evaluation. *The International Journal of Robotics Research*, 29(5), 2010.
[44] A. Mottard, T. Laliberte and C. Gosselin. Underactuated Tendon-Driven Robotic / Prosthetic Hands: Design Issues. *Proceedings of Robotics: Science and Systems Conference*, 2017.
[45] N. Dechev, W. Cleghorn and S. Naumann. Multiple Finger, Passive Adaptive Grasp Prosthetic Hand. *Mechanism and Machine Theory*, 36(10), 2001. pp.1157-1173.
[46] I. Bullock, J. Zheng, S. De La Rosa, C. Guertler and A. Dollar. Grasp Frequency and Usage in Daily Household and Machine Shop Tasks. *IEEE Transactions on Haptics*, 6(3), 2103. pp. 296-308.
[47] A.R. Tilley. *The Measure of Man and Woman: Human Factors in Design***.** John Wiley and Sons, New York, 2002.
[48] J.T. Belter, M.T. Leddy, K.D Gemmell and A.M Dollar. "Comparative Clinical Evaluation of the Yale Multigrasp Hand." *IEEE RAS Int. Conf. on Biomedical Robotics and Biomechatronics*, Singapore, 2016.
[49] J.T. Belter and A.M. Dollar. "Novel Differential Mechanism Enabling Two DOF from a Single Actuator: Application to a Prosthetic Hand." *IEEE Int. Conf. on Rehabilitation Robotics*, Washington, USA 2013.
[50] J.G. Burgerhoff, E. Vasluian, P.U. Dijkstra, R.M. Bongers and C.K. Van Der Sluis. "The Southampton Hand Assessment Procedure revisited: A transparent linear scoring system, applied to data of experienced prosthetic users." *Journal of Hand Therapy*, Vol.30 pp.49-57, 2017.
[51] M. Deijs, R.M. Bongers, N.D.M. Ringeling-Van Leusen and C.K. Van Der Sluis. "Flexible and static wrist units in upper limb prosthesis users: functionality scores, user satisfaction and compensatory movemetns." *Journal of NeuroEngineering and Rehabilitation*, Vol.12, No. 26, 2016.
[52] M. Luchetti, A.G. Cutti, G. Verni, R. Sacchetti and N. Rossi. "Impact of Michelangelo prosthetic hand: Findings from a crossover longitudinal study." *Journal of Rehabilitation Research and Development*, Vol. 78, pp.307-323, 2014.
[53] O. Van Der Niet, R. M. Bongers and C.K. Van Der Sluis. "Functionality of i-Limb and i-Limb Pulse hands: Case report." *Journal of Rehabilitation Research and Development*, Vol. 50, 2013.
[54] J.T. Belter and A.M. Dollar. "Performance Characteristics of Anthropomorphic Prosthetic Hands." *IEEE Int. Conf. on Rehabilitation Robotics*, Switzerland, 2011.
[55] R. Vinet and Y. Lozac'h. "Design methodology for a multifunctional hand prosthesis," *Journal of Rehabilitation Research and Development*, Vol. 32, No. 4, pp. 316-324, 1995.
[56] N. Dechev, W.L. Cleghorn and S. Neuman. "Multiple finger, passive adaptive grasp prosthetic hand." *Mechanism and Machine Theory*, Vol. 36, pp. 1157-1173, 2001.
[57] C.M. Gosselin, F. Pelletier and T. Laliberté. "An Anthropomorphic Underactuated Robotic Hand with 15 Dofs and a Single Actuator." *IEEE Int. Conf. on Robotics and Automation*, California, USA, 2008.
[58] M.G. Catalano, G. Grioli, E. Farnioli, A. Serio, C. Piazza and A. Bicchi. "Adaptive synergies for the design and control of the Pisa/IIT Softhand." *The Int. Journal of Robotics Research*, Vol.33, No.5, pp.768-782, 2014.
[59] M.C. Carrozza, C. Suppo, F. Sebastiani, B. Massa, F. Vecchi, R. Lazzarini, M.R. Cutkosky and P. Dario. "The SPRING Hand: Development of a Self-Adaptive Prosthesis for Restoring Natural Grasping," *Autonomous Robots*, Vol. 16, pp. 125-141, 2004.
[60] M.T. Leddy and A.M. Dollar. "Preliminary Design and Evaluation of a Single-Actuator Anthropomorphic Prosthetic Hand with Multiple Distinct Grasp Types", *IEEE Int. Conf, on Biomedical Robotics and Biomechatronics*, Enschede, Netherlands, 2018.
[61] H. Stuart, S. Wang, O. Khatib and M. Cutkosky. "The Ocean One hands: An adaptive design for robust marine manipulation," *The Int. Journal of Robotics Research*, Vol.36, No. 2, pp.150-166, 2017.
[62] A. Rodriguez, M.T. Mason and S. Ferry. "From Caging to Grasping." *Robotics: Science and Systems*, California, USA, 2011.
[63] L. Birglen, T. Laliberté and C.M. Gosselin. *Underactuated Robotic Hands*. Springer-Verlag, 2008.
[64] A. Bicchi and V. Kumar. "Robotic Grasping and Contact: A Review." *IEEE Int. Conf. on Robotics Research and Automation*, California, USA, 2000.
[65] L. Birglen and C. Gosselin. "On the Force Capability of Underactuated Fingers." *IEEE Int. Conf. on Robotics Research and Automation*, Taipei, Taiwan, 2003.

[66] S.A. Spanjer, R. Balasubramanian, J.L. Herder and A.M. Dollar. “Improved Grasp Robustness through Variable Transmission Ratios in Underactuated Fingers.” *IEEE Int. Conf. on Intelligent Robots and Systems*, Algarve, Portugal, 2012.
[67] M. Ciocarlie and P. Allen. “A constrained optimization framework for compliant underactuated grasping.” *Mech. Sci.*, Vol.2, pp. 16-26,2011.
[68] M. Haas-Heger, G. Iyengar and M. Ciocarlie. “Passive Reaction Analysis for Grasp Stability.” *Trans on. Automation Science and Engineerin*g, Vol.15, No.3, pp.955-966, 2018.
[69] D. Prattichizzo, M. Malvezzi, M. Gabiccini and A. Bicchi. “On Motion and Force Controllability of Precision Grasps with Hands Actuated by Soft Synergies.” *IEEE Trans. on Robotics*, Vol.29, No.6, pp.1440-1456, 2013.
[70] M.V. Liarokapis and A.M. Dollar. “Post-Contact, In-Hand Object Motion Compensation with Adaptive Hands.” *IEEE Trans. on Automation Science and Engineering*, Vol.15, No.2,pp.456-467, 2017.
[71] L.U. Odhner, R.R. Ma and A.M. Dollar. “Open-Loop Precision Grasping With Underactuated Hands Inspired by a Human Manipulation Strategy.” *IEEE Trans. on Automation and Engineering*, Vol. 10, No.3, pp.625-633, 2013.
[72] C. Ferrari and J. Canny. “Planning Optimal Grasps.” *IEEE Int. Conf. on Robotics and Automation*, Nice, France, 1992.
[73] MATLAB and Parallel Computing Toolbox Release 2018a, The MathWorks, Inc., Natick, Massachusetts, Unite States.
[74] A.M. Kociolek and P.J. Keir. “ Design methodology for a multifunctional hand prosthesis.” *Journal of Rehabilitation Research and Development*, Vol. 32, No. 4, pp.316-324, 1995.
[75] J.K. Salisbury. “The design and control of a dexterous mechanical hand.” *Proc. ASME Computer Conf.*, USA, 1981.
[76] R.R. Ma, N. Rojas and A.M. Dollar. “Spherical Hands: Towards Underactuated, In-Hand Manipulation Invariant to Object Size and Grasp Location.” *ASME Journal of Mechanisms and Robotics*, 2016.
[77] Robotiq Hand-E, 2-Finger and 3-Finger Adaptive Robot Grippers, 2019. https://robotiq.com/products/3-finger-adaptive-robot-gripper
[78] C. Piazza, G. Grioli, M.G. Catalano and A. Bicchi. “A Century of Robotic Hands.” *Annual Review of Control, Robotics and Autonomous Systems*, Vol. 2, No. 1, pp.1-32, 2019.
[79] M. Roa and R. Suarez. “Grasp quality measures: review and performance.” *Autonomous Robots*, Vol. 38, pp.65-88, 2015.
[80] H. Hertz. “On the contact of solid elastic bodies and on hardness.” *Journal of Math*, Vol. 92, pp.156-171, 1881.
[81] R. Mindlin. “Compliance of elastic bodies in contact.” *Journal of Applied Mechanics*, Vol. 16, pp.259-268, 1949.
[82] K.L. Johnson. *Contact Mechanics*. Cambridge University Press, 1985.
[83] H.X. Trinh, V.A. Ho and K. Shibuya. “Theoretical Foundation for Design of Friction-Tunable Soft Finger with Wrinkle’s Morphology.” *IEEE Robotics and Automation Letters*, 2019.
[84] R.R. Ma, N. Rojas and A.M. Dollar. “Towards Predicable Precision Manipulation of Unknown Objects with Underactuated Fingers.” *Advances in Reconfigurable Mechanisms and Robots II*, Vol.36, pp.927-937, 2016.
[85] M. Honarpardaz, M. Tarkain, D. Sirkett, J. Olvander, X. Feng, J. Elf and R. Sjogren. “Generic Automated Multi-Function Finger Design.” *International Conference on Mechanical Engineering and Automation Science*, 2016.
[86] M. Li, K. Hang, D. Kragic and A. Billard. “Dexterous Grasping Under Shape Uncertainty.” *Robotics and Autonomous Systems*, Vol. 75, pp. 352-364, 2016.
[87] J. Mahler, J. Liang, S. Niyaz, M. Laskey, R. Doan, X. liu, J. Ojea and K. Goldberg. “Dex-Net 2.0: Deep Learning to Plan Robust Grasps with Synthetics Point Clouds and Analytic Grasp Metrics.” *Robotics: Science and Systems*, 2017.
[88] B. Calli, A. Walsman, A. Singh, S. Srinivasa, P. Abbeel and A. Dollar. “Benchmarking in Manipulation Research: The YCB Object and Model Set and Benchmarking Protocols.” *IEEE Robotics and Automation Magazine*, Vol. 22, No. 3, pp. 36-52, 2015.
[89] H. Song, M. Wang and K. Hang. “Fingertip Surface Optimization for Robust Grasping on Contact Primitives.” *IEEE Robotics and Automation Letters*, Vol.3, No. 2, pp.742-749, 2018.
[90] F. Chen, W. Xu, H. Zhang, Y. Wang, J. Cao, M.Y. Wang, H. Ren, J. Zhu and Y.F. Zhang. “Topology Optimized Design, Fabrication, and Characterization of a Soft Cable-Driven Gripper.” *IEEE Robotics and Automation Letters*, Vol. 3, No. 3, pp. 2463-2470, 2018.
[91] ASTM Standard D1894, 2001, “Standard Test Method for Static and Kinetic Coeffiicents of Friction of Plastic Film and Sheeting,” ASTM International, West Conshohocken, PA, USA. www.astm.org.
[92] J. Van Kuilenburg, M.A. Masen and E. Van Der Heide. “A review of fingerpad contact mechanics and friction and ahow this affects tactile perception.” *J. Engineering Tribology*, Vol. 229, pp.243-258, 2015.
[93] H. Han, A. Shimada and S. Kawamura. “Analysis of Friction on Human Fingers and Design of Artificial Fingers.” *IEEE Int. Conf. on Robotics and Automation*, Minnesota, USA, 1996.
[94] N. Nachman and S.E. Franklin. “Artificial skin model simulating dry and moist *in vivo* human skin friction and deformation behavior.” *Tribology International*, Vol. 97, pp.431-439, 2016.
[95] C.P. Hendriks and S.E. Franklin. “Influence of surface roughness, material and climate conditions on the friction of human skin.” *Tribology Letters*, Vol. 37 pp. 361-373, 2010.
[96] M. Klaassen, E.G. De Vries and M.A. Masen. “Friction in the contact between skin and a soft counter material: effects of hardness and surface finish.” *Journal of the Mechanical Behavior of Biomedical Materials*, Vol. 92, pp. 137-143, 2019.
[97] V. Mathiowetz, N. Kashman, G. Volland, K. Weber, M. Dowe and S. Rogers. “Grip and Pinch Strength: Normative Data for Adults.” *Arch. Phys. Med. Rehabilitation*, Vol. 66, pp. 69-72, 1985.
[98] R.W. Gregory. “Biomechanics and Control of Torque Production During Prehension” PhD Diss., Pennsylvania State University, 2002.

[99] V. Falanga and B. Bucalo. “Use of durometer to assess skin hardness.” *Journal of the American Academy of Dermatology*, Vol. 29, No. 1, pp. 47-51, 1993.
[100] H. Bruhn, M. Gyngell, W. Hanicke, K. Merboldt and J. Frahm. “High-resolution fast low-angle shot magnetic resonance imaging of the normal hand.” *Skeletal Radiology*, Vol, 20, pp. 259-265, 1991.
[101] Zuniga, J., Katsavelis, D., Peck, J., Stollberg, J., Petrykowski, M., Carson, A. & Fernandez, C. 2015, "Cyborg beast: a low-cost 3d-printed prosthetic hand for children with upper-limb differences", *BMC research notes*, vol. 8, no. 1, pp. 10.
[102] *Enabling The Future: Upper Limb Prosthetics*. Available: http://enablingthefuture.org/upper-limb-prosthetics [2015, March25]
[103] *RSLSteeper Bebionic3: The Hand*. Available: http://www.bebionic.com/the_hand [2015, March 1].
[104] Ma, R.R., Belter, J.T. & Dollar, A.M. 2015, "Hybrid Deposition Manufacturing: Design Strategies for Multi-Material Mechanisms via 3D-Printing and Material Deposition", *Journal of Mechanisms and Robotics*, . vol. 7, no. 2, pp. 021002-10. doi:10.1115/1.4029400.
[105] Belter, J.T. & Dollar, A.M. 2014, "Strengthening of 3D printed robotic parts via fill compositing", *Intelligent Robots and Systems (IROS 2014), 2014 IEEE/RSJ International Conference on*IEEE, , pp. 2886.
[106] Jamalabad, V. R., Whalen, P. J., Pollinger, J., Agarwala, M. K., & Danforth, S. C. (1996, August). Gelcast molding with rapid prototyped fugitive molds. In Proceedings of Solid Freeform Fabrication Symposium, Austin, TX.
[107] Zonder, L., Sella, N., “Precision Prototyping, The role of 3D printed molds in the injection molding industry”, White Paper by Stratasys Inc, 2013, available at http://www.stratasys.com/~/media/Main/Files /White%20Papers/SSYS-WP-InjectionMolding-9-23-13.pdf
[108] *MARKFORGED:A new class of 3D printing materials*. Available: https://markforged.com/materials. [2015, February 02]
[109] *Touch bionics i-limb ultra: Key Features*. Available: http://www.touchbionics.com/products/active-prostheses/i-limb-ultra/key-features [2015, March 1].
[110] *Touch bionics i-limb ultra revolution.* Available: http://www.touchbionics.com/sites/default/files/i-limb_ultra_revolution_datasheet.pdf. [2015, February 05]
[111] *RedEye: Veroclear*. Material Data Sheet. Available: http://www.redeyeondemand.com/veroclear/. [2015, February 03]
[112] *Sicomin Technical Datasheet: PB 250, PB 400 / SD 560x Resilient % ambient curing epoxy foam*2014, . Available: http://www.sicomin.com/datasheets/product-pdf203.pdf [2015, March 3].
[113] ASTM D790, “Standard test method of flexural properties of unreinforced and reinforced Plastics and electrically insolating materials”, ASTM.org, ASTM International
[114] Aluminum 6061-T6; 6061-T651 *Material Properties, Matweb.com*, Available: http://www.matweb.com/search/DataSheet.aspx?MatGUID=1b8c06d0ca7c456694c7777d9e10be5b&ckck=1
[115] *Smooth-On PMC-780 Urethane Rubber*. Available: http://www.smooth-on.com/tb/files/PMC-780_Dry-Wet.pdf [2015, March 3].
[116] *Smooth-On Vitaflex Series Urethane Rubber*. Available: http://www.smooth-on.com/tb/files/Vytaflex_Series_TB.pdf [2015, March 3].
[117] Pylatiuk, C., Schulz, S., Doderlein, L., “Results of an Internet survey of myoelectric prosthetic hand users” *Prosthet Orthot Int.* 2007, Vol. 31, Issue 4, pp. 362–70.
[118] B.D. Jensen and L.L. Howell. “Identification of Compliant Pseudo-Rigid-Body Four-Link Mechanisms Resulting in Bistable Behavior.” *Journal of Mechanical Design*, Vol. 125, No. 4, pp. 701-708, 2003.